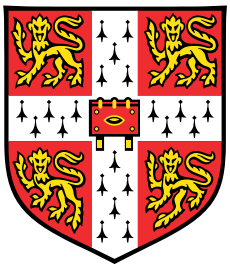

OUTFLOWS AND DUST IN QUASARS

MATTHEW JOHN TEMPLE

St. Catharine's College

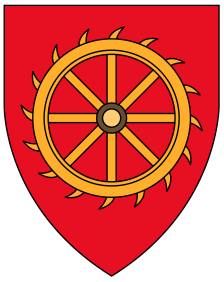

A thesis submitted to the

UNIVERSITY OF CAMBRIDGE

in partial fulfilment of the requirements for the degree of

DOCTOR OF PHILOSOPHY

under the supervision of

MANDA BANERJI & PAUL C. HEWETT

at the Institute of Astronomy

September 2020

DECLARATION

This thesis is the result of my own work and includes nothing which is the outcome of work done in collaboration except as declared in this preface and specified in the text. It is not substantially the same as any work that has already been submitted or is being concurrently submitted for a degree, diploma or other qualification at the University of Cambridge or any other University or similar institution. I further state that no substantial part of my dissertation has already been submitted or is being concurrently submitted for any such degree, diploma or other qualification at the University of Cambridge or any other University or similar institution.

The following work from this thesis has been published in *Monthly Notices of the Royal Astronomical Society*:

- Chapter 2 draws from
  "Fe III emission in quasars: evidence for a dense turbulent medium", **M. J. Temple**, G. J. Ferland, A. L. Rankine, P. C. Hewett et al., 2020, MNRAS 496, pp. 2565–2576.

- Chapters 3 and 4 draw from
  "Exploring the link between C IV outflow kinematics and sublimation-temperature dust in quasars", **M. J. Temple**, M. Banerji, P. C. Hewett, A. L. Rankine & G. T. Richards, 2021, MNRAS 501, pp. 3061-3073.

- Chapter 5 draws from
  "[O III] Emission line properties in a new sample of heavily reddened quasars at $z > 2$", **M. J. Temple**, M. Banerji, P. C. Hewett et al., 2019, MNRAS 487, pp. 2594–2613
  and
  "X-ray observations of luminous dusty quasars at $z > 2$", G. B. Lansbury, M. Banerji, A. C. Fabian & **M. J. Temple**, 2020, MNRAS 495, pp. 2652–2663.

Each chapter has benefited from collaboration with the authors named above. However, except where explicitly indicated in the text, the work contained in each chapter is my own.

This thesis does not exceed 60,000 words.

Matthew John Temple

Cambridge, September 2020

OUTFLOWS AND DUST IN QUASARS

Matthew John Temple

ABSTRACT

Supermassive black holes (SMBHs) at the centres of galaxies are known to actively accrete, forming so-called 'active galactic nuclei' (AGN) or 'quasars'. These AGN are believed to feed back energy into their host galaxies, regulating star formation and the growth of the SMBH itself. This thesis investigates the outflow properties in quasars at $1 < z < 3$, corresponding to the peak epoch of galaxy formation and SMBH growth.

First, I make use of recent improvements to atomic energy-level data and photoionisation models to constrain the properties of the Fe III emitting material in quasars. I show that this material must be dense and micro-turbulent to explain the observed strength of emission, and thus arise from the inner parts of the broad line region. The strength of this emission is shown to correlate with the outflow properties.

Second, I develop an SED model capable of reproducing the median observed photometric colours in the SDSS quasar population. This model is then used to investigate the properties of the emission from the hottest, sublimation-temperature dust components in the near infrared spectra of quasars. This dust is believed to be located at the inner edge of the toroidal obscuring structure. The strength of hot dust emission is found to correlate with the quasar outflow properties, providing evidence of a link between the broad line region and the dusty structures surrounding the inner regions of the AGN.

Finally, I quantify the outflow properties in a sample of heavily dust-reddened quasars. When matched in redshift and luminosity, there is no significant difference between the outflow kinematics of reddened and unobscured quasars. Assuming a paradigm in which dust-reddened quasars arise from major galaxy mergers, quasar-driven outflows must therefore persist after the obscuring dust is cleared from the line of sight.

for my family

FOREWORD

On a clear moonless night in June 2017, two final-year undergraduates pointed the Institute of Astronomy's 16″ telescope towards the radio source 3C273, using the position inferred from lunar occultation by Hazard, Mackey and Shimmins (1963).

A blue, point-like optical source was observed.

To the best knowledge of the author, it is still there.

CONTENTS

LIST OF FIGURES

LIST OF TABLES

ABBREVIATIONS

AGN	Active Galactic Nucleus/Nuclei
BAL	Broad Absorption Line
BLR	Broad Line Region
CDF	Cumulative Distribution Function
DR	Data Release
EW	Equivalent Width
FIR	Far-Infrared
FWHM	Full Width at Half Maximum
LSST	Vera C. Rubin Observatory Legacy Survey of Space and Time
MCMC	Markov Chain Monte Carlo
NLR	Narrow Line Region
S/N	Signal-to-Noise ratio
SDSS	Sloan Digital Sky Survey
SED	Spectral Energy Distribution
SMBH	Supermassive Black Hole
UKIDSS	UKIRT Infrared Deep Sky Survey
VHS	VISTA Hemisphere Survey
VIKING	VISTA Kilo-degree Infrared Galaxy Survey
WISE	Wide-Field Infrared Survey Explorer

1 INTRODUCTION

1.1 HISTORICAL BACKGROUND

1.1.1 *Black holes*

'Black hole' is a comparatively modern term; Lynden-Bell (1969) instead referred to the 'Schwarzschild throat'

Just over one hundred years ago, the field equations of General Relativity were proposed by Einstein (1915). Shortly afterwards, Schwarzschild (1916) found the first non-trivial solution of those equations: a spherically-symmetric solution representing a point mass with zero angular momentum embedded in an otherwise flat space-time. This point-like singularity is surrounded by a surface (Finkelstein, 1958) which is now known as the 'event horizon', first described by Michell (1784) in a Newtonian gravity, within which particles travelling at or below the speed of light cannot escape from the gravitational potential in finite time.

More recent work by Kerr (1963) showed that Einstein's field equations also admit point-mass solutions with non-zero angular momenta. These 'spinning' black holes still have an event horizon, albeit one whose size depends on the spin of the black hole.

In practice, all astrophysical black holes are expected to have some spin, as matter will not fall onto the event horizon in perfect spherical symmetry. By contrast, as they will always be surrounded by some form of neutral ionised plasma, the charge on any astrophysical black hole is expected to be negligible, and is assumed to be zero for the purposes of this thesis.

1.1.2 *Quasars and Active Galactic Nuclei*

Schmidt (1963) identified that the radio source 3C273 was a quasi-stellar (i.e. point-like) optical source with an emission spectrum consistent with broad Balmer lines shifted to the red by a factor

$$(1+z) = \frac{\lambda_{\text{observed}}}{\lambda_{\text{rest}}} = (1+0.158). \tag{1.1}$$

This finding led to Greenstein (1963) to realise that the spectrum of a similar radio source, 3C48, was consistent with a redshift $z = 0.368$. These redshifts implied that what we know now as *quasars* are located at cosmological distances, which in turn implied that the sources were highly luminous ($L \simeq 10^{46}\,\text{erg}\,\text{s}^{-1}$), making them the most powerful non-transient phenomena in the known universe. However, the rapid variability of these sources implied that the physical size of the emitting region was small, no more than a few light-days across.

The only process which can account for such extreme energies was quickly realised to be accretion onto supermassive (i. e., $M > 10^6 M_\odot$) black holes (SMBHs), and that turbulent viscosity was required to transport angular momentum outwards as mass is transported inwards (Salpeter, 1964; Zel'dovich, 1964). Such a process can liberate ~10 per cent of the rest mass-energy of the accreted material, in contrast to the 0.7 per cent released by stellar nucleosynthesis.

Sandage (1965) soon afterwards identified that there exist a significant population of radio-quiet quasars, which outnumber their radio-loud prototypes by at least an order of magnitude, and it later became clear that the bright galaxy centres identified by Seyfert (1943) were also due accretion onto SMBHs. The ubiquity of SMBH accretion was proposed by Lynden-Bell (1969), and such objects are now known collectively as 'Active Galactic Nuclei' (AGN; see Padovani et al., 2017, for a review).

We use 'AGN' as an abbreviation for both 'Active Galactic Nucleus' and 'Active Galactic Nuclei'

1.1.3 *Dust in the Universe*

Astrophysical dust can be taken to be any of the small solid particles, down to a few molecules, which are found in the interstellar medium of galaxies. Dust plays an important role in star formation through regulating the thermodynamics and chemistry of interstellar gas, although this is not discussed in this thesis.

As first noted by Trumpler (1930), dusty material attenuates light passing through it. More importantly, dust preferentially attenuates shorter wavelengths, such that bluer light is more heavily extincted. This effect is known as dust *reddening*, and can be seen to modify the colours of both the stars in the Milky Way and also the colours of galaxies in the distant universe. The degree of preferential attenuation is described by a dust extinction curve, which varies depending on the size, shape and composition of the dust grains, and is thus observed to differ between the Milky Way and the Small and Large Magellanic Clouds (Draine, 2003).

The energy that is absorbed by dust is re-radiated as thermal emission at infrared wavelengths. It has been estimated that 30 per cent of electromagnetic radiation from stars in the Universe is re-radiated in the infrared (Bernstein, Freedman and Madore, 2002), and thus emission from dust can contribute a significant fraction of the light observed from any extragalactic source.

1.1.4 *Unification*

Over the 1970s and 1980s, a diverse range of AGN began to be identified, and understanding the physics which gives rise to such diversity remains one of the keys goals of extragalactic astrophysics today.

The various emission lines seen in optical and ultraviolet AGN spectra often have different profiles, suggesting that the emitting material has a different line-of-sight projected velocity structure, and hence that the different emission lines arise from different physical regions (Peterson, 2006). One particular feature is the presence of broad ($\sigma > 1000\,\mathrm{km\,s^{-1}}$) emission lines from species such as C IV, Mg II, and the Balmer series, which are present in many AGN. Such broad emission lines are thought to be produced from a 'broad line region' (BLR), which, due to the large speeds required to produce broad lines via Doppler shifting, must be located close in to the central SMBH, such that the velocity dispersion of the emitting ionised gas can be accounted for by virial motions within the gravitational potential. This has been confirmed by reverberation mapping experiments, which find that the BLR is located within light-days to light-months of the central ionising source. More recent experiments (Li et al., 2017) have shown that different broad lines have different reverberation lags, suggesting that the BLR has a stratified structure with the higher ionisation lines emitted from closer in to the source of the ionising continuum.

In their landmark spectropolarimetry work, Antonucci and Miller (1985) showed that the so-called 'type 2' AGN, which do not show broad emission lines in their spectra, do in fact emit broad lines in polarised light. This lead to a unification scheme (Antonucci, 1993), which suggested that the region emitting the broad lines is still present in these objects, but merely obscured at some viewing angles by a toroidal dusty structure. In this scheme, many quasar properties can be explained by orientation, with the axisymmetric and geometrically thin (at least to first order; Shakura and Sunyaev, 1973) accretion disc and BLR surrounded by a circumnuclear region of gas and dust which blocks the line of sight to the innermost regions.

Antonucci (1993) admits this model is "only a caricature of the unification idea"

While the Antonucci model explains the type 1/2 dichotomy, there remain many observations of AGN which are not well understood. This thesis investigates the properties of type 1 quasars, i. e. luminous AGN which show broad emission lines in their rest frame optical and ultraviolet spectra. Within the unification scheme, these objects should also be representative of type 2 AGN, but we note that the ratio of type 1 : type 2 objects (in other words, the covering fraction of the obscuring region) could vary with the luminosity or accretion rate of the quasar (Netzer, 2015). Indeed, the structure of the toroidal obscuring region is not fully understood, and in Chapter 4 we investigate how the properties of the innermost dusty regions surrounding the SMBH are linked to the properties of the BLR.

1.1.5 *Estimating SMBH masses*

The main property of interest of any astrophysical black hole is its mass, given that it interacts with its surroundings primarily through the force of gravity. However, measuring any property of an object whose fundamental characteristic is a lack of intrinsic electromagnetic emission is inherently difficult. In the case of supermassive black holes, the mass is usually inferred by examining the kinematics of a well-defined material surrounding them, with a few notable exceptions such as the very long baseline interferometric observations of the accretion disc in M87 (Event Horizon Telescope Collaboration et al., 2019). For example, the mass of the SMBH at the centre of the Milky Way was derived using the motions of individual stars (Gillessen et al., 2009), and SMBH masses in some local Seyferts have been inferred from measurements of water maser discs (Miyoshi et al., 1995).

However, such techniques rely on the emitting material being spatially resolved, which is not possible in quasars outside the local universe. To overcome this problem, a large amount of time has been invested over the past few decades in reverberation mapping studies (e.g. Peterson, 1993). The broad emission lines in AGN are generally believed to be photoionised by the continuum emitted by the accretion disc, and so by monitoring both the continuum and line emission in a given object and observing how long it takes the lines to respond to variations in the continuum strength, it is possible to measure the light-travel time between the central source and the line emitting region. Under the assumption that the broad line-emitting gas is undergoing viral motions, the mass of the black hole is then given by

$$M = \frac{f v^2 R}{G} \tag{1.2}$$

where v is the velocity of material located at radius R, and f is a 'virial coefficient' of order unity determined empirically to transform the chosen measurement of the line width into a virial velocity.

The number of objects with reverberation-mapped masses is small, albeit rapidly growing (e.g. Shen et al., 2015). In order to estimate masses for larger numbers of black holes, a technique is required which only makes use of a single epoch of spectroscopy. Reverberation mapping has revealed that the radius of the BLR is tightly correlated with the continuum luminosity of the AGN. Theoretical considerations can show that this relation is expected to take the form $R_{BLR} \propto L^{0.5}$, and so throughout this thesis we make use of so-called 'virial mass estimators' of the form

Any single-epoch determination of a black hole mass will generally be referred to as an 'estimate' in this thesis

$$M_{BH} = M_0 \left(\frac{L}{L_0}\right)^{0.5} \left(\frac{\sigma}{\sigma_0}\right)^2 \tag{1.3}$$

where σ is some measurement of the width of an emission line, L is monochromatic luminosity at a nearby wavelength and M_0, L_0 and

σ_0 are constants calibrated for the given choice of σ and L. Systematic uncertainties in such estimates are at least 0.4 dex due to our inherently poor understanding of f.

1.1.6 *The Eddington limit*

For a point source of mass M emitting an isotropic luminosity L, Eddington (1925) showed that there is a value of L where the outwards force due to radiation pressure is equal in magnitude to the inwards force due to gravity:

$$\begin{aligned} \frac{L\kappa}{4\pi r^2 c} &= \frac{GM}{r^2} \\ \implies L_{Edd} &= \frac{4\pi GMc}{\kappa} \end{aligned} \tag{1.4}$$

where c is the velocity defined by Clerk Maxwell (1865) and κ is the opacity of the material located at radius r, i. e. the fraction of radiation energy flux absorbed per unit density per unit length. For pure ionised hydrogen, which is a good approximation for many astrophysical plasmas, $\kappa = \sigma_T/m_p$ where σ_T is the cross-section due to Thomson electron scattering and m_p is the rest mass of a proton. This gives

Note that other sources of opacity, such as dust grains, lead to a modified Eddington limit - we discuss this in Chapter 5

$$\begin{aligned} L_{Edd} &= \frac{4\pi GMm_p c}{\sigma_T} \\ &= 3.28 \times 10^4 \left(\frac{M}{M_\odot}\right) L_\odot \\ &= 1.26 \times 10^{38} \left(\frac{M}{M_\odot}\right) \text{ erg s}^{-1} \end{aligned} \tag{1.5}$$

For AGN, the Eddington luminosity gives a theoretical limit to the bolometric output of the central engine: assuming spherically symmetric accretion, if the AGN luminosity exceeds L_{Edd} then infalling material is blown away from the system and further accretion is prevented, thus removing the fuel source for the active nucleus. We therefore define the 'Eddington ratio' to be L/L_{Edd}, the fraction of the Eddington limit which equates to an object's bolometric luminosity.

The terms 'Eddington fraction' and 'Eddington ratio' are used interchangeably in this thesis

1.2 GALAXY EVOLUTION AND AGN FEEDBACK

1.2.1 *SMBH - host galaxy correlations*

It is now known that most, if not all, galaxies have a SMBH at their centre. The mass of the black hole has been found to correlate tightly with several properties of the host galaxy, most notably the stellar mass of the galactic bulge (Magorrian et al., 1998) and the velocity dispersion of stars well outside the radius within which the gravity of

the SMBH is dominant (Ferrarese and Merritt, 2000; Gebhardt et al., 2000; Kormendy and Ho, 2013; McConnell and Ma, 2013).

Many authors have attempted to explain these results by means of a co-evolution picture, whereby different modes of AGN 'feedback' inject energy into the interstellar medium of the host galaxy. This feedback regulates both star formation in the surrounding galaxy, and also the fuelling of the AGN, leading to a picture in which galaxy and SMBH evolve in parallel and regulate the growth of each other (Alexander and Hickox, 2012; Fabian, 2012; Harrison, 2017; King and Pounds, 2015; Silk and Rees, 1998). Feedback from AGN is now used in the study of galaxy evolution to also explain other observables such as the shape of the galaxy luminosity function (or more fundamentally, the mass function) and the morphologies of present-day galaxies (Sijacki et al., 2015; Vogelsberger et al., 2013).

1.2.2 *Galaxy mergers*

The most massive galaxies in today's universe must have undergone at least one major merger, and possibly more, in order to build up their present day masses; thus major mergers are an important component in many models of galaxy evolution. Merger-driven models normally predict a reddened quasar phase: as the galaxy merger triggers a burst of intense star formation, which in turn produces large amounts of reddening dust, at the same time gas is dynamically shocked and falls onto the central SMBH, triggering highly luminous AGN activity (Di Matteo, Springel and Hernquist, 2005; Hopkins et al., 2008; Narayanan et al., 2010; Sanders et al., 1988).

This proposed model for quasar activity and galaxy evolution is reliant on a 'blow-out' phase, where powerful small scale outflows from the inner regions of the active nucleus couple to gas and dust, transferring energy and momentum and driving large scale outflows which then disrupt the gas in the host galaxy, shutting down star formation and clearing obscuring material away from the line of sight to reveal a luminous blue quasar. Such outflows are likely to be driven by some combination of gas pressure and radiation pressure acting on dust, neutral hydrogen and atomic line transitions, and disc-driven magnetocentrifugal winds (e.g. Ishibashi, Banerji and Fabian, 2017; Ishibashi and Fabian, 2015; Konigl and Kartje, 1994; Murray et al., 1995; Proga, Stone and Kallman, 2000), although the dominant driving mechanism is still a topic of debate.

If this model is correct, one might therefore expect to see evidence for more powerful outflows in luminous dust-reddened quasars. However, this picture has not been fully tested, and in Chapter 5 we present the first comparative study of the outflow properties of reddened and unobscured quasars at $z \simeq 2$.

1.2.3 *AGN driven outflows*

Evidence for AGN feedback has now been seen in observations of different gas phases and at different wavelengths (e.g. Fabian, 2012; Harrison, 2017). However, it is still not clear how outflows from AGN are launched and driven into their host galaxies in such a way as to impact star formation. Moreover, it is not known what, if any, changes to the structure of the inner regions of the quasar (such as the BLR) could be expected by the presence of such outflows, or conversely what conditions in the BLR are required in order to drive outflows from the central engine to large distances. In Chapter 2 we investigate how emission from the dense, inner regions of the BLR is correlated with outflow signatures in the ultraviolet C IV emission line.

1.3 SIGNATURES OF OUTFLOWS IN QUASAR SPECTRA

Spectroscopic observations of AGN provide a powerful tool to identify and quantify outflows. Gas in the molecular phase is believed to contribute the largest fraction of the outflowing gas mass in an active galaxy. Such outflows can be identified through the broadening of lines due to molecular transitions, for example at sub-millimetre wavelengths (Cicone et al., 2014; Feruglio et al., 2010; Fiore et al., 2017). However, this thesis focuses on tracers of ionised gas, which can display more complicated (and arguably more interesting) kinematics.

If an outflow is being driven along the line of sight towards the observer, one would expect to see line emission from ionised gas which which has been shifted to the blue through the Doppler effect. The accretion disc and surrounding material in an AGN is generally taken to be optically thick, and lying roughly in the plane of the sky of the observer (for a type 1 object), leading to redshifted emission from any far-side outflow being obscured. Ionised gas outflows can thus be identified via tracers of different densities and ionisation states, manifesting through asymmetric line profiles with an excess of flux in the blue wing of the line.

If the conditions are right, outflowing gas along the line of sight can also produce absorption features. Some of the most dramatic evidence for quasar outflows comes from so-called Broad Absorption Lines (BALs) which can trace material travelling at speeds of tens of thousands of $\mathrm{km\,s^{-1}}$ in the rest frame of the quasar.

1.3.1 *C IV λ1549*

C IV λ1549 is a high ionisation line (64 eV), where the line profile is often asymmetric with an excess of emission in the blue wing. C IV is a typical broad emission line, and so C IV blueshifts are often taken to trace outflowing material on small scales, possibly in some wind

driven off the accretion disc. These blue excesses can skew the location of the median line flux by up to $\approx 5000\,\mathrm{km\,s^{-1}}$ relative to the systemic redshift (Richards et al., 2011).

However, the C IV emission line is often contaminated by both broad and narrow absorption features. Throughout this thesis we therefore make use of emission line properties derived using the spectral reconstructions presented by Rankine et al. (2020). Briefly, these reconstructions use the known correlation between the morphology of the C III] λ1909 emission complex and the blueshift of C IV to place priors on the weights of linear spectral components derived from a mean field independent component analysis of quasars which do not have any absorption features. These components are fit to the unabsorbed pixels in each quasar spectrum, where absorbed pixels are identified and masked in an iterative fashion until the fit converges and no unmasked pixel is more than 2σ below the reconstruction. The reconstructions essentially provide a higher signal-to-noise (S/N) version of each spectrum, with both broad and narrow absorption features masked to allow a more robust measurement of the emission line properties.

We use the C IV line properties measured by Rankine et al. (2020), who follow the prescription described by Coatman et al. (2016, 2017). A power-law in flux is defined using the wavelength windows 1445-1465 Å and 1700-1705 Å, and subtracted from the spectrum over 1500-1600 Å. The line blueshift is then defined as the Doppler shift of the line centroid relative to the rest frame wavelength of the emission line at the systemic redshift:

$$\text{C IV blueshift} \equiv c \times (\lambda_{\text{rest}} - \lambda_{\text{median}})/\lambda_{\text{rest}} \tag{1.6}$$

where $\lambda_{\text{rest}} = 1549.48$ Å is the rest frame wavelength of the C IV doublet, assuming equal contributions in emission from both components, and λ_{median} is the wavelength bisecting the total continuum-subtracted line flux.

1.3.2 *[O III] λ5008*

The forbidden [O III] λλ4960,5008 doublet transition traces ionised gas in regions of low ($n_e \sim 10^3\,\mathrm{cm^{-3}}$) electron density (Baskin and Laor, 2005). Such low density gas cannot be located in the BLR and must instead be significantly further out from the central regions of the AGN when compared to the C IV emitting material. The ratio of the λ4960 : λ5008 lines is set to be 1 : 2.98 by the Einstein coefficients (Storey and Zeippen, 2000), and is therefore assumed to be the same in all physical conditions and across all cosmic time.

[O III] is present as a strong emission line in many active galaxies, and the shape of the line can be used as a robust estimator of the kinematics of the emitting ionised gas. Spatially resolved observations

of [O III] in local ($z < 0.5$) active galaxies have found ionised gas moving with near-escape velocities on scales of $0.5 - 15$ kpc in most objects (e.g. Greene, Zakamska and Smith, 2012; Greene et al., 2011; Harrison et al., 2014; Liu et al., 2013; Tadhunter et al., 2018), although different observers use different definitions of spatial extent depending on whether they use spatially resolved kinematic data, narrow-band imaging or other methods (Baron and Netzer, 2019; Karouzos, Woo and Bae, 2016).

While the classic narrow [O III] emission line profile can be used to define the systemic redshift, more luminous AGN often have a broader ($v \sim 1000\,\mathrm{km\,s^{-1}}$) blueshifted component to the [O III] line, which is too broad to be tracing gas in dynamical equilibrium with the host galaxy. Recent work by Coatman et al. (2019) has found that the blueshift of the [O III] line is correlated with the blueshift of the C IV emission line, even when the dependence of both quantities on the quasar luminosity has been taken into account. If present, broad blue [O III] emission is usually interpreted as evidence for ionised gas outflows on kilo-parsec scales. If these outflows are indeed occurring on such large scales, then they would be capable of transferring significant amounts of kinetic energy from the active nucleus back into the host galaxy (Coatman et al., 2019; Harrison et al., 2018; Liu et al., 2013). The correlation with C IV would then provide evidence for quasar-driven outflows launched at small scales being driven to radii where they can have a significant impact on the host galaxy.

1.4 QUASARS IN LARGE-AREA SKY SURVEYS

1.4.1 *The Palomar-Green survey*

The bright quasar survey (BQS) of the Palomar-Green survey (Schmidt and Green, 1983) was the first large area survey to take spectra of, and hence identify, statistical numbers of quasars. Of the 114 quasars in BQS, 87 have redshifts $z < 0.5$. These were analysed in the seminal study of Boroson and Green (1992), who used a Principal Component Analysis (PCA) to gain understanding into the diversity seen in AGN spectra.

This PCA was the first attempt to identify the main drivers behind the variance in the rest frame optical spectral features, specifically Hβ, [O III], He II λ4686 and the many Fe II lines. Their first eigenvector (EV1), responsible for the largest amount of variance, is a strong anti-correlation between the strengths of [O III] and Fe II, and an anti-correlation between the strength of Fe II and the full width at half maximum (FWHM) of Hβ.

EV1 has since been extended with additional correlates to define a 'main sequence' for quasars (Marziani and Sulentic, 2014; Marziani et al., 2018; Sulentic, Marziani and Dultzin-Hacyan, 2000). Variation

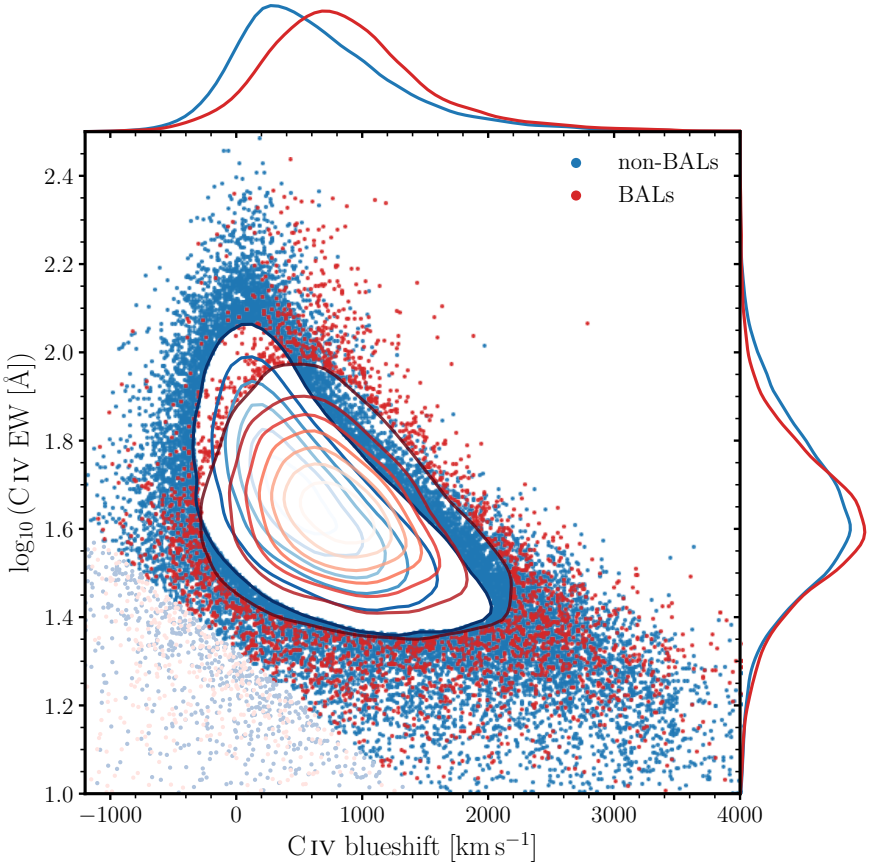

Figure 1.1: The space of C IV emission line blueshift versus C IV emission line equivalent width (EW), when reconstructing the line profile to account for absorption features. The anti-correlation between blueshift and EW is evident, especially in those objects without broad absorption lines (BALs).
Credit: Rankine et al. (2020), Fig. 8.

along this sequence is believed to be driven primarily by the Eddington fraction (Shen and Ho, 2014), which leads to modified accretion disc structures and outflow properties at fixed black hole mass (e. g. Giustini and Proga, 2019).

1.4.2 *The Sloan Digital Sky Survey*

The ability to cover large contiguous fields-of-view with charge-coupled devices triggered a revolution in survey astronomy. The Sloan Digital Sky Survey (SDSS; York et al., 2000) is now the largest source of quasar spectra at the time of writing. Almost 80,000 of those were selected to have $i_{AB} < 19.1$ in the earliest iteration of the survey, and are presented in the seventh data release (Schneider et al., 2010). The fourteenth data release (Pâris et al., 2018) presents spectra of more than half a million quasars, many of which are at much fainter magnitudes.

With such a large sample of objects, it is now possible to perform statistical analyses of objects with redshifts $z \simeq 2$, where the SDSS spectrograph covers the rest frame ultraviolet part of the spectrum. Richards et al. (2011) proposed that the properties of the C IV emission line could be used to classify quasars in a similar way to that done at lower redshifts with EV1. In Fig. 1.1, we show the blueshift and equivalent width of the C IV line in the SDSS quasars measured by Rankine et al. (2020). The two quantities are observed to anti-correlate, for both the population of quasars with broad absorption features and the population without.

The diversity of C IV emission properties is believed to be linked to variation in strength of the radiation field which is ionising the line emitting material. The lack of objects in the top-right corner of Fig. 1.1 is then explained by objects with harder spectra over-ionising the line emitting material such that stronger lines are observed but that the material loses the opacity required to drive strong outflows.

Richards et al. (2011) sought to classify quasars in a paradigm where the diversity of the broad emission lines is due to differences in the balance of 'wind' to 'core' emission, in a model where C IV is emitted from clouds of gas which are either outflowing in a wind or located at the systemic redshift. Such differences would be driven by the spectral energy distribution (SED) which is illuminating the BLR, which must ultimately be linked to the mass of the SMBH, the current accretion rate, the spin of the black hole and possibly the recent accretion history.

1.4.3 *Heavily reddened quasars*

Optical surveys like SDSS are, by design, going to identify unobscured quasars with blue continua. However, some of the most important AGN in the galaxy evolution paradigm described in Section 1.2.2 are expected to be obscured by dust, which attenuates their spectra to the extent that they are not detected in optical surveys.

Such heavily dust-reddened quasars have instead been identified in large area infrared surveys (Banerji et al., 2012, 2013, 2015; Temple et al., 2019). These objects were selected to have near-infrared colours consistent with the amount of dust reddening found in sub-millimetre bright galaxies (Takata et al., 2006), which are believed to host dust-obscured starbursts. Heavily reddened quasars are found to be as intrinsically luminous as the brightest objects from SDSS (Fig. 1.2). Four have been followed up with the Atacama Large Millimeter/sub-millimeter Array (ALMA; Banerji et al., 2017, 2018), finding high levels of both cold dust and molecular gas in their host galaxies, while Wethers et al. (2018) exploit the obscuration of the quasar light in the rest frame ultraviolet to investigate the host galaxy emission, finding evidence for high rates of ongoing star formation.

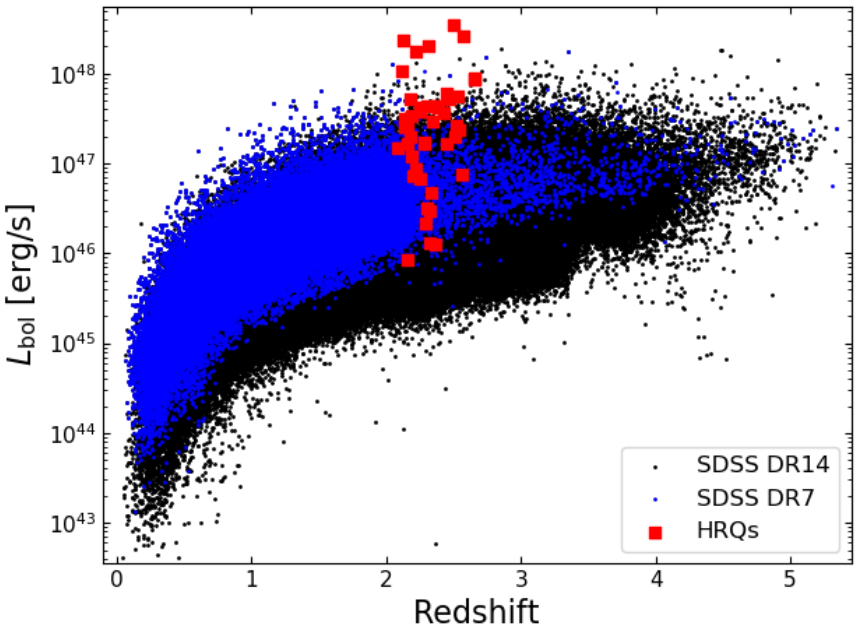

Figure 1.2: The distribution in the luminosity-redshift plane of (i) the 526 356 quasars from SDSS DR14, (ii) the subset of 79 487 quasars which were selected in SDSS DR7 to have $i < 19.1$, and (iii) 48 heavily reddened quasars with $z > 2$ selected from near-infrared surveys. Bolometric luminosities have been estimated using the corrections given in equation 1.9, having first corrected the observed monochromatic luminosities for the effect of dust extinction.

1.5 THESIS STRUCTURE

The structure of this thesis is as follows.

In Chapter 2, we use photoionisation models to investigate the properties of the gas which is emitting Fe III lines in quasar spectra. The properties of this emission are found to be linked to the C IV outflow properties.

Chapter 4 looks to see if there is a link between the BLR outflow properties and the obscuring toriodal material. To do this we first build a parametric quasar SED model in Chapter 3 which tells us about how we are finding quasars in large-area sky surveys.

In Chapter 5, we investigate the [O III] outflow properties in heavily dust-reddened quasars and compare to their unobscured counterparts. We use the kinematics of these outflows to place constraints on the role of dust in models of galaxy evolution.

Throughout this thesis, all emission line wavelengths and equivalent widths are identified in vacuum in units of Ångströms, unless otherwise stated. The first-person plural is adopted to match the usual style of scientific prose and does not imply any co-authorship beyond that declared in the preface and indicated in the text.

1.5.1 *Flux and Luminosity*

Throughout this thesis, a flat ΛCDM cosmology is assumed with $\Omega_m = 0.27$, $\Omega_\Lambda = 0.73$, and $H_0 = 71\,\mathrm{km\,s^{-1}\ Mpc^{-1}}$. This gives a luminosity distance

$$d_L = \frac{c}{H_0}(1+z)\int_0^z \frac{dz'}{\sqrt{\Omega_m(1+z')^3+\Omega_\Lambda}} \tag{1.7}$$

Rest frame monochromatic luminosities can then be calculated from observed fluxes via

$$L_\lambda = 4\pi\, d_L^2\,(1+z)\lambda f_\lambda \tag{1.8}$$

where f_λ is the flux density per unit wavelength at observed frame wavelength $(1+z)\lambda$.

When estimating Eddington fractions, the following bolometric corrections are used:

$$\begin{aligned} L_{bol} &= 5.15 \times L_{3000} \\ L_{bol} &= 8.0 \times L_{5100} \end{aligned} \tag{1.9}$$

Use of a single bolometric correction implies that all quasars have the same shape of SED, from the X-rays through to the radio, which is not true. In particular, it has been suggested that the ratio of hard X-ray to soft X-ray emission varies as a function of the accretion rate, with higher Eddington-fraction objects having stronger soft X-ray

emission, which would lead to a larger bolometric correction (Giustini and Proga, 2019; Jin, Ward and Done, 2012; Vasudevan and Fabian, 2007). The bolometric corrections we use therefore have associated uncertainties of at least 20 per cent, and could be biased as a function of Eddington ratio. However, these uncertainties are subdominant compared to the uncertainty on the estimate of the black hole mass we derive from a single epoch of spectroscopy for each object. The total uncertainty on the estimate of the Eddington fraction for any quasar in this thesis is a factor of around 2.5. In the case where there are additional uncertainties on the measurement of the intrinsic luminosity of an object, a higher estimate of the total uncertainty on L/L_{Edd} is stated in the text.

1.5.2 *Magnitude systems*

The use of a system of 'magnitudes' to quantify the apparent brightness of astronomical sources can trace its origins back to ancient Greeks, who classified stars in the night sky on a scale where the brightest stars had a value of zero, and the faintest objects visible to the naked eye had a value of six. This system was more rigorously defined by Pogson (1856), who described a logarithmic magnitude scale where a change of five magnitudes equated to a factor of 100 difference in brightness - thus one magnitude corresponds to a change in flux of a factor 2.512:

$$\begin{aligned} m_{\text{Pogson}} &= -5\log_{100}(f/f_0) \\ &= -2.5\log_{10}(f/f_0) \\ &= -a\ln(f/f_0) \\ a &= 2.5\log_{10}(e) = 1.08574 \end{aligned} \tag{1.10}$$

Throughout this thesis, we quote Pogson magnitudes on the Vega system for measurements from UKIDSS, VHS, VIKING and WISE

where f is the integrated flux of the source after passing through a given photometric filter, and f_0 is the equivalent integrated flux of a spectrum defined to have zero magnitude. In the case of infrared surveys this is usually the spectrum of the star Vega.

For SDSS, Lupton, Gunn and Szalay (1999) defined a new magnitude system using the inverse hyperbolic sine function:

$$m_{\text{SDSS}} = -a\left[\operatorname{asinh}\left(\frac{f}{2bf_0}\right) + \ln(b)\right] \tag{1.11}$$

recalling that $\operatorname{asinh}(x) = \ln(x + \sqrt{x^2+1})$, we see that

$$m_{\text{SDSS}} \simeq \begin{cases} -a\ln(f/f_0) & f > 2bf_0 \\ -a\left[f/(2bf_0) + \ln(b)\right] & f < 2bf_0 \end{cases} \tag{1.12}$$

For photometry from SDSS, we quote asinh magnitudes which approximate the AB system

Here b is a softening parameter which is chosen such that bf_0 is approximately equal to the 1-σ sky noise in the measurement of f.

Thus, for a well-detected source, the asinh magnitude will approximate the Pogson magnitude. For low S/N detections, the asinh magnitude is linear with flux, giving a meaningful quantity with well-defined error properties, even for sources with formally zero or negative flux (Lupton, Gunn and Szalay, 1999).

For predicted magnitudes from LSST and Euclid, we use Pogson magnitudes on the AB system

Most optical surveys employ the AB system, where zero magnitude is given by a flat reference spectrum

$$f_\nu = (\lambda^2/c) f_\lambda = 3631\,\mathrm{Jy} \tag{1.13}$$

which is very close to the zero points used by SDSS.[1]

1 https://www.sdss.org/dr16/algorithms/fluxcal#SDSStoAB

2

FE III EMISSION IN QUASARS

2.1 INTRODUCTION

Iron lines have long been recognised as an important component in the spectra of AGN. For example, emission from the Fe II ion has been identified as one of the major sources of cooling in the broad line region (BLR; Wills, Netzer and Wills, 1985) and an important contributor to the observed population variance within optical quasar spectra (the so-called 'eigenvector 1'; Boroson and Green, 1992). There is now an extensive literature investigating the properties of the low ionisation (16.2 eV) Fe II emission in quasars. Recent results of reverberation-mapping campaigns indicate that the Fe II emission originates in gas at distances comparable to, or larger than, the gas responsible for much of the hydrogen Balmer emission in both low and high luminosity AGN (e.g. Hu et al., 2015; Zhang et al., 2019).

Empirical iron templates such as those provided by Vestergaard and Wilkes (2001) have also identified Fe III (ionisation potential 30.6 eV) as a significant source of emission, which needs to be accounted for when modelling emission lines such as the C III] λ1909 blend. However, until recently the electronic energy structure of the Fe^{2+} ion was poorly known and so theoretical predictions for the Fe III line ratios and strengths were not accurate. Within the past few years, work by Badnell and Ballance (2014) has produced improved atomic data for Fe III which, for the first time, allows predictions to be made for the full emission line spectrum of this ion (Laha et al., 2017).

Previous observational studies of Fe III have focused on the complex of lines at ~2075 Å, which is relatively isolated and measurements are thus relatively straightforward. Fian et al. (2018) find evidence that the complex of Fe III lines at λλ2039-2113 is strongly microlensed in a sample of 11 gravitationally lensed high luminosity quasars, suggesting the line emitting region is no more than a few light days across. At lower luminosity, Mediavilla et al. (2018, 2019) suggest that the Fe III in NGC 5548 reverberates with a time scale of around three days, which is shorter than the predicted time of 10-20 days estimated for Fe II reverberation in the same object (Hu et al., 2015). Thus, over an extended range of luminosities, investigation of Fe III emission can probe the conditions of gas in quasars and AGN closer to the central ionising source than is the case for Fe II emission.

The structure of this chapter is as follows. In Section 2.2 we discuss the theory of the Fe^{2+} ion and constrain its excitation mechanism using existing high S/N composite spectra in the rest frame ultraviolet.

Spectra from SDSS provide the basis for an investigation of the statistical properties of Fe III emission in the population of high luminosity, $\log_{10}(L_{bol}/\,erg\,s^{-1}) \simeq 46.5$, quasars with redshifts $1.2 < z < 2.3$. In Section 2.3 we outline the selection of a sample of such objects from the DR14 catalogue to investigate the Fe III emission across the quasar population. Initial investigation of the sample is used to demonstrate the presence of Fe III emission with significant equivalent width at wavelengths ≃1850-2150 Å. The observation is used to motivate additional theoretical investigation in Section 2.4, where we present further results of CLOUDY models. The particular focus is to place constraints on the temperature, density and turbulence of the Fe III emitting gas. In Section 2.5 we then check the consistency of our preferred model with a more involved consideration of the Fe III emission properties using the full quasar sample. The implications for our understanding of quasar broad-line regions form the basis for the discussion in Section 2.6.

2.2 FORMATION OF FE III LINES IN AGN

These calculations were performed by G. Ferland

Spectral calculations are performed using version 17.02 of CLOUDY, last described by Ferland et al. (2017). Figure 2.1 shows the Fe III model now implemented in CLOUDY. Data are largely from Badnell and Ballance (2014) with experimental energies from the National Institute of Standards and Technology (NIST) atomic spectra database (Kramida et al., 2018) adopted where possible. Previous work on the Fe III ion is summarized by Badnell and Ballance (2014).

This chapter centres on Fe III UV34 (as defined by Moore, 1952) at λλ1895,1914,1926 resulting from the septet transition indicated in Fig. 2.1 and also the strongest Fe III multiplet indicated in the Vestergaard and Wilkes (2001) template. According to NIST the next higher septet is ^{7}D at 147 000 wavenumbers, a level not included in Badnell and Ballance (2014). Little is known about the emission properties of Fe III from the dense gas found near the centres of AGN and we begin with some fundamental considerations.

Lines can form via two processes, photoionisation or collisional ionisation. The key difference is in the gas kinetic temperature, with photoionised gas having a temperature set by energy balance, generally around 10^4 K (Osterbrock and Ferland, 2006), while the gas kinetic temperature is near the ionisation temperature of the ion in collisional equilibrium, around $10^{4.5}$ K for Fe^{2+} (Lykins et al., 2013).

Figure 2.2 compares the resulting emission spectra of a pure Fe^{2+} gas with a density of $n_e = 10^{11}$ cm^{-3}. Both spectra are from a 'unit cell', a cubic-centimetre of gas, to ensure that the spectrum is not affected by radiative transfer effects. An incident radiation field is not included in the collisional case so as to ensure a pure collisional model.

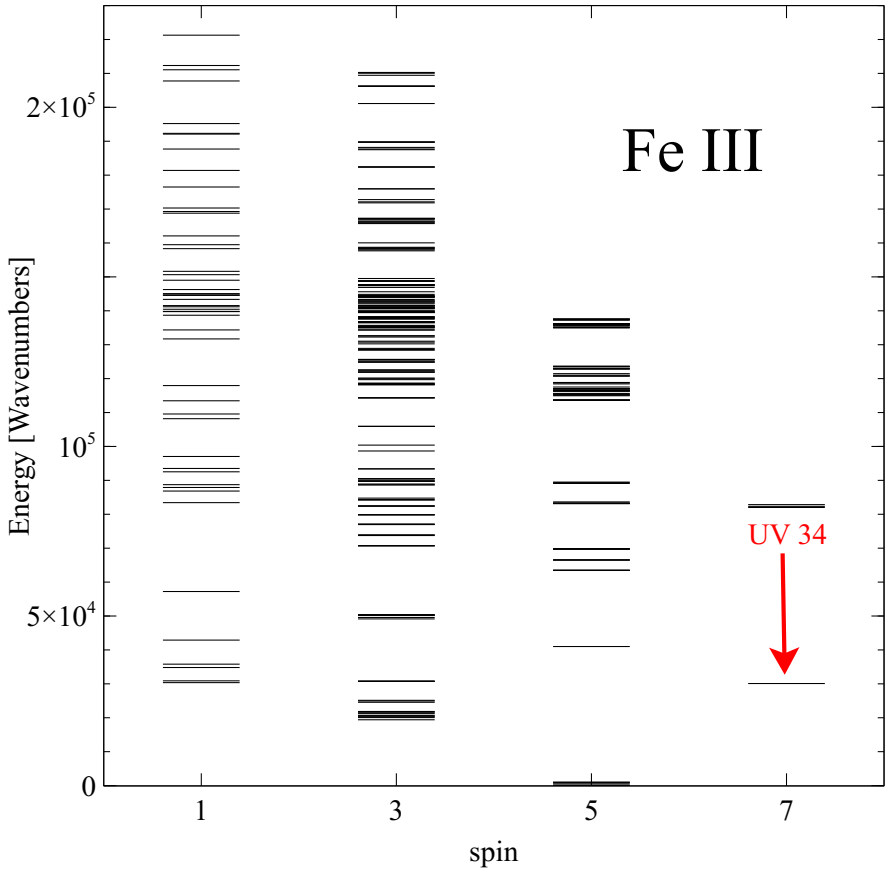

Figure 2.1: The Fe III model now implemented in CLOUDY. The UV34 transition studied in this chapter is indicated.

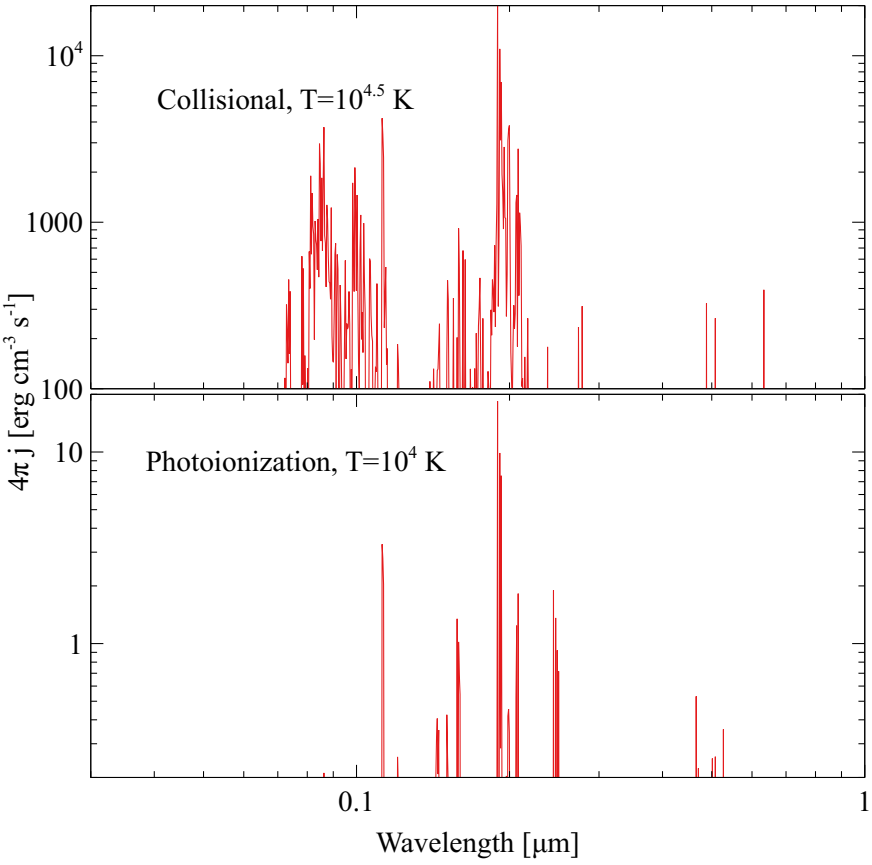

Figure 2.2: The Fe III emission spectrum for typical photoionisation (bottom) and collisional ionisation (top) temperatures. The gas has only Fe^{2+} and an electron density of 10^{11} cm^{-3}. The spectrum is from a unit cell in which the gas experiences only collisional excitation. The dynamic range of the y-axis is adjusted to only show lines brighter than one per cent of UV34.

The differences in the gas kinetic temperature for the two cases result in spectra of very different form. While the UV34 multiplet is strongest in both cases, electron collisions in the much warmer gas of the collisional ionisation model excite higher energy levels, producing emission at shorter ultraviolet wavelengths. In particular, there is significant emission just below 0.1 μm. The photoionisation case is much cooler so the gas is ≃3 dex less emissive (the independent axis in each panel can be compared directly) and short wavelength transitions are even weaker.

The difference in predicted Fe III emission strength below 1000 Å is such that existing ultraviolet spectra of luminous quasars can discriminate between a collisional and photoionisation origin for the iron emission. The composite quasar spectrum of Stevans et al. (2014, their fig. 5), constructed using *Hubble Space Telescope*-Cosmic Origins Spectrograph spectra of 159 AGN at $z < 1.5$, possesses both high S/N and high resolution (≃7500). The rest frame spectrum from the relatively low redshift AGN contributing to the composite is not significantly affected by Lyman absorption from the intergalactic medium.

Stevans et al. (2014) identify Fe III emission at 1125 Å, as predicted by both our photoionised and collisionally ionised models. The quality of the composite spectrum is such that weak emission features with equivalent widths of only a few Ångströms are detectable. Examination of their composite, however, confirms there is no evidence for Fe III emission in the 800-900 Å region, where we would expect to see strong emission if the Fe III emitting gas was collisionally excited (cf. our Fig. 2.2).

The first conclusion of this chapter is, therefore, that the observational evidence strongly favours the hypothesis that the ultraviolet Fe III emission in the spectra of luminous quasars arises from gas at 10^4 K over the hypothesis that such emission arises from $10^{4.5}$ K gas. In other words, there is no evidence for collisionally-ionised Fe III emission and a photoionised origin for the Fe III emission is strongly favoured. This is consistent with the reverberation of Fe III in response to continuum variation reported by Mediavilla et al. (2018, 2019).

While collisional ionisation can be ruled out as the physical process responsible for the observed Fe III emission, there is an apparent tension between the low emissivity of the Cloudy photoionisation model and the strong Fe III UV34 emission seen in the Vestergaard and Wilkes (2001) iron emission template. More quantitative measures of Fe III emission in the population of luminous quasars can constrain the Cloudy model predictions. In the next section, following the definition of the quasar sample to be used, we therefore make an initial measurement of the strength of Fe III UV34 and λ2075 emission to guide the theoretical investigation presented in Section 2.4.

2.3 OBSERVATIONAL QUASAR DATA

2.3.1 *Quasar sample*

To characterize the Fe III emission in the rest frame near-ultraviolet spectra of the luminous quasar population we use the quasar catalogue from the fourteenth data release of the SDSS (DR14; Pâris et al., 2018). Selecting objects with redshifts in the range $1.20 < z < 2.30$ provides rest frame wavelength coverage over the interval 1700-3000 Å which includes the C III] λ1909 blend, Mg II λ2800 emission and the complex of Fe III lines at ~2075 Å. The reliability of emission line measurements is poor for spectra of the fainter quasars in the DR14 catalogue and a minimum S/N of 10 per 69 km s^{-1} pixel over the wavelength interval 1700-3000 Å is imposed.

The resulting sample consists of 26 501 quasars with redshifts $1.20 < z < 2.30$ and luminosities $10^{45.8} < L_{bol} < 10^{48.1}$ erg s^{-1} . The median luminosity of the sample is $L_{bol} = 10^{46.4}$ erg s^{-1} .

For comparison with later results, we note that the median luminosity in the sample corresponds to C IV emission line lag of 73^{+21}_{-16} light-days behind the continuum, assuming the bolometric correction $L_{bol} = 3.81 \times L_{1350}$ from Shen et al. (2011) and the luminosity-lag relation from Grier et al. (2019),

$$\log_{10}\left(\frac{R_{C\,IV}}{\text{light-days}}\right) = 0.92 + 0.52 \times \log_{10}\left(\frac{L_{1350}}{10^{44}\,\text{erg s}^{-1}}\right) \pm 0.11 \quad (2.1)$$

corresponding to a source-cloud separation of 1.89×10^{17} cm for the C IV emitting gas.

2.3.2 *Defining the equivalent width of Fe III emission at 2075 Å*

A complex of Fe III transitions blends together to form a feature at ~2075 Å. This feature is relatively isolated, in that it is not blended with emission from other species, and can thus be used to estimate a measure of the strength of Fe III emission in a quasar spectrum.

The equivalent width of this emission feature can be obtained by defining a power-law continuum ($F(\lambda) \propto \lambda^{\alpha}$) and integrating the emission line flux within a specified wavelength range. The median fluxes in two 10 Å-wide intervals, centred on 1975 and 2150 Å, are used to calculate the slope, α, of the continuum. The continuum-subtracted emission is summed over the wavelength interval 2040-2120 Å. Different continuum regions and line-boundaries can be used but the results are not sensitive to the exact wavelengths adopted.

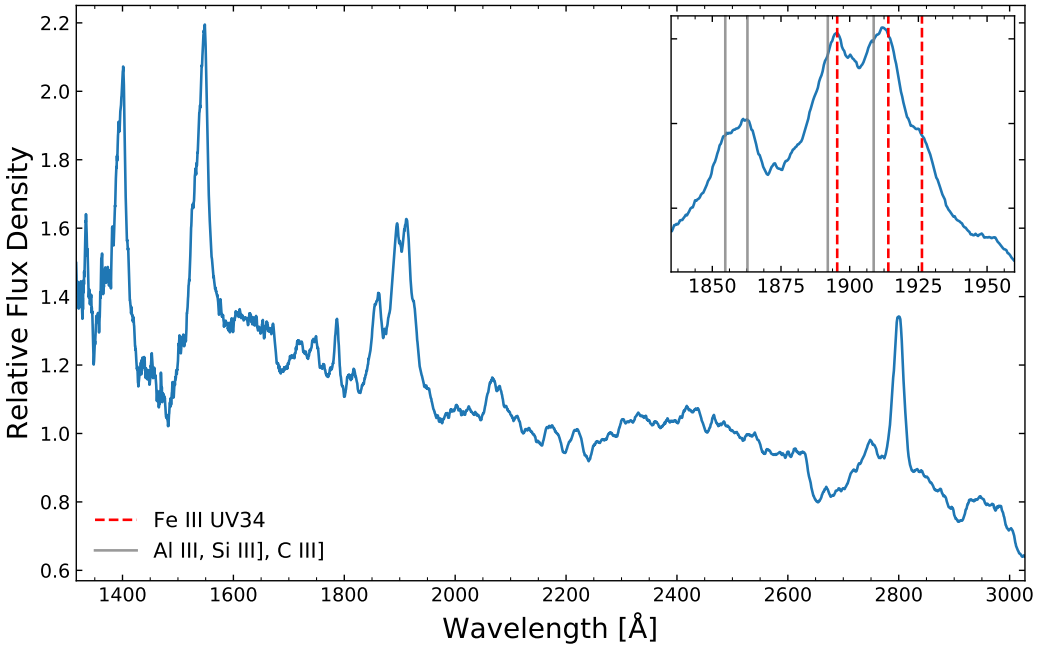

Figure 2.3: Composite of 44 quasars with narrow Mg II and and weak C III] emission. UV34 emission is directly detectable, and the composite also shows strong Fe III emission at 2075 Å. The C IV emission line is blueshifted with some weak absorption around 1500 Å. The spectrum has been smoothed with a 7-pixel (480 $\mathrm{km\,s^{-1}}$) window to reduce the pixel-to-pixel noise.
Inset: the 1909 Å complex, with the wavelengths of the Al III λλ1855,1863 doublet, C III] λ1909 and Si III] λ1892 lines, and Fe III UV34 multiplet marked.

2.3.3 *Directly detectable UV34 emission*

The diversity of the morphology of the '1909 Å complex' among luminous quasars is well-established (e.g. Richards et al., 2011, fig. 11). This strong feature consists of the Al III λλ1855,1863, Si III] λ1892, C III] λ1909 and Fe III UV34 emission lines. In most objects, these lines are blended together and it is hard to disentangle the relative contribution of UV34 from the semi-forbidden lines without additional constraints on the line ratios. However, in objects with narrow emission velocity widths, such as the quasar presented by Graham, Clowes and Campusano (1996), the individual lines contributing to the 1909 Å complex deblend and can be directly detected.

Within our sample of quasars it is possible to identify small numbers of objects where the FWHM of Mg II is narrow (< 2800 km s^{-1}) and the C III] λ1909 emission is relatively weak. Figure 2.3 shows a composite of 44 such quasar spectra, where the objects contributing to the composite have an average black hole mass of $10^{8.6}$ M$_\odot$ and an average Eddington fraction of 0.7. While the definition of their sample differs somewhat, the quasars contributing to our composite are very similar to the extreme 'Population A' objects discussed by Marziani and Sulentic (2014). Within this composite, we see that the emission doublet from Al III is detectable at the expected wavelengths, and that Si III] λ1892 and C III] λ1909 are very weak. The Fe III UV34 multiplet and Al III λλ1855,1863 are responsible for the majority of the emission, demonstrating that in at least some quasars Fe III UV34 is present with high, $\gtrsim 5$ Å, equivalent width.

However, for the majority of quasars, the Al III, Fe III UV34, Si III] and C III] lines are blended together. At the typical S/N of available large samples of quasar spectra, such as those from SDSS DR14, significant degeneracies exist between measures of the strengths of emission from these species. We therefore require additional constraints on the Fe III emission lines in order to be able to quantify the strength of UV34 across the whole quasar population.

We note in passing that the composite also shows strong Fe II UV191 λ1787 emission, which is indicative of strong continuum fluorescence (i.e. photon pumping, Bottorff et al. 2000), suggesting that this excitation mechanism may also play an important role in the production of Fe III emission.

Before returning to a more extensive investigation of the observational properties of Fe III emission in Section 2.5, we first make use of the improved atomic data now implemented in Cloudy to produce theoretical predictions for the strengths of these lines emitted from gas under different physical conditions.

2.4 PHOTOIONISATION CALCULATIONS

The photoionisation calculations in this section were also carried out by G. Ferland

This section presents predictions of the equivalent widths of a number of ultraviolet lines over a broad range of cloud densities and distances from the black hole. Our calculations extend to higher densities than conventional BLR grids (e.g. Baldwin et al., 1995; Korista et al., 1997). We find that the Fe III lines trace especially high density gas that is located close to the black hole. The Fe III energy level diagram (Fig. 2.1) is highly unusual in that the strongest permitted line, UV34, is a subordinate line that has a different spin than the ground term. Most ultraviolet lines are instead resonance lines and become strongly thermalised at high densities either because of large optical depths or low critical densities. They are weak at high densities as a result. Although the dense clouds do emit in other lines, their contribution is modest compared to emission from lower density components of the BLR. As Fe III emits only very weakly from lower density gas, we find that Fe III is the best tracer of the high density part of the BLR.

2.4.1 *Photoionisation model parameters*

We present a first grid of photoionisation models assuming that lines within the clouds are broadened only by thermal motions, the usual assumption in BLR modeling, and a second grid including a microturbulence of 300 km s^{-1} which Baldwin et al. (2004) found improved the fit for the Fe II spectrum. The effects of including turbulence on other quasar emission lines are described by Bottorff et al. (2000).

We use the intermediate L/L_{Edd} SED described by Jin, Ward and Done (2012). We assume solar abundances and a cloud column density of 10^{23} cm^{-2} , typical assumptions for BLR clouds. With these assumptions the remaining parameters are the flux of ionising photons striking the cloud, $\phi(H)$[cm^{-2} s^{-1}], and the hydrogen density n_H[cm^{-3}]. In Figs. 2.4 and 2.5 we vary these parameters over a broad range. Plots similar to these are presented in Baldwin et al. (1995), Korista et al. (1997), and Baldwin et al. (2004).

The following features are presented: C IV λ1549, Al III λ1860, Si III] λ1892, C III] λ1909, C III λ2297, Mg II λ2798, Fe II ultraviolet emission over the interval 2200-2660 Å ('Fe II UV'), and Fe III UV34. All features are shown as equivalent widths in Ångströms expressed relative to the continuum at 1215 Å, and assuming 4π sr coverage of the ionising source, i.e. a cloud covering factor of unity. In the case of multiplets or blends we predict the total equivalent width. However, the line luminosity or equivalent width depends on the cloud covering factor (Osterbrock and Ferland, 2006), and so these predictions need to be multiplied by that factor, which is typically taken to be of the order of 20 per cent. Adopting this value, an observed Fe III UV34 equivalent

width of 5 Å requires a predicted equivalent width of the order of 25 Å.

The two axes for these contour plots have simple physical meanings. The flux of ionising photons $\phi(H)$ is related to the total ionising photon luminosity, $Q(H)$ [s^{-1}] and the distance of the cloud from the continuum source r by

$$\phi(H) = \frac{Q(H)}{4\pi r^2} [\mathrm{cm}^{-2}\ \mathrm{s}^{-1}] \tag{2.2}$$

so the vertical axis is related to the cloud separation from the centre, $\phi \propto r^{-2}$ with lower regions representing larger radii. The typical bolometric luminosity of our sample is $10^{46.4}$ erg s^{-1}. This, assuming the middle SED of Jin, Ward and Done (2012), corresponds to a photon luminosity of $Q(H) = 1.96 \times 10^{56}\,s^{-1}$. For reference, C IV emitting clouds, adopting a lag of 73 light days, have

$$\phi(H) = 4.36 \times 10^{20} r_{73.6}^{-2} [\mathrm{cm}^{-2}\ \mathrm{s}^{-1}], \tag{2.3}$$

where $r_{73.6}$ is the radius in light days and we assume that the radiation field falls off as an inverse square law. Lower ionisation photoionised clouds that emit strongly in the ultraviolet and optical have kinetic temperatures in the neighbourhood of 1-2$\times 10^4$ K so the horizontal axis is an approximate surrogate for the gas pressure. We see that the source-cloud separation varies by nearly 4 dex while the gas pressure varies by 8 dex.

Intermediate ionisation lines such as C IV and Al III peak along a diagonal corresponding to particular values of the ionisation parameter

$$U = \frac{\phi(H)}{c\, n_H}. \tag{2.4}$$

Very low ionisation lines such as Fe II and Mg II do not show such a peak but rather favour lower $\phi(H)$ and larger r.

2.4.2 *Implications of the Fe III equivalent width: a turbulent dense medium*

The energy level diagram shown in Figure 2.1 suggests that UV34 is an odd choice for the strongest Fe III line. The multiplet has a high excitation potential, with its upper level at 82 000 wavenumbers (10.2 eV). Direct excitation from the ground term is via forbidden transitions and so is not very efficient. Tests show that efficient excitation of UV34 is via a two-step process, with excited quintet levels playing an intermediary role.

Several Fe III levels are close enough to the Lyα energy of 82 259 wavenumbers for Lyα pumping to be significant. This is included in CLOUDY as a general line excitation process and completes with direct continuum photoexcitation. Both processes will photoexcite the

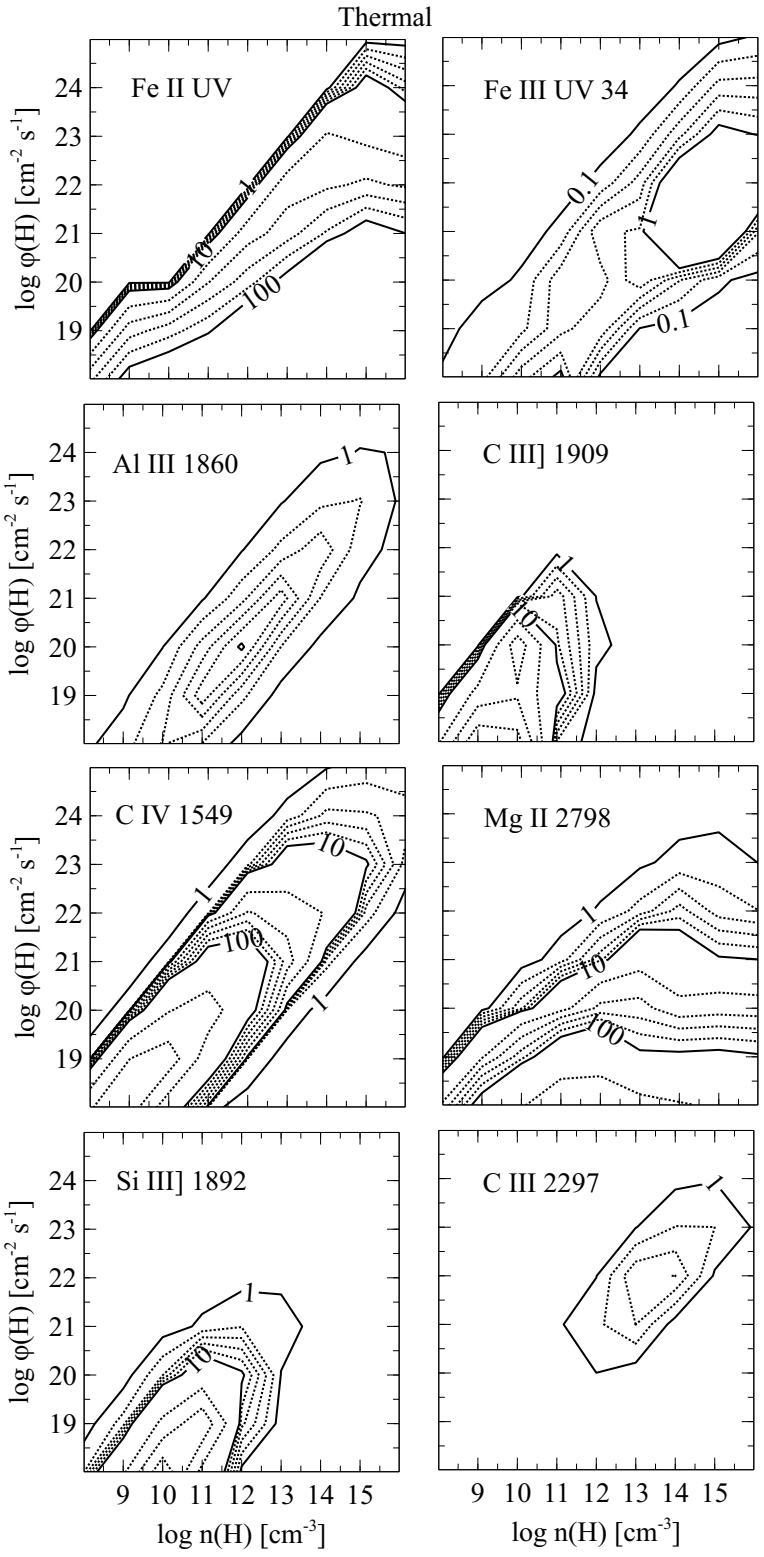

Figure 2.4: The ensemble of possible photoionisation models for thermal line widths. Contours show the predicted equivalent widths in Ångströms relative to the continuum at 1215 Å for each emission feature, assuming a covering factor of unity. The integrated Fe II ultraviolet emission over the interval 2200-2660 Å is reported as a single feature.

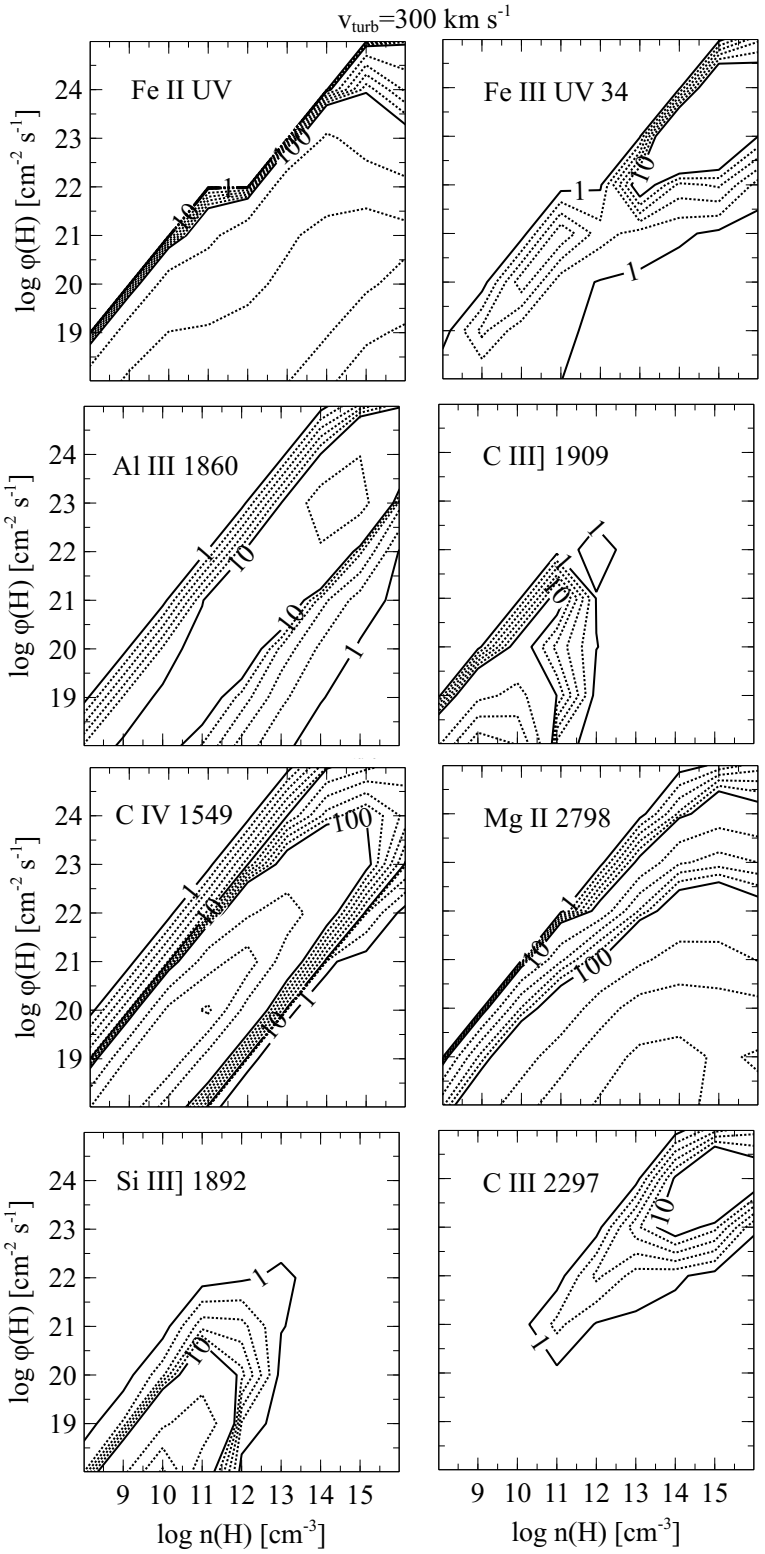

Figure 2.5: The ensemble of possible photoionisation models, with microturbulence of 300 km s^{-1}. Contours show the predicted equivalent widths in Ångströms relative to the continuum at 1215 Å for each emission feature, assuming a covering factor of unity. Axes are identical to Fig. 2.4 and so the contours can be compared directly.

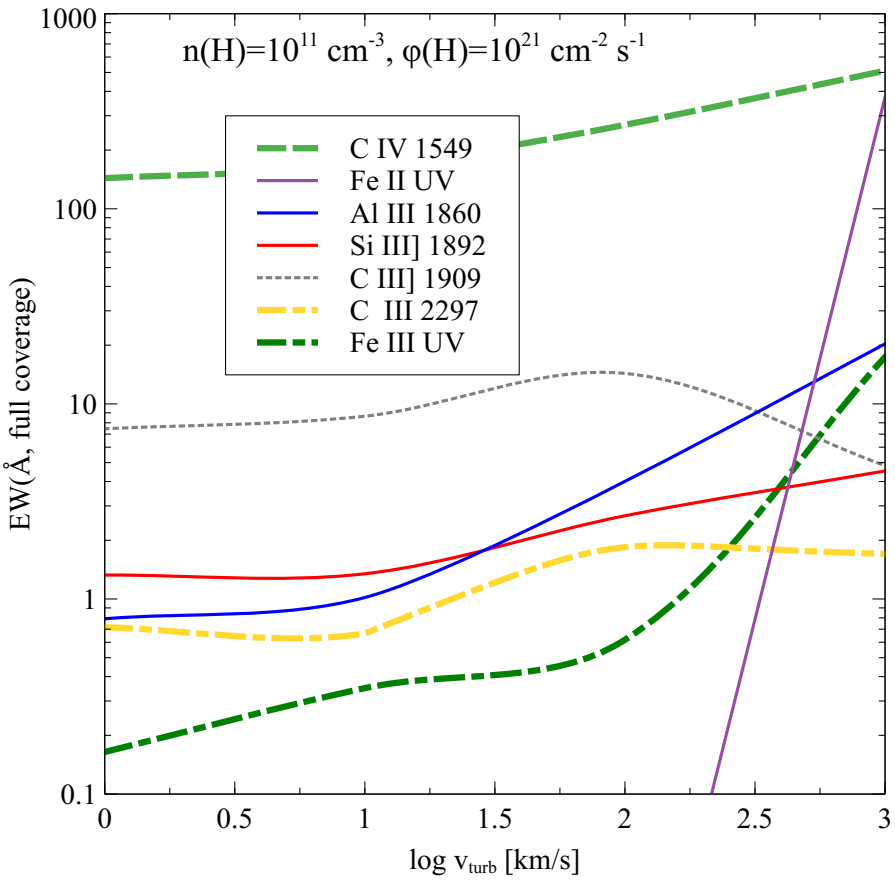

Figure 2.6: The effects of varying turbulence upon the equivalent widths of several prominent lines. Both Fe III and Fe II are predicted to produce much stronger emission as the turbulent velocity parameter increases.

septets since these are connected to ground by an allowed electric dipole transition. However, the fact that the spectrum is sensitive to the turbulence, which affects continuum pumping more than line overlap, shows that continuum fluorescence is more important than Lyα pumping.

The effects of varying the turbulence are shown in Fig. 2.6. Increasing the turbulence increases the importance of continuum pumping because the line width increases and so do the number of continuum photons that can be absorbed by a transition (Section 2.1 of Ferland, 1992). Physically, increased continuum pumping increases the population of excited quintets which can then undergo a collisional transition to the septets.

We note that, as discussed in Baldwin et al. (2004), the turbulence implemented in CLOUDY describes any situation in which the wavelengths of the emitting lines are shifted or broadened over a physical distance corresponding to the mean free path of a continuum photon. Such

velocity differences could naturally arise from differential rotation or instabilities within the accretion disc. We see no evidence for kinematic structure within the Fe III lines to suggest that the Fe III emitting material is itself outflowing, and so we do not believe that the turbulence needed to account for the observed strength of the Fe III emission is due to velocity gradients in ordered outflows as would be expected if the Fe III emitting material was entrained in a wind off the accretion disc.

Adopting a value of $v_{turb} = 300\,km\,s^{-1}$ for the microturbulence parameter, we find that the predicted equivalent width of Fe III emission is still significantly weaker than that observed in quasar spectra. Varying the metallicity of the emitting gas has an insufficient effect on the predicted equivalent width for the strength of Fe III in AGN to be explained by non-solar iron abundances. However, as shown in Figs. 2.4 and 2.5, the Fe III emission peaks at a density of $\simeq 10^{15}\,cm^{-3}$, irrespective of the microturbulence. In Fig. 2.7, we show how the equivalent widths of various lines change as a function of density, taking a diagonal slice through the $\phi(H) - n_H$ plane corresponding to the ridge of peak C IV and Al III emission and constant ionisation parameter.

The only way in which we can account for the observed strength of the Fe III emission is through turbulent, high density gas with $n_H > 10^{13}\,cm^{-3}$. Taken with the upper limits on the density of the gas which is producing the semi-forbidden lines such as C III] λ1909 in quasar spectra, this is strong evidence for multiple components of differing densities contributing to the region which is producing the broad emission lines in AGN.

2.4.3 *How dense is the turbulent dense medium?*

In the previous subsection, we have shown that emission from a turbulent medium with density $n_H > 10^{13}\,cm^{-3}$ is required to reproduce the observed Fe III line strengths. To better constrain the density of this medium, we use the predicted strengths of the C III emission lines shown in Fig. 2.8.

As shown in Fig. 2.7, the strength of the semi-forbidden C III] λ1909 line drops drastically above $n_H \simeq 10^{12}\,cm^{-3}$. We show in Section 2.5 that the C III] λ1909 emission in our sample of SDSS quasars is independent of the Fe III UV34 emission, consistent with emission from at least two distinct locations around the black hole.

The C III λ2297 line is predicted to be strong when the density is above $n_H \simeq 10^{14}\,cm^{-3}$ (Fig. 2.7). However, to the best of our knowledge, the line is not detected in the spectrum of any quasar. In particular, C III λ2297 is not present in the high S/N composites of Vanden Berk et al. (2001) and Francis et al. (1991), or the ultraviolet spectrum of I Zw 1 presented in Vestergaard and Wilkes (2001). We therefore use

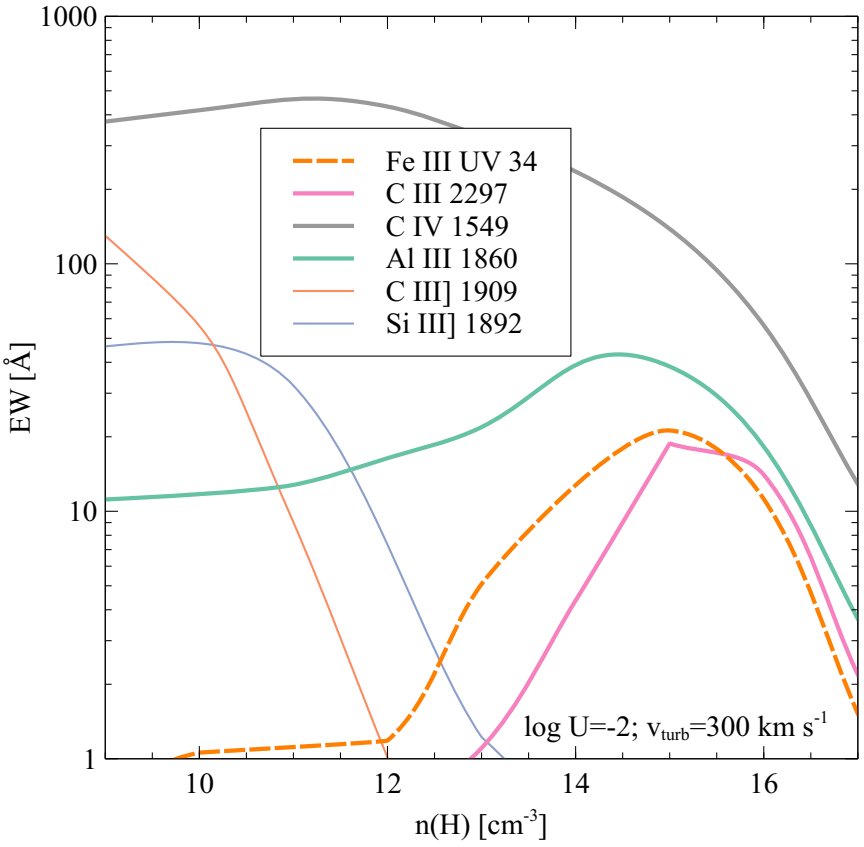

Figure 2.7: The effects of varying hydrogen density along the ridge of peak C IV emission strength, keeping the ionisation parameter constant. C III] λ1909 and Si III] λ1892 produce very little emission above 10^{13} cm^{-3}, where both Fe III UV34 and Al III λ1860 are predicted to peak. C III λ2297 is predicted to be strong above 10^{14} cm^{-3}, but this line is not observed in quasar spectra.

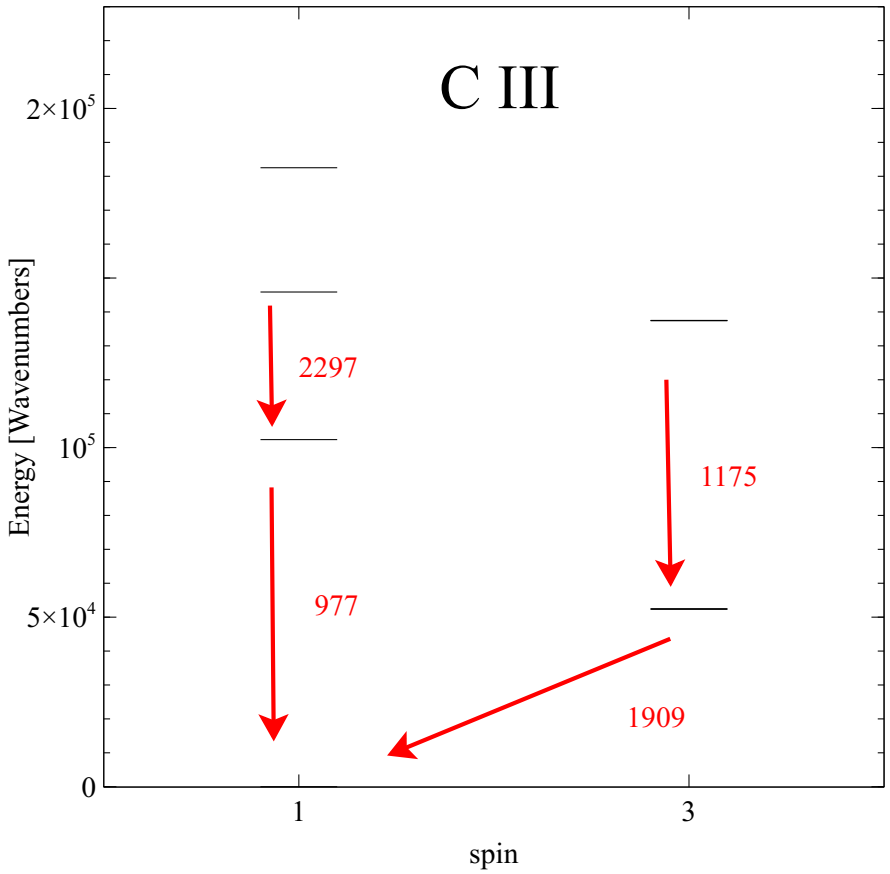

Figure 2.8: The C III model implemented in CLOUDY. Only the lower levels are shown to keep the energy scale the same as Fig. 2.1. The strong C III lines are indicated.

the observed lack of C III λ2297 emission to constrain the density of the Fe III emitting gas to lie in the range $n_H = 10^{13-14}$ cm^{-3}.

2.5 COMPARISON WITH OBSERVATIONS

With theoretical predictions from CLOUDY in hand, we can now use the full sample of spectra described in Section 2.3.1 to test our preferred model for the dense turbulent medium required to reproduce the observed Fe III.

2.5.1 *Measuring Fe III UV34 in quasar spectra*

As shown in Figs. 2.6 and 2.7, the dense turbulent medium will also produce a significant amount of Al III λλ1854.72,1862.79 emission. For each of the 26 501 quasars in our sample, we fit the Al III doublet with two Gaussians, with the ratio of the lines constrained to be 2.3866 : 1.9162, and compare with the strength of the Fe III λ2075

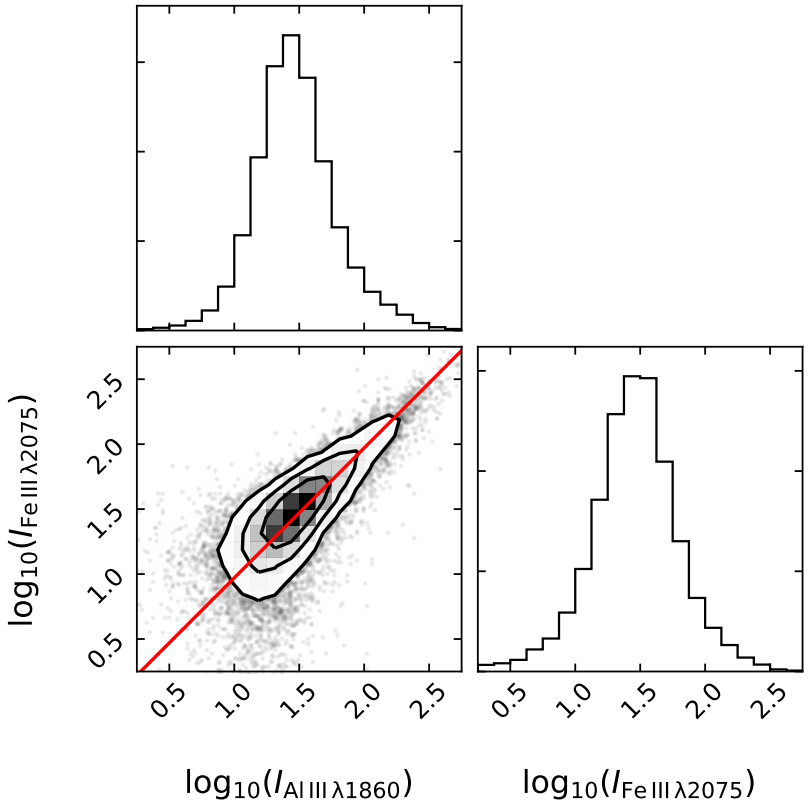

Figure 2.9: The observed intensities of the Al III doublet and Fe III λ2075 complex in units of 10^{-17} erg s^{-1} cm^{-2}. In red is the predicted ratio from the dense turbulent CLOUDY model, which agrees very well with the slope of the observed correlation. The observed emission is consistent with the line ratio expected if both lines are produced in the same dense turbulent medium.

complex described in Section 2.3.2. The results are shown in Fig. 2.9: the strength of the Al III doublet clearly correlates with the strength of the Fe III λ2075. The ratio of the line intensities of the two complexes is in agreement with the predictions of our dense turbulent model.

Encouraged by this, we fit the λ1909 complex with a model which describes the relative contribution of the aluminium, iron, carbon and silicon lines.

For each object, a power-law in flux is defined at 1800 and 2020 Å and subtracted from the spectrum. The wavelength region 1820-1920 Å is then fit with a sum of seven Gaussians described by four free parameters: (i) the amplitude of the Al III and Fe III UV34 component, (ii) the amplitude of the Si III] line, (iii) the amplitude of the C III] line,

and (iv) the velocity width of the lines. The Al III doublet and Fe III UV34 triplet are constrained to have the line ratios

$$\begin{aligned}\lambda1854.72 : \lambda1862.79 : \lambda1895.46 : \lambda1914.06 : \lambda1926.30 \\ = 2.3866 : 1.9162 : 0.9910 : 0.7538 : 0.6945 \end{aligned} \quad (2.5)$$

as predicted for a dense, microturbulent, photoionised gas[1] with solar abundances. In theory the Si III] and C III] lines would be expected to have narrower profiles than the Al III and Fe III, as they are coming from gas which is less dense and thus located further from the black hole. In practice the S/N of the spectra are such that allowing the velocity widths of the lines to vary independently leads to an over-fit to the data. We therefore constrain the velocity widths of all lines in our fitting routine to be equal, which gives a more robust estimate of the equivalent width of each line in the complex. Examples of our best-fitting models are presented in Fig. 2.10.

2.5.2 *Implications for C III] and Si III]*

The improved atomic data and CLOUDY model presented above now allow a more certain estimate of the UV34 multiplet to be made in any given quasar spectrum, even when the multiplet is completely blended with other lines. This allows, for the first time, an accurate measurement of the C III] and Si III] emission to be made in objects with a significant contribution from Fe III UV34.

Using our dense turbulent model for Fe III emission to fit the λ1909 complex, with independent contributions from Si III] and C III], we measure the equivalent widths of the Si III], C III] and Fe III lines in our sample of SDSS quasars. The results are shown in Fig. 2.11. We find that the Fe III emission correlates with the Si III], but that the C III] emission is essentially uncorrelated with either species. This is consistent with the expected behaviour of C III] λ1909, which must be coming from gas of a significantly lower density than that which is emitting the Fe III (see Section 2.4.3).

The Si III] strength does however correlate with the strength of the Fe III UV34, suggesting that some of the observed silicon emission could also be coming from the dense turbulent component. The observed C III]:Si III] ratio thus correlates with Fe III and could therefore be an indicator of the hardness of the SED which is illuminating the BLR, as suggested by Casebeer, Leighly and Baron (2006) and Richards et al. (2011).

The median equivalent widths of emission in our sample are 2.58, 9.95, 5.97, and 4.43 Å for Fe III UV34, C III], Si III], and Al III respectively; the average strength of Fe III UV34 is ≈0.16 times the combined strength of C III] and Si III]. 83 per cent of the quasars in our sample

1 $v_{turb} = 300\ \mathrm{km\,s^{-1}}$, $n_H = 10^{14}\,\mathrm{cm^{-3}}$, $\phi = 10^{23}\,\mathrm{cm^{-2}\ s^{-1}}$

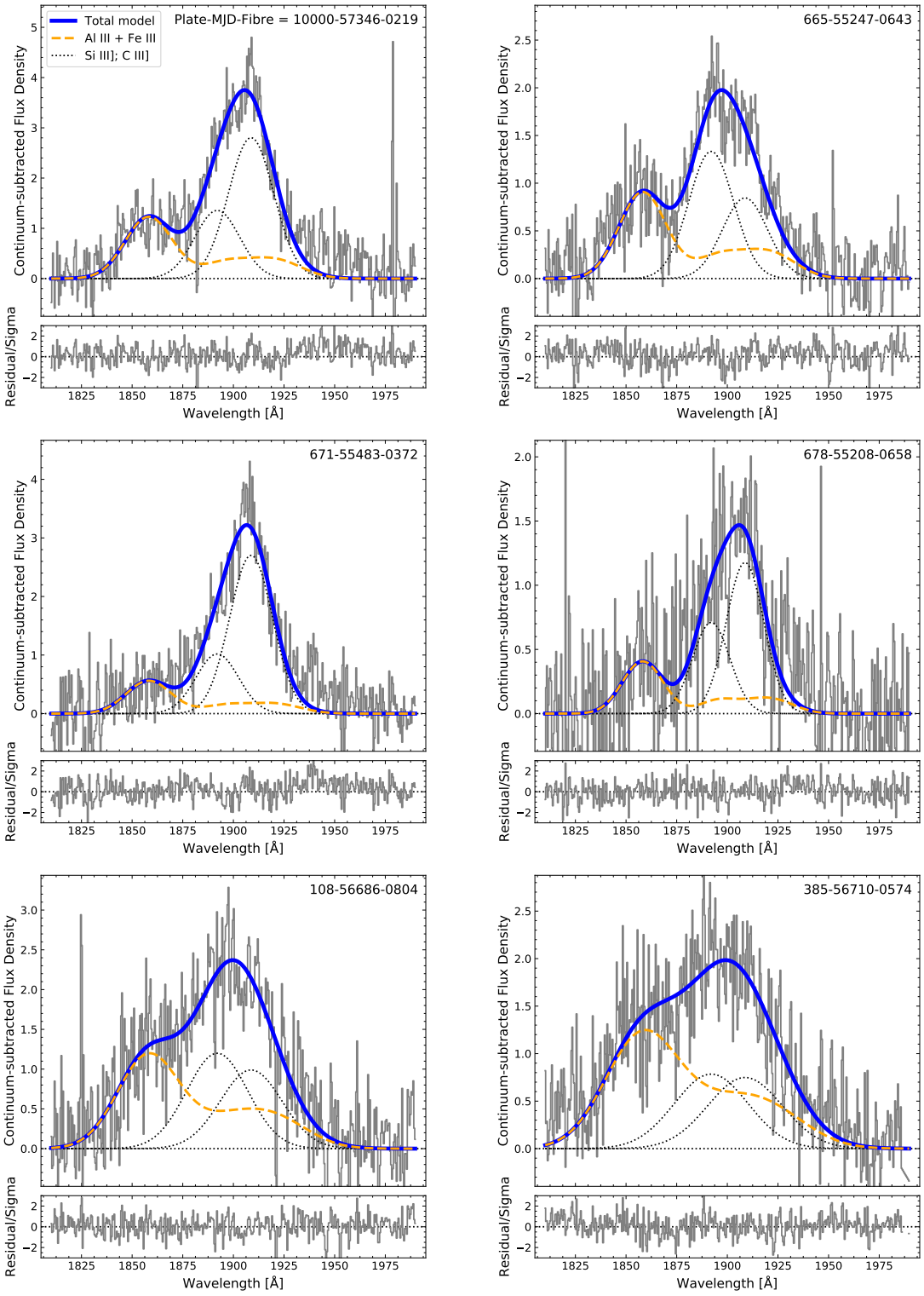

Figure 2.10: Six examples of our best-fitting models to the 1909 Å complex. Each model is fit to the data in the wavelength range 1820-1920 Å, avoiding contamination from weak Fe II emission features at ≃1940 Å. The C III] emission may be slightly narrower than the Al III and Fe III emission in e.g. 671-55483-0372, but in general the S/N is such that constraining the velocity widths of all lines to be equal provides a reasonable fit to the data.

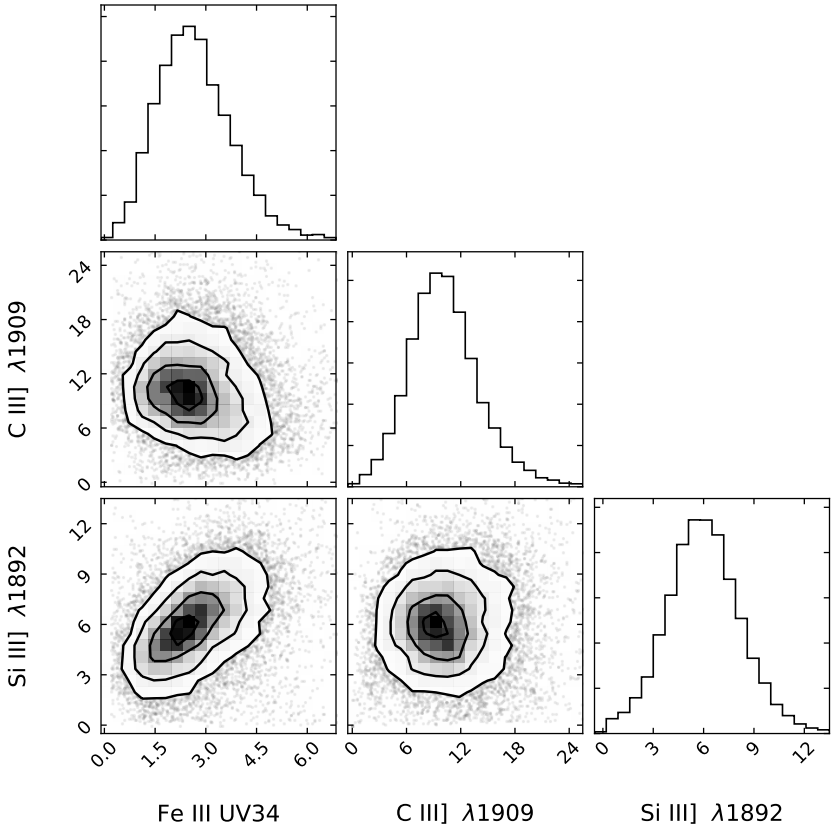

Figure 2.11: Observed equivalent widths in Ångströms for the three components of the λ1909 complex, relative to the continuum at 1900 Å. When the Fe III UV34 emission is incorporated into the fit to the complex, we find that the C III] emission strength is uncorrelated with that of Si III].

have UV34 fluxes which are greater than 0.1 times the sum of flux in C III] and Si III]. This highlights the need for accurate modeling of UV34 when attempting to measure C III] and Si III] line properties.

2.5.3 *Broad absorption line quasars*

The absorption line properties of the 19 590 quasars in our sample with $z > 1.56$, where spectral coverage of the C IV emission line is available, are classified as part of the Rankine et al. (2020) investigation into broad absorption line (BAL) quasars. The classification of objects as BAL quasars from this subsample produces 16 148 non-BAL and 3048 high ionisation BAL quasars. We exclude 394 low ionisation BALs with broad Al III troughs from subsequent analysis.

Following the same scheme as described above, we find no significant difference between the high ionisation BALs and non-BALs, in that the high ionisation BALs also require a high density, turbulent component to account for the Fe III emission in their spectra.

2.5.4 *Comparison with Vestergaard & Wilkes (2001)*

In this section we compare our Fe III UV34 multiplet with those presented in the templates of Vestergaard and Wilkes (2001).

Vestergaard and Wilkes (2001) discuss the blending of UV34 with the C III] and Si III] lines and the degeneracies arising when attempting to fit multiple overlapping lines simultaneously due to the non-orthogonality of Gaussian functions (their section 5.1). Due to the lack of atomic data at the time, they were unable to place theoretical constraints on the UV34 line ratios and thus provided a range of ratios which were consistent with the observed emission. Their published ratios range from the optically thick case where the lines thermalise at 1:1:1, to their preferred values of 0.375:1:0.425 based on the observed strength of the λ1914 line in I Zw 1.

Using the new atomic data and the dense turbulent CLOUDY model presented above, we are now able to predict the ratios of the λλ1895.46, 1914.06, 1926.30 Fe III lines in quasar spectra. Assuming a dense, microturbulent, photoionised gas with solar abundances, we find UV34 line ratios of 1.316:1:0.921.

Our preferred Fe III model therefore predicts stronger λ1895 emission relative to λ1914 than any of the models presented by Vestergaard and Wilkes (2001), but we believe our line ratios are still consistent with those they observe in I Zw 1 within the uncertainties they discuss.

2.5.5 *Comparison with Mediavilla et al. (2018, 2019)*

The systemic redshifts used in this chapter are those described by Rankine et al. (2020), which do not make use of the C IV line. This

approach avoids biasing the systemic redshift estimation in cases where the C IV emission profile is skewed, which we have found to be an issue with the SDSS pipeline redshifts. Using our redshifts, and the Fe III energy level data now included in CLOUDY, we find that the Fe III emission in our sample is consistent with coming from gas at the systemic redshift. In particular, we are unable to reproduce the result of Mediavilla et al. (2018), who find that the Fe III λ2075 emission lines are systematically redshifted, and the magnitude of this additional redshift is correlated with the FWHM of the C IV emission line.

In Fig. 2.12, we show composite spectra constructed from those objects in our sample which are also contained within the twelfth data release of the SDSS, of which the quasar catalogue (Pâris et al., 2017) reports the FWHM of the Mg II emission line. We construct two composites: one using 375 objects with FWHM(Mg II) in the range $2000 - 4000\,\mathrm{km\,s^{-1}}$, and one using 967 objects with FWHM(Mg II) in the range $9000 - 15,000\,\mathrm{km\,s^{-1}}$. The median FWHM(Mg II) in each subsample is 3800 and $10,200\,\mathrm{km\,s^{-1}}$ respectively. The narrow-lined composite is artificially broadened using a Gaussian kernel to match the velocity width of the broader lined subsample. The work of Mediavilla et al. (2019, their Fig. 2) would suggest that the factor of $\simeq$2.7 difference in FWHM(Mg II) would correspond to a shift of at least 10 Å in the location of the Fe III lines between the two composites, which we would expect to be easily detectable. We see that the peak of Mg II is observed at 2798 Å in both our composites, and there is no noticeable difference between the peak of the Fe III complex marked at 2073.5 Å.

2.6 DISCUSSION

2.6.1 *High Densities*

It is perhaps surprising to see that significant line emission from Fe III and Al III is predicted from gas illuminated by such high ionising fluxes. Our favoured model for the Fe III emitting gas has an ionising photon flux $\phi = 10^{23}\,\mathrm{cm^{-2}\,s^{-1}}$, which suggests that this part of the BLR must lie very close to the central black hole. While this is consistent with the existing reverberation-mapping studies in the literature (see Section 2.1), we would expect this locale to have large Keplerian speeds - the 4 dex difference in ϕ gives a 2 dex difference in radius and hence v_{Kepler} a factor 10 greater compared to the gas which is most likely emitting C III].

We would expect such an extreme difference in the velocity width of the emission lines to be easily observable, however, no such difference is seen in the objects in our sample. The spectral resolution and S/N constraints are such that, while we cannot rule out variation between the velocity widths of each species within individual objects at the

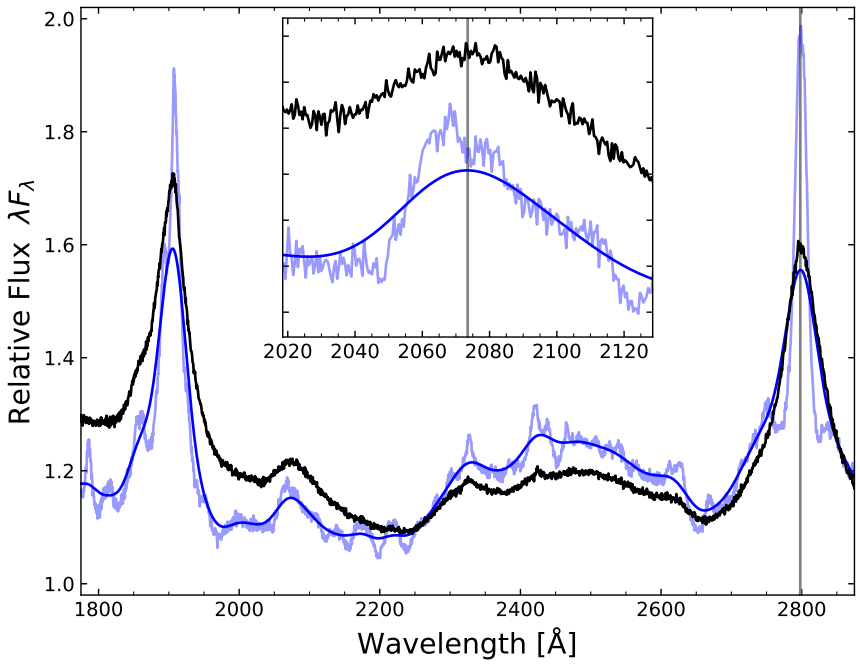

Figure 2.12: Composites of objects in our sample with FWHM(Mg II) $\simeq$ 3800 km s^{-1} (blue) and $\simeq$ 10,200 km s^{-1} (black). The narrow-lined composite has been broadened with a Gaussian kernel to match the velocity widths.
Inset: the peak of the Fe III complex is seen at at 2073.5 Å in both composites.

level of tens of per cent, the Si III] and C III] lines are no more than a factor 2 narrower than the Al III lines in any given object in our sample.

One explanation for this is if the dense turbulent gas which is emitting Fe III is primarily undergoing equatorial motion. For a Type-1 quasar, this would mean that the majority of the motion of the line emitting gas is in the plane of the sky, and the observed velocity dispersion along the line of sight is smaller than the Keplerian speed. This would suggest that the dense media we require to explain the strength of the observed Fe III emission are found in quasi-ordered flows in the equatorial regions of the AGN.

2.6.2 *Correlations with C IV properties*

The high ionisation C IV λ1549 emission line exhibits a large range of kinematic morphologies, from strong, 'peaky' emission at the systemic redshift which is believed to be dominated by emission from gas in virial equilibrium, to weaker and highly blueshifted emission tracing outflowing material. However, the physical mechanisms which set the balance of these emitting components are not well understood, despite the fact that the C IV morphology is known to be closely tied to other parameters such as the Eddington ratio and the hardness of the SED which is ionising the BLR (Rankine et al., 2020; Richards et al., 2011). Here we note certain correlations using the results of the modelling of the λ1909 complex described in Section 2.5.

The measured strength of the Fe III and Al III component tends to increase as the blueshift of the C IV line increases (Fig. 2.13), suggesting that objects with stronger wind emission are likely to display stronger emission from the dense turbulent medium. This is consistent with the results from the sample of seven objects studied by Baldwin et al. (1996). However, the Fe III line profiles do not themselves show any evidence for outflows, and so we do not believe that the dense ($\simeq 10^{14}$ cm^{-3}) Fe III emitting gas is being accelerated within a wind.

One possible explanation for the correlation between the strength of the Fe III UV34 emission and the increasing blueshifted C IV emission, tracing outflowing lower density material, might be the range of Eddington fractions within the population, which is one of the commonly quoted drivers of variation in C IV line properties. Quasars with larger Eddington fractions potentially 'puff up' the inner regions of the accretion disc (e.g. Giustini and Proga, 2019), leading to a larger volume of high density line emitting gas close in to the black hole. The increased Eddington fraction also leads to stronger radiation line-driven winds. However, inferring L/L_{Edd} from single-epoch spectra is fraught with large systematic uncertainties, deriving both from the use of a single bolometric correction to estimate L_{bol} from a monochromatic luminosity, and also the use of a virial factor to estimate the black

hole mass from a single emission line velocity width. Here we use the FWHM of the Mg II λ2800 line and the single-epoch virial estimator described by Vestergaard and Osmer (2009) to estimate black hole masses, and the monochromatic luminosity at 3000 Å to estimate L_{bol} and hence L/L_{Edd}. This quantity is also shown in Figure 2.13, along with the observed equivalent width of the He II λ1640 emission line.

As expected, we recover the correlation between L/L_{Edd} and C IV blueshift. We also find that objects with stronger Fe III emission tend to have higher L/L_{Edd} ratios, consistent with the scenario outlined above. However, not all objects with high L/L_{Edd} display strong Fe III emission, suggesting that L/L_{Edd} is not the sole driver of the Fe III equivalent width.

On the other hand, we also find that the equivalent width of UV34 anticorrelates with that of He II λ1640, which is another quantity known to show strong trends with C IV line properties. He II is believed to trace the hardness of the SED which is illuminating the BLR, i.e. the strength of the extreme ultraviolet continuum radiation which is largely unseen by the observer. The observed correlation between Fe III and C IV could thus be driven by changes in the shape of the ionising SED. However, recent work by Ferland et al. (2020) has also pointed out that changes in the equivalent width of He II are also expected due to changes in the covering factor of the He II emitting gas, which could itself be varying in response to the hardness of the unseen SED, and thus the equivalent width of He II may not enjoy a linear relationship with the relative flux of Helium-ionising photons.

2.7 SUMMARY

While Fe III has long been known to be present in AGN spectra, the recent large set of atomic data of Badnell and Ballance (2014) makes theoretical predictions of its emission spectrum possible for the first time.

Using CLOUDY predictions for the strength of the Fe III emission across a large range of parameter space, we have explored the effect of variations in the density, ionising flux and turbulence of the emitting gas. The highly-excited UV34 multiplet is predicted to be the strongest feature, and the new predictions allow this multiplet to be accurately subtracted from the 1909 Å C III] + Fe III + Si III] complex. Our main results are as follows:

- The lack of observed Fe III emission below 1000 Å shows that the Fe III lines in AGN are emitted by photoionised gas.
- Strong Fe III UV34 emission in quasar spectra demonstrates that high density ($n_H \simeq 10^{14}\,cm^{-3}$) gas is present in the majority of luminous quasars. This gas must also produce large amounts of Al III λλ1855,1863.

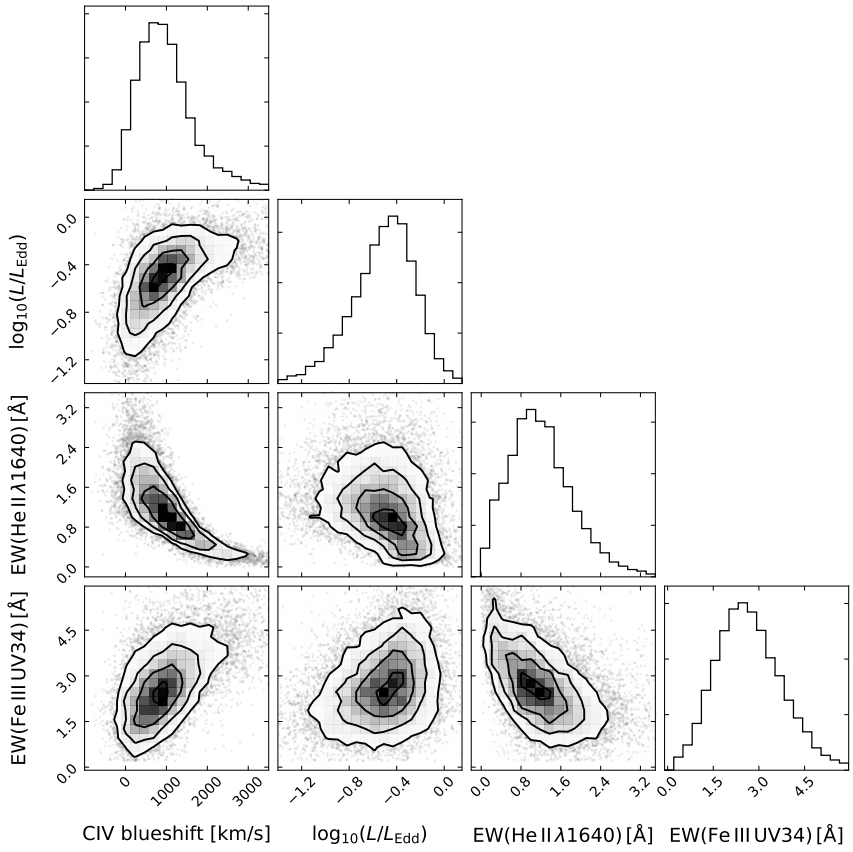

Figure 2.13: The equivalent width of Fe III UV34 emission, shown against the blueshift of the C IV emission line, the Eddington ratio, and the equivalent width of He II λ1640 emission. The strength of Fe III increases with the signature of stronger nuclear outflows, which might be driven by higher L/L_{Edd}. However, the strengths of Fe III and He II anticorrelate, suggesting that the link between Fe III and C IV could also be driven by variation in the SED which is illuminating the BLR.

- Together with the upper bounds on density from semi-forbidden lines such as C III], our results show that the BLR in AGN must have a non-uniform density structure. Our analysis suggests that the Fe III emission originates in gas about 1 dex closer to the black hole than the source of C IV emission.

- Thermal line widths cannot produce sufficiently strong Fe III emission. Non-thermal line widths must therefore be present to increase the equivalent width by continuum pumping, i.e. increasing the number of continuum photons which can excite the transition.

- Baldwin et al. (2004) found that microturbulence also improves the fit to the Fe II spectrum. Fe III is a more straightforward case since its spectrum is much simpler with isolated lines. Together, the strength of the Fe II and Fe III emission in quasar spectra make a compelling case for a turbulence in the line emitting region.

- Using the new atomic data, and our dense turbulent model, it is possible to predict the line ratios in the Fe III UV34 multiplet: $\lambda 1895.46 : \lambda 1914.06 : \lambda 1926.30 = 1.316 : 1 : 0.921$.

- Using the observed strength of the Al III doublet, the Fe III UV34 multiplet can be modelled and subtracted from the 1909 Å complex (equation 2.5). This enables a more accurate measurement of the C III] and Si III] emission, even when these lines are blended together.

3

MODELLING QUASAR COLOURS

3.1 INTRODUCTION

Over the past few decades, larger and deeper surveys of the sky have each built a more complete census of the AGN which populate our universe, from the 2dF QSO Redshift Survey (Boyle et al., 2000; Croom et al., 2001, 2004) through iterations of the Sloan Digital Sky Survey (SDSS; Pâris et al., 2017, 2018; Richards et al., 2002; Schneider et al., 2010; York et al., 2000).

Upcoming surveys such as the Vera C. Rubin Observatory's Legacy Survey of Space and Time (LSST; Ivezić et al., 2019) and ESA's Euclid mission (Euclid Collaboration et al., 2019; Laureijs et al., 2011) will probe new regimes; both pushing fainter in luminosity and also providing unprecedented amounts of data on variability in the time domain. In order to identify as many quasars as possible within these rich upcoming data-sets, we first need to understand what we expect new AGN to look like in those surveys. LSST and Euclid will probe deeper than ever before and in so doing will identify tens of millions of new AGN. These apparently fainter AGN will be located in hitherto unpopulated regions of parameter space: both bright objects at higher redshifts and intrinsically fainter objects at lower redshifts, whether that be due to smaller black holes or lower accretion rates, and where the contribution from starlight in the host galaxy to the total observed flux will be more significant.

Since the intra-population variation in the structure of SMBH accretion discs is not fully understood in a quantitative sense, the majority of quasar SED templates are purely empirical. Two popular models are the template SED of Elvis et al. (1994) and the composite spectrum of Vanden Berk et al. (2001). However, models such as these are generally derived from samples with a large range in luminosity as a function of rest frame wavelength, which means that different parts of the template are appropriate for different regions of luminosity-redshift space. This motivates the need for a parametric model, where different parameters are able to be adjusted in a way which is well-motivated by known astrophysics, especially when providing predictions for luminosities and redshifts which are different from those used to define the model.

In this chapter we construct a parametric model for the rest frame 912 Å to 3 μm region of the quasar SED, which corresponds to the observed frame optical and near-infrared colours. By cross-matching the SDSS quasar catalogue to UKIDSS-LAS and unWISE, we obtain a large

sample of quasars with photometric data covering the *ugrizYJHKW12* bands. The parameters of this model are fit to the median SDSS-UKIDSS-WISE colours in redshift bins spanning $0.1 < z < 3.5$. We then explore how the parameters change as a function of apparent magnitude, before extrapolating these observed changes to make predictions for the colours of new quasars which will be discovered using LSST and Euclid.

3.2 DATA

3.2.1 *Optical data*

All the quasars used in this chapter are drawn from the SDSS fourteenth data release (DR14) quasar catalogue, the selection of which is summarised in Pâris et al. (2018). There are a total of 526 356 quasars in this catalogue, spanning the redshift range $0 < z < 5$. We use *ugriz* point spread function magnitudes from the SDSS quasar catalogue.

SDSS catalogue magnitudes are reported on the 'asinh' system. Assuming that all sources are well-detected, so the asinh magnitude is well-approximated by the Pogson magnitude, SDSS zeropoints are converted to the AB standard using

$$\begin{aligned} u_{AB} &= u_{SDSS} - 0.04 \\ z_{AB} &= z_{SDSS} + 0.02 \end{aligned} \tag{3.1}$$

The SDSS *g*, *r*, and *i* magnitudes are believed to be on the AB system,[1] and we take care to exclude bands with low flux (i. e. 'drop-outs') as we move to higher redshifts.

AB magnitudes are converted to the Vega system using

$$\begin{aligned} u_{Vega} &= u_{AB} - 0.913 \\ g_{Vega} &= g_{AB} + 0.081 \\ r_{Vega} &= r_{AB} - 0.169 \\ i_{Vega} &= i_{AB} - 0.383 \\ z_{Vega} &= z_{AB} - 0.542 \end{aligned} \tag{3.2}$$

For consistency between surveys, we report all observed SDSS, UKIDSS and WISE colours on the Vega system. Predicted LSST and Euclid colours are reported on the AB system, which will be the native magnitude system for those surveys.

3.2.2 *Infrared data*

We cross-match the SDSS DR14 quasar catalogue to the tenth data release of the UKIDSS Large Area Survey (UKIDSS-LAS DR10; Lawrence

1 https://www.sdss.org/dr16/algorithms/fluxcal#SDSStoAB

et al., 2007). We use 'apermag3' values, which are the default point source 2.0 arcsec diameter aperture corrected magnitudes. The SDSS footprint covers 14 555 square degrees of the northern sky. UKIDSS-LAS covers a subset of size 4000 square degrees, i.e. slightly less than three tenths of the SDSS footprint, in the near-infrared *YJHK* bands. We match 116 370 quasars from SDSS DR14 to unique sources within 1.0 arcsec in the UKIDSS-LAS DR10 catalogue. The number of detections is slightly larger than given by Pâris et al. (2018), who use a force-photometry method, and we believe the improvement is due to our use of more recent data from UKIDSS.

We cross-match the SDSS DR14 quasar catalogue to the deepest source of mid-infrared WISE (Wright et al., 2010) data which is currently available: the unWISE catalogue presented by Schlafly, Meisner and Green (2019), which makes use of the Meisner et al. (2019) coadds. WISE is an all-sky survey and so covers the entire SDSS footprint. unWISE incorporates additional data from the reactivation of the satellite as NEOWISE, giving ≈0.7 magnitudes deeper coverage in *W1* and *W2* compared to AllWISE. The unWISE catalogue is matched to SDSS using a 3.0 arcsec matching radius, keeping only sources with unique matches within that radius. unWISE models the *W1* and *W2* pixel data separately, and to reduce the number of contaminants we keep only sources where there is a detection in both *W1* and *W2*. We find 452 315 unWISE sources match to quasars from SDSS DR14. 452 199 of these matches have S/N greater than 5 in both *W1* and *W2*. This number of unWISE matches is significantly higher than the number of matches to AllWISE found by Pâris et al. (2018), reflecting the increased depth of the Schlafly, Meisner and Green (2019) catalogue.

3.2.3 *Galactic extinction*

We correct the *ugrizYJHK* photometric bands for Galactic extinction using the improved dust maps of Schlafly et al. (2010) and Schlafly and Finkbeiner (2011). Such extinctions are typically of the order $E(B-V) < 0.1$, as most quasars in the SDSS footprint lie outside the Galactic plane.

Commonly quoted passband attenuations are correct only for sources with SEDs similar to that of an elliptical galaxy at low redshift, and we derive our own passband attenuations using a $z = 2.0$ quasar source SED, assuming $R_V = 3.1$ and the Galactic extinction curve of Fitzpatrick and Massa (2009). A type 1 quasar SED is bluer than a typical stellar or galaxy SED, leading to subtle differences in the conversion from $E(B-V)$ to the attenuation in each observed passband. The conversions we use are given in Table 3.1. Using source quasar SEDs in the range $1.5 \leqslant z \leqslant 2.5$ alters these values by no more than 1.5 per cent. The attenuation due to dust in the WISE bands is found

Filter	$A_\lambda/E(B-V)$
SDSS u	4.82
SDSS g	3.80
SDSS r	2.58
SDSS i	1.92
SDSS z	1.42
UKIDSS Y	1.12
UKIDSS J	0.80
UKIDSS H	0.52
UKIDSS K	0.33

Table 3.1: Passband attenuations $A_\lambda/E(B-V)$ for *ugrizYJHK* filters adopting the $R_V = 3.1$ Galactic reddening law from Fitzpatrick and Massa (2009) and a $z = 2.0$ quasar SED.

to be negligible for the extinctions we consider and no correction for Galactic extinction is applied to these data.

3.3 PARAMETRIC MODEL SED

In this section we describe the construction of a parametric SED model to describe quasar emission in the 912 Å to 3 μm rest frame wavelength range. The model parameters are then optimised using a Markov Chain Monte Carlo (MCMC) sampler to fit the median observed colours of the SDSS quasar population at $i_{AB} < 19.1$. The quasar SED model builds on the model used by Hewett et al. (2006), Maddox et al. (2008) and Maddox et al. (2012), and three example SEDs are shown in Fig. 3.1.

3.3.1 *Ultraviolet–optical continuum*

The 900 Å to 1 μm region of the quasar SED is dominated by a blue continuum, corresponding to the low-frequency tail of the thermal emission from the accretion disc. We characterise this continuum using a broken power-law, with both the slopes and position of the break able to vary.

$$f_\lambda = \begin{cases} k_1 \lambda^{\alpha_1} & \lambda < \lambda_{\rm break} \\ k_2 \lambda^{\alpha_2} & \lambda > \lambda_{\rm break} \end{cases} \qquad (3.3)$$
$$f_{\lambda_{\rm break}} = k_1 \lambda_{\rm break}^{\alpha_1} = k_2 \lambda_{\rm break}^{\alpha_2}$$

At wavelengths $\lambda \leqslant 1200$ Å, the power-law slope is modified to become $\alpha_3 = \alpha_1 - 1$ to account for the sharp change in the continuum observed in quasar spectra (Green et al., 1980).

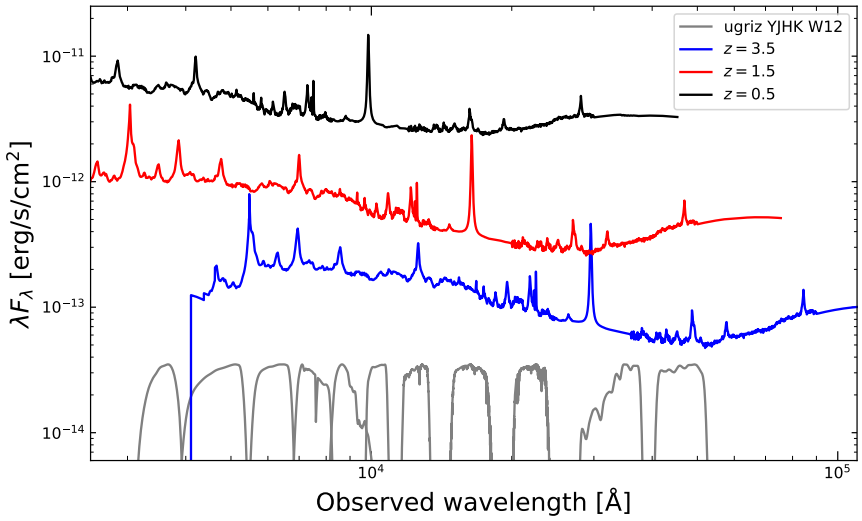

Figure 3.1: Examples of the model SED in the observed frame. SDSS *ugriz*, UKIDSS *YJHK* and WISE *W12* filter response curves are shown for comparison.

3.3.2 *Hot dust*

Near-infrared emission at wavelengths $1 < \lambda < 3\,\mu\mathrm{m}$ is dominated by emission from hot dust, which we characterise using a single blackbody. The temperature, T_{BB}, and normalisation relative to the power-law continuum at $2\,\mu\mathrm{m}$, `bbnorm`, of this blackbody are free to vary.

$$f_\lambda = \texttt{bbnorm} \times B_\lambda(T_{BB}) \times \left(\frac{k_2 \lambda^{\alpha_2}}{B_\lambda(T_{BB})} \right)_{\lambda = 2\mu\mathrm{m}} \tag{3.4}$$

where $B_\lambda(T)$ is the Planck function:

$$B_\lambda(T) = \frac{2hc^2}{\lambda^5} \frac{1}{e^{hc/\lambda k_B T} - 1} \tag{3.5}$$

3.3.3 *Balmer continuum*

We use the prescription from Grandi (1982) to describe the broad ~3000 Å 'bump' due to blended emission from Fe II, high-order Balmer lines, optically thin Balmer continuum, and two-photon emission from neutral Hydrogen:

$$\begin{aligned} f_\lambda &= f_0 \times B_\lambda(T_{BC})(1 - e^{-\tau_\lambda}); \quad \lambda < \lambda_{BE} \\ \tau_\lambda &= \left(\frac{\lambda}{\lambda_{BE}} \right)^3 \\ f_0 &= \texttt{bcnorm} \times \left(\frac{k_2 \lambda^{\alpha_2}}{B_\lambda(T_{BC})(1 - e^{-\tau_\lambda})} \right)_{\lambda = 3000\text{Å}} \end{aligned} \tag{3.6}$$

where $T_{BC} = 13150\,\mathrm{K}$ is the electron temperature of the Balmer continuum, $\lambda_{BE} = 3646\,\text{Å}$ is the wavelength of the Balmer edge, and τ_λ is the optical depth of the Balmer continuum, fixed such that the continuum is optically thick at the edge, i. e. $\tau_{\lambda_{BE}} = 1$. This function is then broadened via convolution with a Gaussian, with a FWHM of $5000\,\mathrm{km\,s^{-1}}$, to imitate the kinematics of the Balmer-emitting gas in broad line AGN. The normalisation relative to the power-law continuum at 3000 Å, `bcnorm`, is the only parameter free to vary.

3.3.4 *Emission lines*

Emission lines are included using the templates of Francis et al. (1991) and Glikman, Helfand and White (2006) for the ultraviolet–optical and near-infrared regions of the spectrum respectively. These templates overlap around the Hα emission line, which is replaced with a single Gaussian centered at 6565 Å. The equivalent width of each line in the template is preserved as the continuum changes, subject to four scaling factors: `scal_em` re-scales the combined emission line template, `scal_ha` and `scal_glik` re-scale the Hα and near-infrared regions respectively to account for any differences in the continuum subtraction prior to combining the templates. Finally, `scal_lya` re-scales the emission line template at wavelengths shorter than 1350 Å to account for the fact that the objects contributing to the Francis et al. (1991) template at short wavelengths are much fainter than those contributing at longer wavelengths. We found that preserving the emission line equivalent widths resulted in a better representation of the colours, but the code also has the ability to instead preserve the relative emission line fluxes.

It has been proposed by Baldwin (1977) that the equivalent width of strong emission lines in quasar spectra is (anti-)correlated with the intrinsic luminosity of the source. However, this correlation has also been ascribed as spurious and due to selection effects, with contradictory results in the literature for different samples (see section 3.1 of Sulentic, Marziani and Dultzin-Hacyan, 2000, for a review).

For our model, the emission line for which a Baldwin effect would have the most significant impact on the resulting colours is Hα. We have experimented with including a scaling factor for Hα which adjusts the strength of this line as a power-law function of luminosity, but fitting for the slope of this power-law lead to a posterior which was consistent with zero slope, i. e. no significant evolution in the average strength of Hα across the redshift range of our bright $i < 19.1$ sample. We therefore fix the equivalent width of the emission lines to be constant as a function of redshift within our model SED.

3.3.5 *Host galaxy flux*

We have the ability to include a component to account for stellar emission from the host galaxy. For the luminous quasars we consider, the primary effect of starlight from the host galaxy is to add flux to the 1 μm minimum in the total quasar SED. For optically unobscured, blue quasars such as those from SDSS, the strength of emission from any young stellar population is very hard to quantify as the quasar power-law continuum will be much brighter than the host galaxy at shorter wavelengths. It is therefore hard to quantify any change in shape of the host galaxy SED across the luminosity and redshift range we consider. We use an Sb template from the SWIRE library (Polletta et al., 2007; Rowan-Robinson et al., 2008), having found that this choice of template produces a small but significant improvement in the goodness-of-fit of the best fitting model. This is perhaps to be expected as an Sb is in some sense an 'average' galaxy SED which contributes flux from both young and old stellar populations.

There undoubtedly exist quasars in SDSS which reside in strong starbursts and also quasars which lie within passive elliptical galaxies, but these objects will always be found at the extremes of the colour distribution; the *median* quasar colours are most likely to be well-accounted for with the inclusion of a spiral galaxy SED. Probing fainter in flux is likely to reveal an amount of diversity in the galaxy types of quasar hosts, but such considerations are beyond the scope of this work. Here we do not set out to infer anything about the host galaxy properties of quasars in either SDSS or LSST, but simply aim to describe what we might expect the average colours of quasars which are similar to the SDSS population to look like in LSST and Euclid.

The strength of host galaxy emission is incorporated into the model with two parameters: `fragal`, the fraction of total flux in the wavelength region 4000-5000 Å due to the galaxy for an object at a reference luminosity L_0, and `gplind`, the power-law index controlling how the luminosity of the galaxy component changes as a function of the quasar luminosity:

$$\frac{L_{\text{galaxy}}}{L_0} = \frac{\texttt{fragal}}{1 - \texttt{fragal}} \left(\frac{L_{\text{quasar}}}{L_0} \right)^{\texttt{gplind}} \tag{3.7}$$

`gplind` is assumed to lie between 0 and 1, meaning that as one moves to higher redshifts within a flux-limited sample, the host galaxy component gets brighter as the quasar gets brighter, but the fractional contribution of the galaxy to the total flux decreases.

The luminosities used are the absolute *i*-band magnitudes at redshift 2, derived using the *K*-correction from Richards et al. (2006) and as reported in the Pâris et al. (2018) catalogue. For each flux cut that is used, the median M_i is calculated in each redshift bin, giving an empirical redshift-luminosity relation for each sample which is then

assumed when calculating the galaxy normalisation at any given redshift (see Fig. 3.7). The reference luminosity L_0 is taken to be $M_i = -22.6$, corresponding to the average luminosity of the $i_{AB} < 19.1$ sample at $z = 0.2$.

3.3.6 *Dust reddening*

This extinction curve was derived by P. Hewett.

We characterise the attenuation due to dust at the redshift of the quasar using an empirically derived extinction curve. The curve is very similar to that presented by Gallerani et al. (2010): while it rises more steeply with decreasing wavelength than the Milky Way curve, it is significantly less steep than the extinction curve found from the Small Magellanic Cloud, and contains no 2200 Å feature.

The quasar flux, excluding the host galaxy component, can be reddened using this quasar extinction curve with the $E(B-V)$ as a free parameter. The colour distribution of SDSS quasars is largely Guassian, with only a small tail due to reddening (Hopkins et al., 2004; Richards et al., 2003); the median colour in any redshift bin is assumed to be not significantly affected by extinction. The $E(B-V)$ is therefore held fixed at zero when fitting for the other model parameters.

3.3.7 *Lyman suppression*

At redshifts $z > 1.4$, flux at $\lambda < 1216$ Å is suppressed using the prescription of Faucher-Giguère et al. (2008) to account for the incomplete transmission through the intergalactic medium of flux shortwards of Lyα, Lyβ and Lyγ.

Finally, the SED is redshifted into the observed frame and multiplied by the passband filter responses to obtain synthetic photometry.

3.4 BRIGHT QUASAR SAMPLE

3.4.1 *Sample definition*

The original SDSS quasar selection is known to recover more than 90 per cent of known and simulated quasars at the majority of redshifts, up to a magnitude limit of $i_{AB} = 19.1$ (Richards et al., 2002). Subsequent iterations of SDSS have added more quasars at fainter luminosities, but have targeted specific sub-populations for the purposes of e. g. Baryonic Acoustic Oscillation experiments, which are possibly biased in their colour selection.

The aim of this chapter is to model the SED of quasars across the 912 Å to 3 µm rest frame wavelength range, so we require infrared photometry for the objects in our sample. Restricting the SDSS DR14 catalogue to $i_{AB} < 19.1$ produces a sample which is 98, 96, 98 and 99

per cent complete in UKIDSS Y, J, H, and K respectively, and 98 per cent complete in unWISE.

84 267 quasars from SDSS DR14 have $i_{AB} < 19.1$, and 26 274 of these match to UKIDSS-LAS and unWISE. The number of objects at very high and very low redshift is very low and the redshift range is restricted to $0.1 < z < 3.5$. There are 26 001 objects in this sample, which are divided into 321 redshift bins with precisely 81 objects in each bin.

3.4.2 *Fitting routine*

Let C be the set of ten intra-band SDSS, UKIDSS-LAS, and unWISE colours

$$C = \{u - g, g - r, ..., K - W1, W1 - W2\} \tag{3.8}$$

For every quasar in the sample, each colour c in C is computed. The sample is then divided into a set of redshift bins Z which are spaced so as to have a uniform number of objects in each bin. The medians of each colour M_c are computed in each bin, along with the median absolute deviation (MAD), which is a measure of the spread of observed colours within that redshift bin.

for a Gaussian distribution with standard deviation σ, the median absolute deviation is given by $MAD \approx 0.6745\sigma$

$$\mathrm{MAD}(\{x_i\}) = \mathrm{median}(\{|x_i - \mathrm{median}(\{x_i\})|\}) \tag{3.9}$$

For any given set of SED model parameters, the SED model can then be evaluated at every median redshift z in Z, giving a set of synthetic colours $S_{c,z}$.

The loglikelihood is then defined as

$$\ell = -\frac{1}{2} \sum_{c,z \in C,Z} \left(\frac{(M_{c,z} - S_{c,z})^2}{\mathrm{MAD}^2_{c,z}} + \log(\mathrm{MAD}^2_{c,z}) \right) \tag{3.10}$$

Using flat priors on all parameters, samples are drawn from the posterior distribution using an affine-invariant ensemble MCMC method (Goodman and Weare, 2010), as implemented by the python package `emcee` (Foreman-Mackey et al., 2013). The advantage of using an affine-invariant sampler over a traditional Metropolis-Hastings (MH) algorithm is that it has a higher acceptance fraction, therefore requiring fewer calls of the likelihood function to produce the same number of independent posterior samples. As an ensemble method, the algorithm can also be parallelised without violating the detailed balance equations, reducing both the time and total computational resource required compared to the MH algorithm.

3.4.3 *Results*

We fit our model to the median observed *ugrizYJHKW12* colours in our $0.1 < z < 3.5$, $i_{AB} < 19.1$ quasar sample, letting all twelve parameters

Description	Parameter	Value	σ
blue power-law slope	α_1	-0.446	0.013
red power-law slope	α_2	-0.137	0.018
power-law break wavelength	λ_{break}	2700 Å	40 Å
blackbody normalisation	`bbnorm`	2.91	0.05
blackbody temperature	T_{BB}	1270 K	8 K
Balmer continuum normalisation	`bcnorm`	0.017	0.002
overall emission line scaling	`scal_em`	1.047	0.024
Hα emission line scaling	`scal_ha`	1.003	0.024
Lyα emission line scaling	`scal_lya`	0.686	0.027
near-infrared emission line scaling	`scal_glik`	0.950	0.071
galaxy fraction at $M_i = -22.6$	`fragal`	0.251	0.013
galaxy luminosity power-law index	`gplind`	0.177	0.072

Table 3.2: Best-fitting model parameters for the sample of $i_{AB} < 19.1$ quasars. σ is the Gaussian standard deviation for each parameter.

		r
α_2	`gplind`	0.735
`scal_em`	`scal_ha`	0.649
`fragal`	`gplind`	-0.619
`bbnorm`	`gplind`	0.618
α_2	`bbnorm`	0.593
α_2	`scal_ha`	0.538
α_2	λ_{break}	0.531

Table 3.3: Correlation coefficients for all seven parameter pairs with $|r| > 0.5$

vary. The results are shown in Fig. 3.2, and the maximum likelihood values are given in Table 3.2. The correlation coefficients for the most correlated parameter pairs are given in Table 3.3. Degeneracies are to be expected between certain parameter pairs, for example `scal_em` and `scal_ha`, as they both control the strength of the Hα emission line. Slight degeneracies are also seen between the strength of evolution of the galaxy contribution `gplind`, the strength of hot dust emission `bbnorm` and the second power-law slope α_2. These degeneracies are due to the normalisation of the hot dust blackbody and galaxy contribution relative to the power-law continuum at 2 μm and 4000-5000 Å respectively, which are both in the region governed by α_2.

In Fig. 3.3, we show the median observed colours for this sample, together with the predicted colours from our best-fitting model. The model is seen to be very good at reproducing the average quasar properties across most of the colour-redshift space, although the median

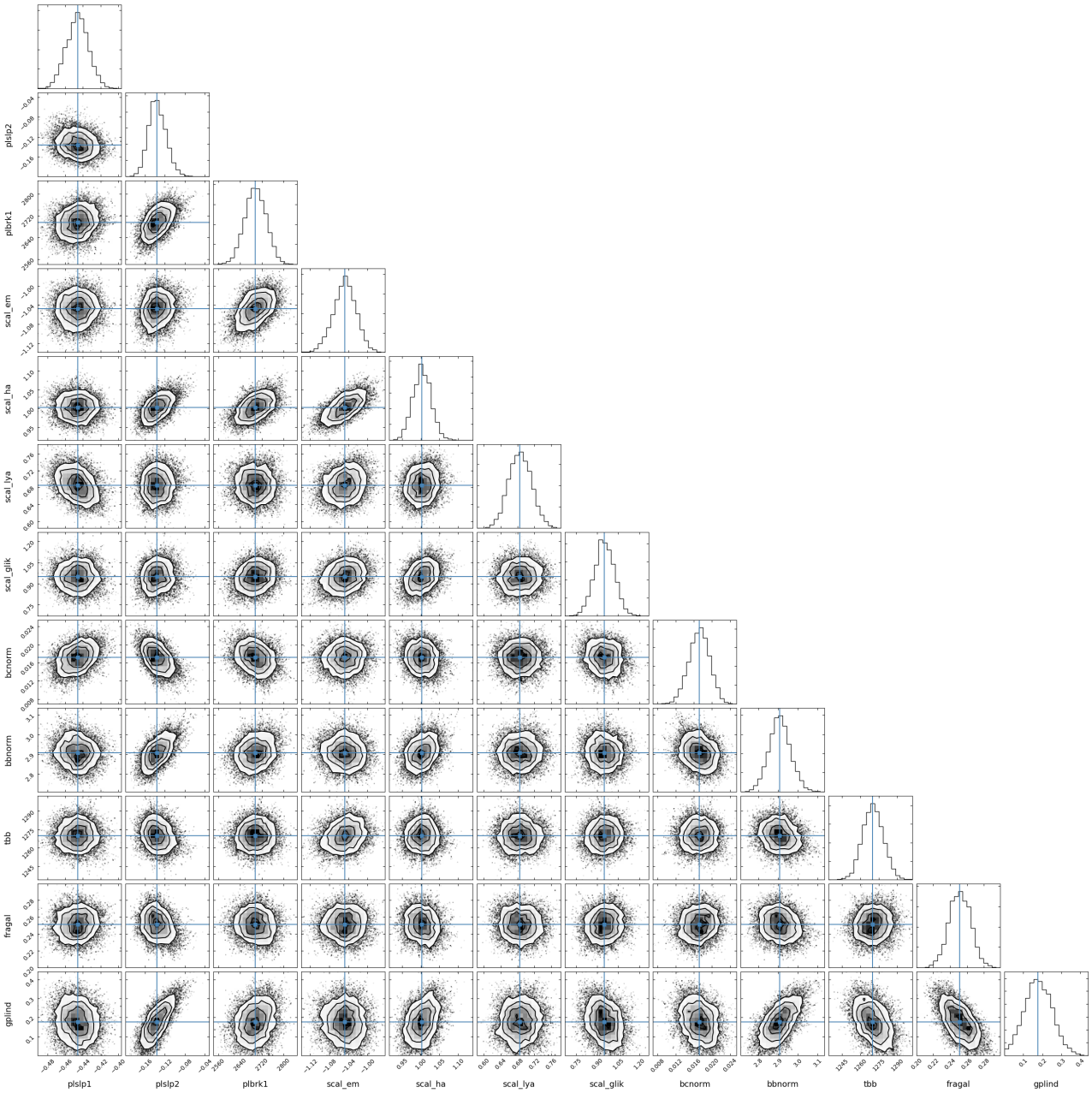

Figure 3.2: Samples from the posterior distribution of the likelihood surface of SED model parameters defined in equation 3.10, fitting to the sample of $i < 19.1$ quasars. The posterior is seen to be unimodal in all projections. Some slight degeneracies can be observed between the strength of evolution of the galaxy contribution `gplind`, the strength of hot dust emission `bbnorm` and the second power-law slope α_2, but otherwise all parameters are well-determined. The maximum-likelihood solution is shown in blue.

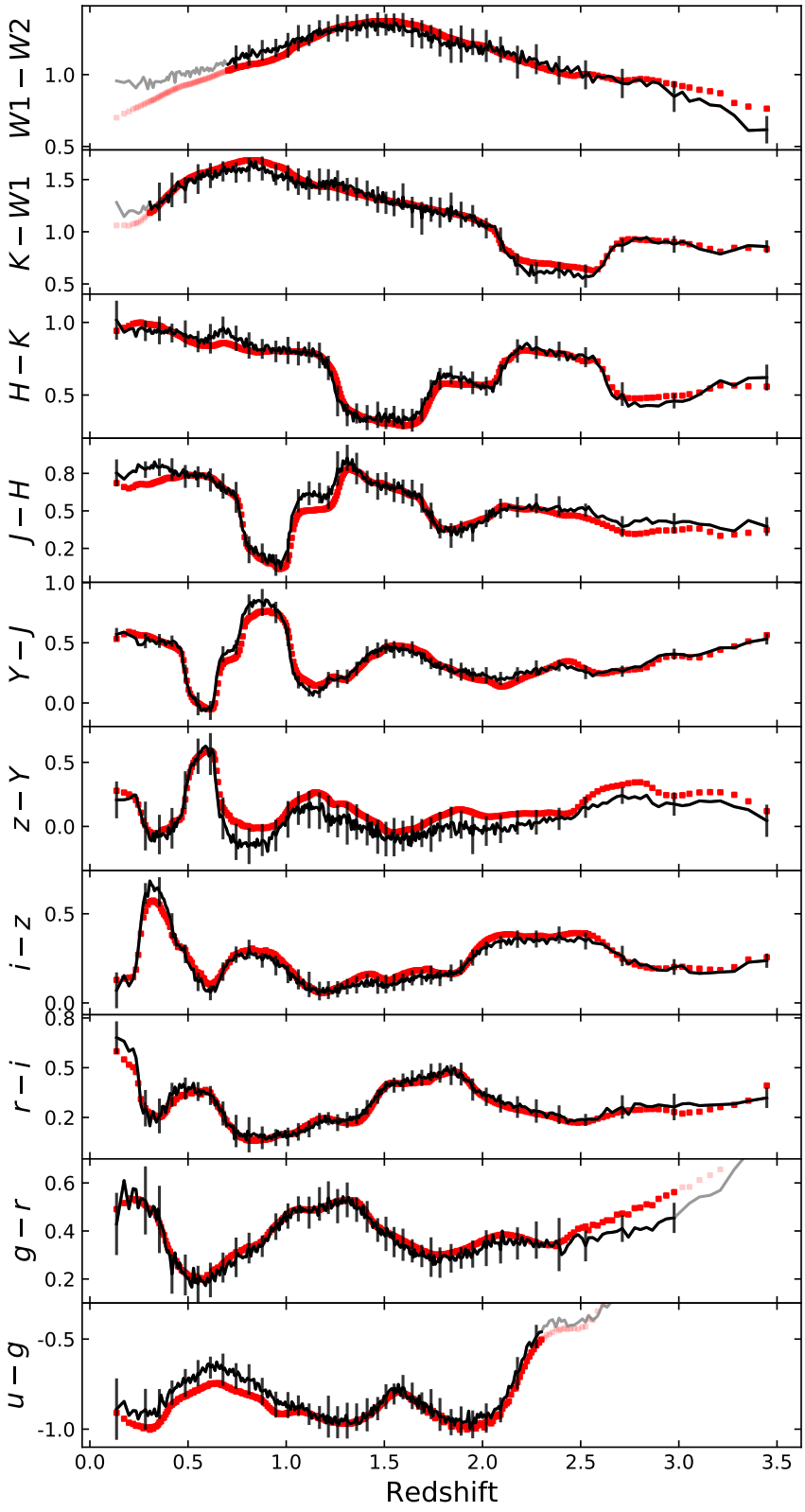

Figure 3.3: Black: median observed SDSS-UKIDSS-unWISE Vega colours in each redshift bin for our sample of $i_{AB} < 19.1$ quasars. Error bars show the median absolute deviation within every eighth bin. Red: the best-fitting model. Rest wavelengths $\lambda < 912\,\text{Å}$ or $\lambda > 3\,\mu\text{m}$ where the model is not fit to the data are grayed out.

$u-g$ colour at the lowest redshifts is observed to be ~0.1 magnitudes redder than modelled. This is unlikely to be due to systematic changes in the average ultraviolet continuum slope, as the lowest redshift objects are those with the smallest black hole masses, which would normally be expected to display the bluest continua. It could instead be that the form of the host galaxy template is not optimal, and that the average host galaxy SED of low-redshift quasars has a different shape, potentially due to a different balance between young and old stellar populations. The $u-g$ offset could also be explained by the fact that the low-redshift objects are much less luminous and so are expected to show stronger emission lines.

We have successfully constructed a model which reproduces the median SDSS-UKIDSS-WISE colours of a reasonably complete sample of quasars at $i_{AB} < 19.1$. However, future surveys such as LSST will probe significantly fainter than this flux limit, so we now need to identify how the average quasar colours might be expected to change as a function of apparent magnitude.

3.5 CHANGES IN QUASAR COLOURS WITH APPARENT MAGNITUDE

3.5.1 *Observed trends*

The completeness of SDSS quasars within the UKIDSS-LAS drops significantly above $i_{AB} = 19.1$. unWISE, on the other hand, remains 95 per cent complete up to a limit of $i_{AB} < 20.6$. At $i_{AB} > 20.6$, significant numbers of SDSS quasars become fainter than $z_{AB} = 20.3$, where their asinh magnitudes and logarithmic Pogson magnitudes begin to differ by more than one per cent in flux. In Fig. 3.4 we therefore show the median SDSS-unWISE colours in four bins of *i*-band magnitude up to $i_{AB} = 20.6$.

The largest change in the quasar colours at fainter luminosities is expected to be due to a changing fraction of host galaxy flux contribution. This is expected to be most significant around the 1 μm minimum in the quasar SED, where the optical continuum is dying off but the hot dust emission has yet to start rising. At redshifts $1 < z < 2$, this minimum is moving through the unWISE *W1* passband, and as expected, moving to fainter *i*-band magnitudes we can see that there are noticeable changes in the *zW1W2* colours. In the rest frame optical, the flux due to starlight is generally going to be redder than the quasar continuum, so a larger host galaxy contribution has the effect of reddening the *griz* colours at lower redshifts $z < 1$. Finally, the equivalent width of the ultraviolet emission lines is expected to increase as the luminosity of the quasars decreases, the so-called Baldwin effect, leading to slightly larger-amplitude wiggles in the *griz* colour-redshift tracks at higher redshifts $z > 1$.

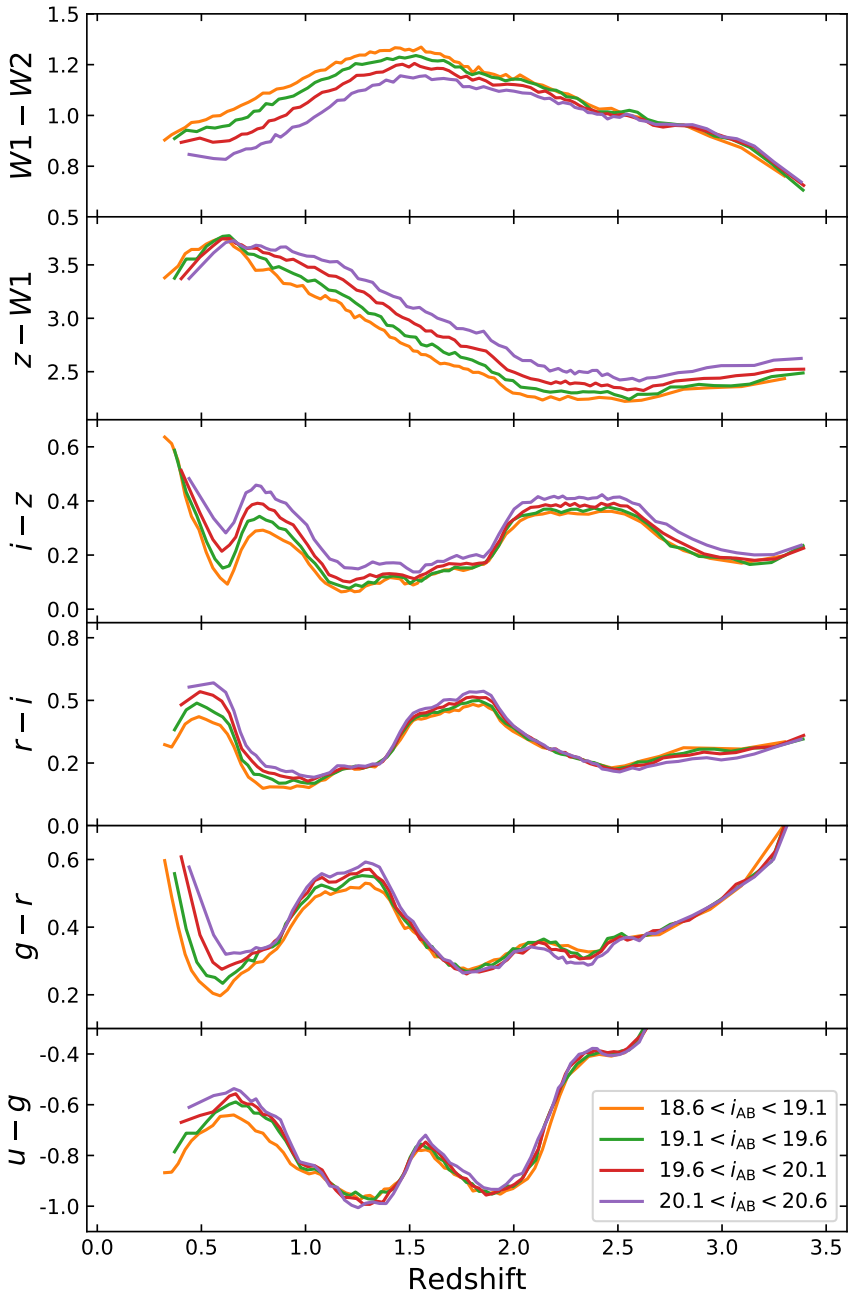

Figure 3.4: Median observed SDSS-unWISE Vega colours as a function of redshift. Each colour-redshift track represents a different apparent *i*-band magnitude: as we move to fainter luminosities we expect starlight from the host galaxy to have a greater contribution to the total quasar SED.

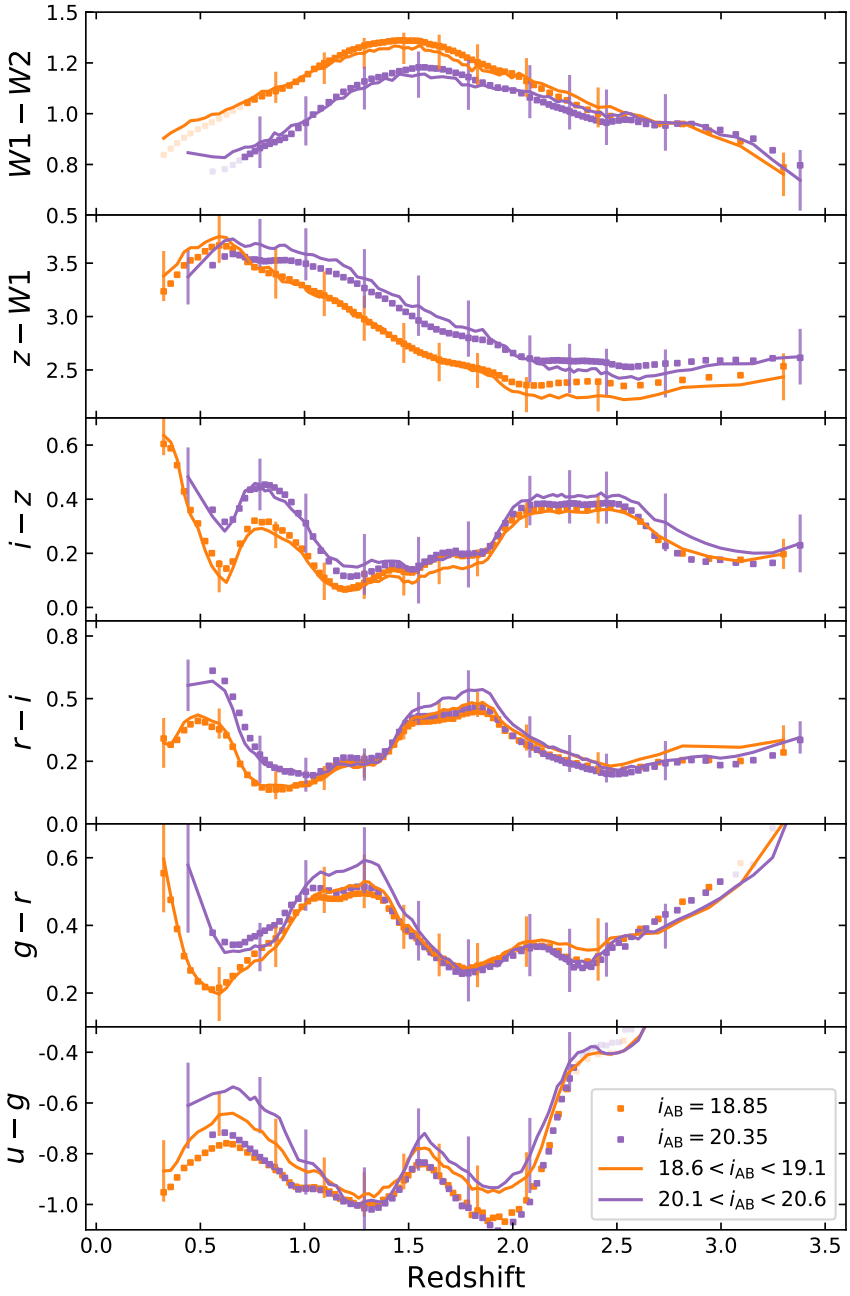

Figure 3.5: Fitting for the host galaxy parameters and emission-line scaling in fainter-magnitude samples. Solid lines show the median observed Vega colours as in Fig. 3.4. Error bars show the median absolute deviation in every eighth bin. Squares show the best-fitting quasar model: the variation in *W1* and *W2* is well accounted for by the host galaxy, as are the low-redshift changes in *griz*.

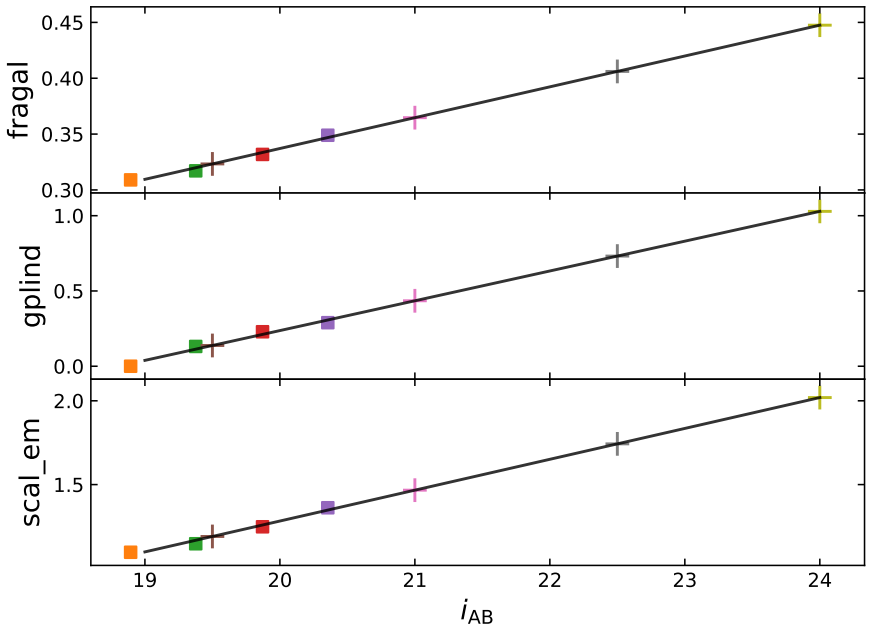

Figure 3.6: Squares: best-fitting model parameters to observed data in four flux bins. Black lines: linear extrapolation of the parameters to LSST-like depths (Eq. 3.11), with the values used in Figs. 3.8-3.10 marked with crosses.

To account for these observed changes in the median colours, we fit our model to the *ugrizW12* colours for each sample shown in Fig. 3.4, allowing only the galaxy parameters `gplind` and `fragal` and the emission line scaling `scal_em` to vary, and holding all other parameters fixed at their maximum likelihood values. The results are shown for the two most extreme *i*-band bins in Fig. 3.5: as expected, the variable host galaxy does a good job of accounting for the changes in *W1* and *W2*, and the changes in *griz* at low redshift, while the emission-line scaling accounts for the changes in *griz* at higher redshift. As before, the $u-g$ colour at $z < 1$ is not perfectly fit, which is an indication that we are not fully accounting for the changes in the observed total SED of lower-luminosity objects - recall from Fig. 1.2 that the faintest objects at $z < 0.5$ in SDSS have luminosities $L < 10^{44}\,\mathrm{erg\,s^{-1}}$, which is ~100 times fainter than the typical SDSS quasar at $z > 2$. Indeed, the observed excess can be explained if the lower-redshift quasar population has, on average, stronger line emission in the rest frame ultraviolet, as expected from the Baldwin effect.

For each *i*-band magnitude bin, we now have a set of best-fitting model parameters describing the host galaxy contribution and the emission line normalisation. These are shown as squares in Fig. 3.6, colour-coded to match their respective samples in Fig. 3.4. All three parameters are observed to display a direct linear correlation with i_{AB},

so we fit a straight line to these points which can then extrapolate to fainter magnitudes:

$$\begin{aligned} \texttt{fragal} &= 0.5521 \left(\frac{i_{AB}}{20}\right) - 0.2150 \\ \texttt{gplind} &= 3.960 \left(\frac{i_{AB}}{20}\right) - 3.723 \\ \texttt{scal\_em} &= 3.684 \left(\frac{i_{AB}}{20}\right) - 2.402 \end{aligned} \tag{3.11}$$

3.5.2 *Extrapolation to fainter flux limits*

In order to compute model colours at fainter flux limits, such as those expected to be reached by LSST, it is first necessary to predict the redshift-luminosity relation used to compute the galaxy normalisation (Eq. 3.7). In Fig. 3.7, we show the observed median M_i as a function of redshift for each *i*-band limited sample. These are found to be approximated by a function of the form

$$M_i = -\left[1.907\left(\frac{i_{AB}}{20}\right) + 3.411\right]\log_{10}(z) - \left[18.33\left(\frac{20}{i_{AB}}\right) + 5.841\right] \tag{3.12}$$

The faintest object from SDSS which we have considered in deriving these relations is at approximately $M_i = -22.0$, and we chose not to extrapolate our model any fainter than this luminosity. In effect this limits our model to redshifts $z > 1.5$ for $i_{AB} = 24.0$ and to redshifts $z > 1.0$ for $i_{AB} = 22.5$. However, we note that we have already seen some evidence in the $u - g$ colours which suggests that our model predictions will break down before we reach this luminosity limit. The point at which the trajectory of the trends we see in the SDSS quasar colours alters, and our model predictions will break down, is unknown, and an interesting question which one could address with LSST and Euclid data. From that point of view it is important not to take our predicted model parameters as inferring anything about the physics of fainter AGN, but instead merely providing testable predictions for how quasar selection techniques may need to adapt to identify objects in new regimes of luminosity-redshift space.

Combining our predicted $z - M_i$ tracks with the extrapolated model parameters from Eq. 3.11, we make predictions for the average colours of quasars in LSST and Euclid down to $i_{AB} = 24$, which is the single-epoch limiting magnitude for LSST. These are shown in Fig. 3.8, and the model SEDs from which they have been derived in Fig. 3.9. The evolution of the galaxy contribution to the median colours is shown in Fig. 3.10 for both observed samples and predicted models. The strong evolution of the fractional galaxy contribution with apparent

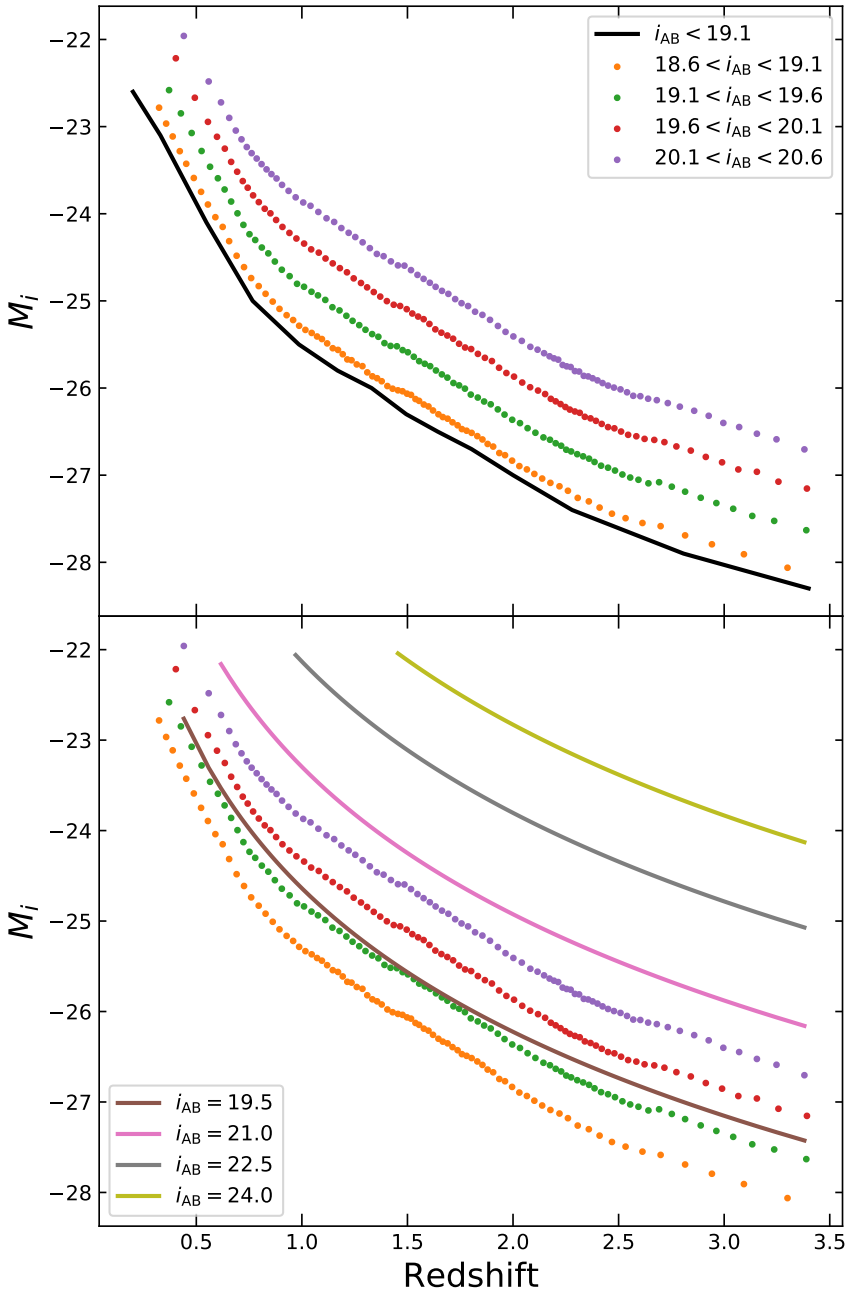

Figure 3.7: Top panel, black line: the median absolute *i*-band magnitude as a function of redshift for the sample of 26,001 quasars from SDSS DR14, UKIDSS-LAS and unWISE with $i_{AB} < 19.1$ (Fig. 3.3). Coloured points: the median M_i in each redshift bin for each *i*-band apparent magnitude sample presented in Fig. 3.4. Bottom panel, solid lines: predicted luminosity-redshift relations (Eq. 3.12) assumed when predicting colours for different flux-limited samples at LSST depths (Fig. 3.8). We limit our predictions to redshifts and apparent magnitudes where M_i is predicted to be less than −22.0, which has the effect of limiting our predictions at the faintest flux limits to higher redshifts.

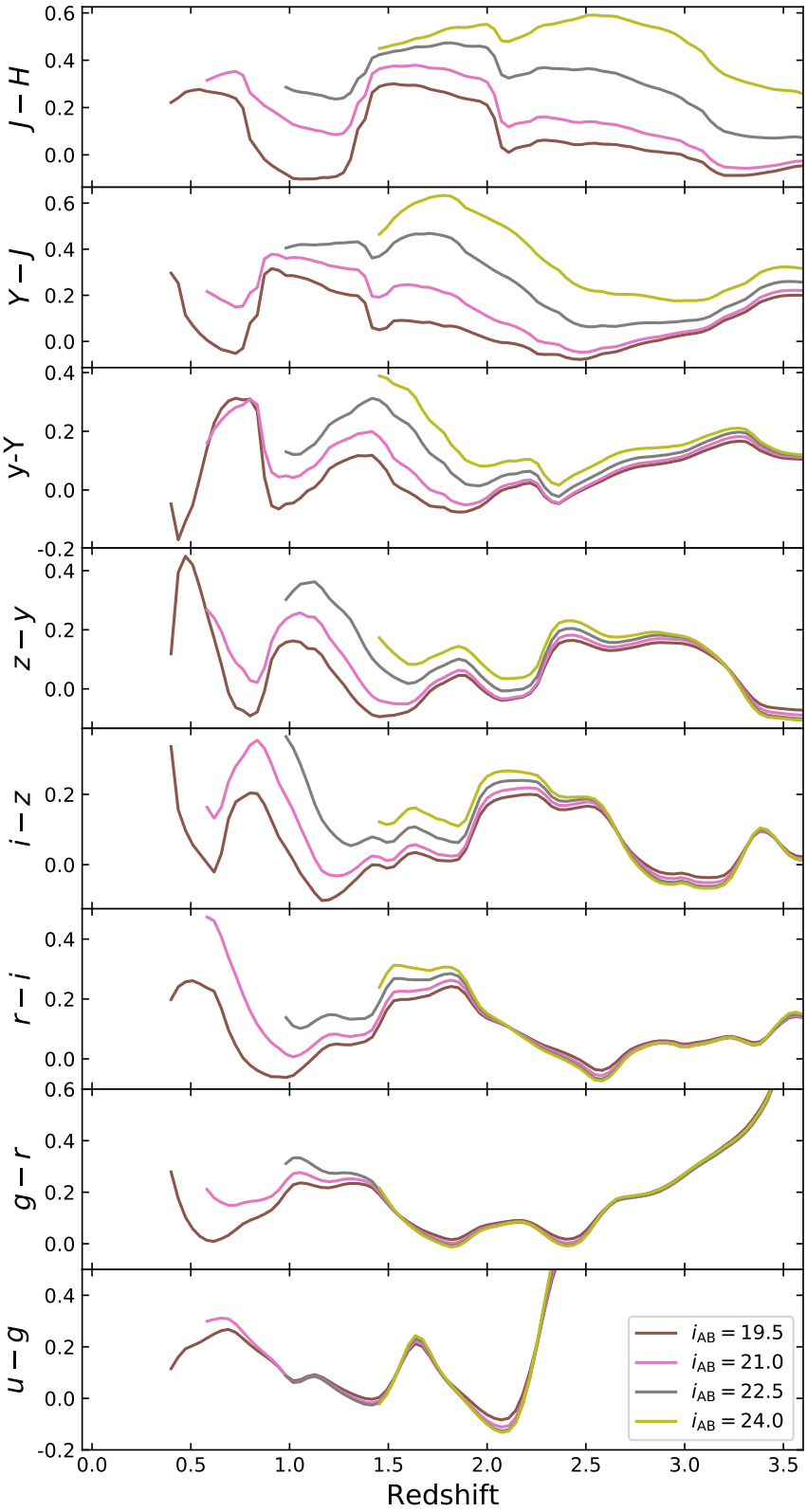

Figure 3.8: Predicted average colours as a function of redshift for LSST *ugrizy* and Euclid *YJH*. Colours are presented on the AB system, and shown for different apparent magnitudes. The host galaxy contribution is predicted to have a significant effect on the *YJH* colours, even at $z > 2$, as we move towards the LSST single-epoch limiting magnitude of $i_{AB} = 24.0$.

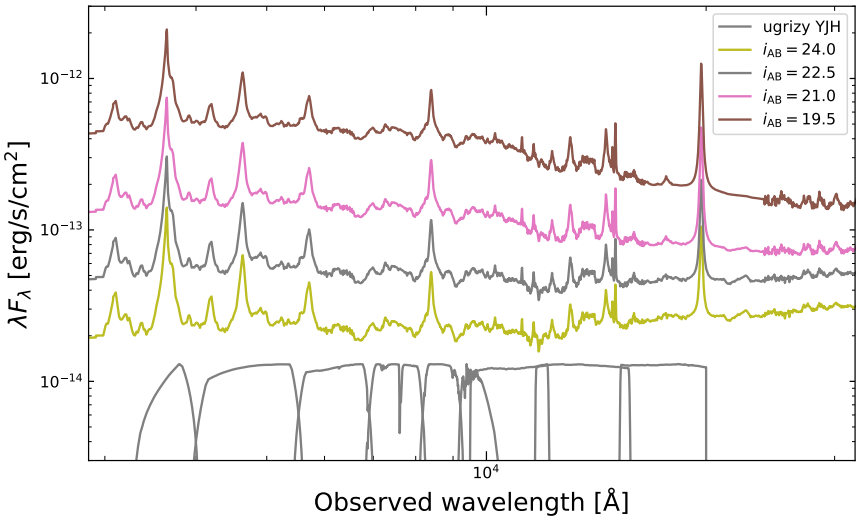

Figure 3.9: SEDs at redshift $z = 2$ corresponding to the predicted median colours for fainter *i*-band flux limits. LSST *ugrizy* and Euclid *YJH* filter response curves are shown for comparison. The increase in galaxy contribution at fainter magnitudes is evident in the change in continuum slope, especially in the Euclid passbands.

magnitude leads to significant changes in the predicted Euclid *YJH* colours at all redshifts $z > 0.5$. However, these predictions are based off a somewhat simplistic extrapolation of the trends observed in the colours of SDSS quasars, and it is not clear that the extrapolation is valid in the regimes that LSST will probe. Testing how well our predictions match the observed colours of fainter quasars in upcoming surveys will provide an interesting insight into the properties of those soon-to-be-discovered populations.

3.6 SUMMARY

The main results of this chapter are as follows:

- We have built a parametric SED model which is capable of reproducing the median optical and infrared colours of tens of thousands of quasars at redshifts $0.1 < z < 3.5$, to within ~0.1 magnitudes.
- As a function of apparent *i*-band magnitude, there are systematic changes in the average quasar colours, which are well-explained by changes in the strength of the emission lines and the contribution of the host galaxy.
- We quantify the changes in the model parameters as a function of *i*-band magnitude, and extrapolate to fainter magnitudes to make predictions for what the median LSST-Euclid colours

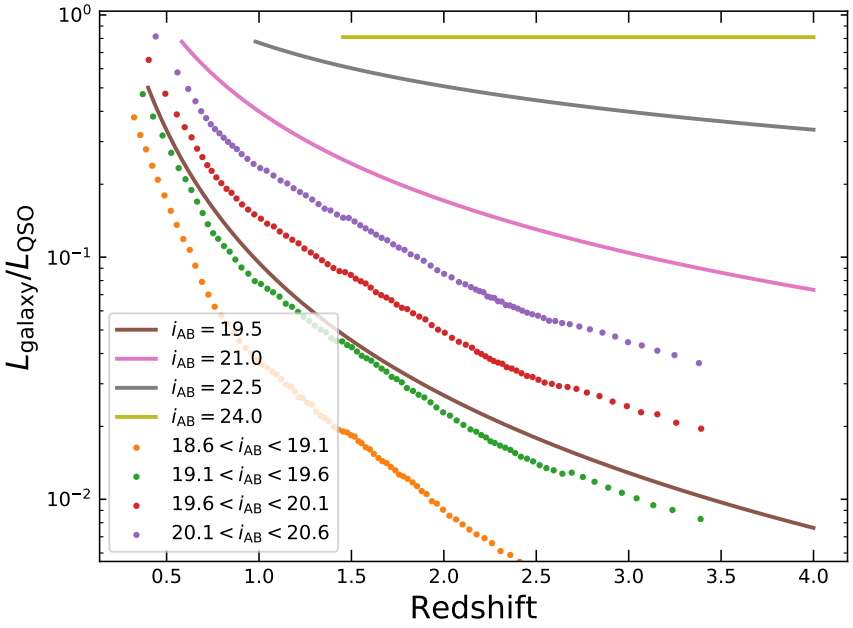

Figure 3.10: Ratio of integrated 4000-5000 Å luminosities for the galaxy and quasar components of our SED model. Points: best-fitting models to the average colours for the four flux regimes shown in Fig. 3.4. Solid lines: predicted models from extrapolating the trends observed in SDSS. The extrapolation reaches a regime at $i_{AB} = 24$ where the host galaxy is predicted to be a constant 45 per cent of the total 4000-5000 Å luminosity (80 per cent of the quasar component), irrespective of redshift. In reality we expect the predicted colours to cease to be accurate before that regime is reached.

of new populations of AGN might be, assuming the trends observed in SDSS continue for another 3 magnitudes in flux.

- In reality we expect our predictions for the average colours to break down before we reach $i_{AB} = 24$. When and how they break down will provide an insight into the physics of fainter quasars.

4

HOT DUST IN QUASARS

4.1 INTRODUCTION

It has been known for decades that quasars, and other AGN, show an excess of emission in the rest frame near-infrared at ~1-3μm. This emission is attributed to dust that has been heated to its sublimation temperature by the central continuum source (Barvainis, 1987; Rees et al., 1969; Rieke, 1978). Interferometric observations (Gravity Collaboration et al., 2020; Kishimoto et al., 2009, 2011) confirm that the emission from the shortest-wavelength components of the near-infrared excess is located close in to the central continuum source, while reverberation mapping studies have shown that the hot dust is located just outside the broad emission line region (BLR), perhaps even setting the outer limit of that region (Goad, Korista and Ruff, 2012; Landt et al., 2019; Minezaki et al., 2019; Suganuma et al., 2006).

The sublimation temperature of astrophysical dust in AGN is largely set by its composition, with little change expected for physically reasonable variations in the shape of the ionising SED or the size of the dust grains: pure silicate dust sublimates at temperatures around 1300-1500 K, and pure graphite dust at 1800-2000 K. This narrow temperature range allows a prediction to be made for the sublimation radius, which is larger than light-travel distance corresponding to the hot dust time lag found from reverberation mapping. These shorter-than-expected time lags suggest that the hot dust is located above the plane of the accretion disc, leading to a geometric foreshortening effect (e.g. Goad, Korista and Ruff 2012, fig. 1; Figaredo et al. 2020, fig. 14).

Over the past three decades, several authors have proposed models which use disc-driven winds to account for the dusty toroidal structures which obscure the inner regions of AGN from certain viewing angles (e.g. Hönig, 2019; Konigl and Kartje, 1994). More recently, models have been proposed which link these winds, or more specifically, associate the failed parts of these winds, with the broad emission line region (Baskin and Laor, 2018; Czerny and Hryniewicz, 2011; Czerny et al., 2017). These models predict that the properties of the BLR and the dust emitting regions should be related, however, observational studies to probe such links are somewhat small in number. One such study is that of Wang et al. (2013), who found that the rest frame near-infrared colours in a sample of ≃4700 quasars from the fifth data release of SDSS were correlated with the properties of the C IV λ1549 emission line. More specifically, within their 591 objects with the highest Eddington ratios, they found that the objects with broader C IV

emission lines show brighter emission at ≈3 μm in the 2012 All-Sky Data Release from WISE.

Since 2013, the reactivated NEOWISE project has continued to scan the sky, leading to a large improvement in the total amount of data gathered in the 3.4 and 4.6 μm *W1* and *W2* bands. The unWISE coadds presented by Meisner et al. (2019) make use of ten full-sky mappings in *W1* and *W2*, compared to the single full-sky mapping used to construct the 2012 WISE All-Sky Data Release, with a corresponding decrease in the noise associated with each photometric measurement. At the same time, the SDSS has continued to identify new objects: the fourteenth data release includes some 526 356 quasars, compared to the 77 429 from the fifth data release. This increase in sample size allows the hot dust properties to be quantified in a much larger number of quasars, and for the dependence of these parameters on the emission line properties *and* the Eddington fraction to be explored simultaneously. Recent work by Rankine et al. (2020) has developed an improved scheme for masking absorption features within the SDSS spectra, leading to an improved determination of the emission line properties in each object. In particular, the reported blueshift of the C IV emission line is now a more robust measurement of the strength of emission from outflowing gas.

The primary aim of this chapter is to quantify the properties of the high-frequency cutoff to the dust emission in luminous quasars, corresponding to emission from the hottest temperature dust, and to compare to the outflow signatures seen in the high ionisation broad emission lines. The rest frame near-, mid-, and far-infrared emission in quasars is due to several dust components at multiple temperatures: within the type-1 quasar population there exists a diversity of emission at $\lambda > 3$ μm, with the cooler dust emission (at longer wavelengths) not necessarily correlating with the hottest dust emission. These cooler components can be due to emission from dust at larger radii where the equilibrium temperature of the AGN-illuminated material is lower, and or due to dust in the host galaxy which has been heated by young stars. For this reason we restrict this investigation to emission at rest frame wavelengths shorter than 3 μm, where the emitting dust has temperatures $T \gtrapprox 1200$ K and must therefore be located near the inner regions of the AGN and heated by the ultraviolet–optical continuum from the central engine.

4.2 DATA

All the quasars used in this chapter are drawn from the SDSS fourteenth data release (DR14) quasar catalogue, the selection of which is summarised in Pâris et al. (2018).

The 'core' eBOSS quasar sample (Myers et al., 2015) makes up a significant fraction of the SDSS DR14 quasar catalogue. This sample

was in part selected using an optical–infrared colour cut, meaning that 'core' eBOSS quasars have a force-photometered weighted-average flux in WISE *W1* and *W2* above some threshold relative to the optical fluxes from the Sloan imaging data, which potentially biases our sample against quasars with weaker hot dust emission.

To test the effect of this selection criterion on our results, we have repeated all subsequent analysis using only objects with the `EBOSS_TARGET1` selection flag solely set to `QSO1_EBOSS_CORE`. This cut reduces our sample to the SDSS DR9 (Ross et al., 2012), which predates WISE, while still keeping all objects from SDSS-IV which were targeted through other programs. The total size of the DR14 quasar catalogue is reduced from 526 356 to 442 231 objects using this criterion. The results and conclusions of this chapter remain unchanged.

4.2.1 *Photometry*

We make use of the same SDSS, UKIDSS and unWISE photometry described in Chapter 3. In addition to the unWISE catalogue described in Section 3.2, we also match the DR14 catalogue to the AllWISE source catalogue. unWISE has ≈0.7 magnitudes deeper coverage in *W1* and *W2* compared to AllWISE, corresponding to additional data from the reactivation of NEOWISE. However, due to the lack of coolant on board the spacecraft, unWISE does not represent any improvement in the *W3* band, and so we must use AllWISE for data at observed wavelengths $> 6\,\mu$m. For AllWISE, we use only data points where the S/N is greater than 2 and we require the contamination and confusion flags to be set to zero in all bands, indicating that the source is not affected by any known image artifacts. The catalogue is matched to SDSS using a 3.0 arcsec matching radius, keeping only sources with unique matches within that radius. 397 873 AllWISE sources match to quasars from SDSS DR14. This is slightly less than the number found by Pâris et al. (2018), corresponding to the more stringent quality cuts we impose on the data.

4.2.2 *Spectroscopy*

For objects included in the Schneider et al. (2010) DR7 quasar catalogue, emission-line measurements are made using spectra (Wild and Hewett, 2010) processed using the improved sky-subtraction of Wild and Hewett (2005). For quasars identified after SDSS DR7 emission line measurements are derived from the spectra presented in Pâris et al. (2018). We make use of the C IV line properties presented by Rankine et al. (2020), as described in Section 1.3.1. We exclude all objects which show broad low ionisation absorption features (LoBALs), leaving 141 488 quasars with C IV information in the redshift range $1.56 < z < 3.50$.

4.2.3 *Systemic redshifts*

We use systemic redshifts calculated by P. Hewett using a mean-field independent component analysis scheme with the redshift as a free parameter. This scheme excludes the C IV emission line from the analysis to avoid biasing the systemic redshifts with information from skewed emission lines. These redshifts are the same as those presented in Rankine et al. (2020) for those quasars which have C IV line measurements.

4.2.4 *Black hole masses*

The asymmetry in C IV emission shows that at least some of the emitting gas is not virialised and deriving unbiased black hole masses from C IV is not straightforward (e.g., Coatman et al., 2017). For this reason, we instead use the Mg II λ2800 emission line to estimate black hole masses.

Black hole masses are estimated using the FWHM of the Mg II line and the single-epoch virial estimator described by Vestergaard and Osmer (2009), having subtracted Fe II emission using the template of Vestergaard and Wilkes (2001):

$$M_{BH} = 10^{6.86} \left(\frac{FWHM(Mg\,II)}{1000\,km\,s^{-1}} \right)^2 \left(\frac{L_{3000}}{10^{44}\,erg\,s^{-1}} \right)^{0.5} M_\odot \quad (4.1)$$

4.3 METHOD

We use the parametric SED described in Chapter 3 to model the quasar emission in the 1200 Å to 3μm rest frame wavelength range. The base model parameters, such as the slopes of the power-laws and the strength of the emission lines, are set to match the median observed colours as described in Chapter 3. The near-infrared component is modelled by a blackbody where the temperature and normalisation are both free to vary. An example SED is shown in Fig. 4.1 with the hot dust blackbody decomposed from the rest of the model. The total model can be reddened using a quasar extinction curve with the $E(B-V)$ as a free parameter. However, we do not interpret the modest range of derived $E(B-V)$ values as primarily resulting from dust reddening; rather it introduces flexibility to allow the model to account for slight variations in the quasar continuum slope. We thus allow the $E(B-V)$ to take negative values to account for objects which have bluer continua than average.

We note that the $\simeq$1 μm inflexion point in the quasar SED is sensitive to photospheric stellar emission from the host galaxy. In particular, objects with an excess of host galaxy emission which is otherwise unaccounted for will require a progressively hotter blackbody to

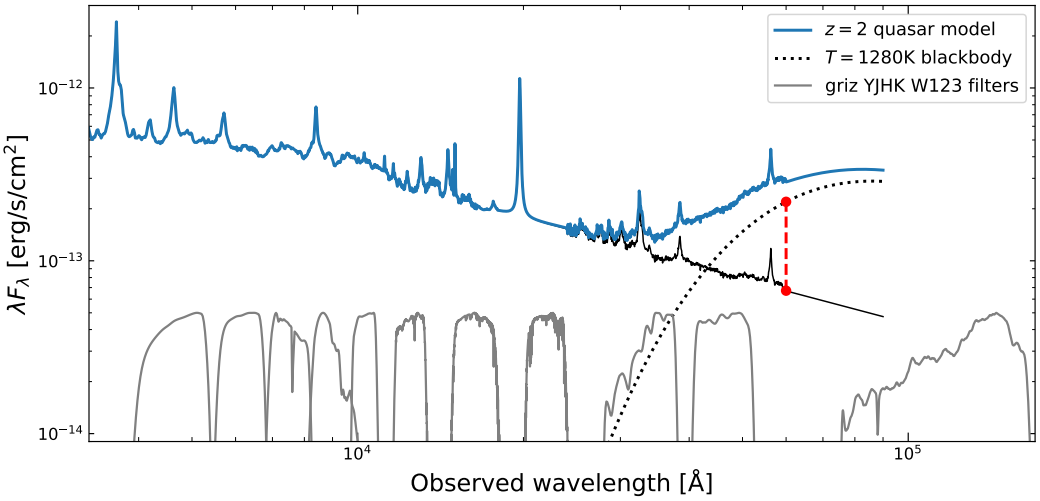

Figure 4.1: An example of our quasar model with $z = 2.0$, $E(B-V) = 0.0$, $L_{3000} = 10^{46}\,\mathrm{erg\,s^{-1}}$, and $L_{2\,\mu m,HD}/L_{2\,\mu m,QSO} = 4$. We quantify the near-infrared excess in the best-fitting model for each object in our sample using the ratio of the luminosities at 2 µm in the rest frame (red dashed line) of the hot dust blackbody (dotted black) and quasar power-law continuum (solid black). The normalised SDSS, UKIDSS and WISE filter response curves are shown in grey.

adequately account for the shape of the observed SED at wavelengths $\geqslant 1$ µm. However, due to the limited number of photometric data points which we have available to use in the rest frame near-infrared, the strength of the host galaxy emission and the temperature of the hot dust component are somewhat degenerate. We therefore chose not to include a host galaxy component in the model SED, but instead mitigate against this uncertainty by restricting our sample to objects which are classed as point sources in all UKIDSS bands, and impose additional flux limits to exclude fainter objects which are more likely to have a significant contribution from starlight.

We show in Section 4.4.4 that our results remain unchanged when including a component in our model to account for starlight from the host galaxy.

4.3.1 *Fitting routine*

For a given redshift, $E(B-V)$, blackbody temperature and blackbody strength, we generate a model SED. We multiply that SED by the *grizYJHKW12* filter response curves to obtain synthetic photometric colours. These are fit to the observed colours using a Nelder-Mead algorithm. A floor of 0.05 mag is imposed on the photometric uncertainties, corresponding to a minimum flux uncertainty of 5 per cent.

A simpler approach would be to treat each photometric passband as a monochromatic data point and fit a combination of power-laws to those data points (e.g. Wang et al., 2013). However, as the redshift of the source increases, the slope of the observed SED at ≃2-4 μm will change as the inflexion point moves to longer observed frame wavelengths. The change in SED slope leads to a change in the effective wavelength of each passband $\lambda_{\rm eff}$, and thus an additional uncertainty in the parameters of the best fitting model. The benefit of our approach, therefore, is that it avoids introducing additional redshift-dependant scatter in the measurement of the strength of the hot dust emission.

The SDSS *z* and UKIDSS *Y* filters overlap slightly and the observed $z-Y$ colour therefore has very little information content at the redshifts we consider, and for ease of computation we exclude the $z-Y$ colour when fitting our model to the data. The strongest emission line in the wavelength range of the type-1 quasars we consider is Hα, variation of which can change the total flux in an observed passband by up to ≃0.2 mag. We therefore exclude any band which includes Hα line at the redshift of a quasar. In practice this means that, for objects at redshift $1.2 < z < 2.0$, we exclude the $J-H$ and $H-K$ colours and instead include the $J-K$ colour when fitting our model to the data. All other optical and near-infrared emission lines have much smaller equivalent widths and the flux in all the other filters is dominated by continuum emission.

4.3.2 *Blackbody temperature*

We begin by exploring the range of best fitting blackbody temperatures in objects with redshifts $1.2 < z < 1.5$. This redshift range is chosen such that both the WISE *W1* and *W2* bands are probing the rest frame 1-3 μm portion of the SED. Two independent photometry points in this wavelength range allow us to fit a two-parameter model (i.e., both blackbody temperature and normalisation) to the data.

We keep only objects with $Y < 18.1$ which are classed as high confidence point sources in all four UKIDSS bands (i.e., `MERGEDCLASS==-1`) to avoid objects which are contaminated by host-galaxy emission, as described in Section 4.3. For this test we use unWISE photometry in preference to AllWISE data, and require a detection in all of the *grizYJKW12* bands, giving a sample of 1213 quasars.

We fit our model to each of the 1213 individual objects with the $E(B-V)$, the blackbody temperature, and the blackbody strength free to vary. The distribution of best fitting blackbody temperatures is shown in Figure 4.2. We find that the blackbody temperatures are evenly distributed around the median value of 1280 K.

We then repeat our fitting routine for the same sample, but this time fixing the blackbody temperature to be $T = 1280$ K. We find that fixing the blackbody temperature reduces the number of objects where the

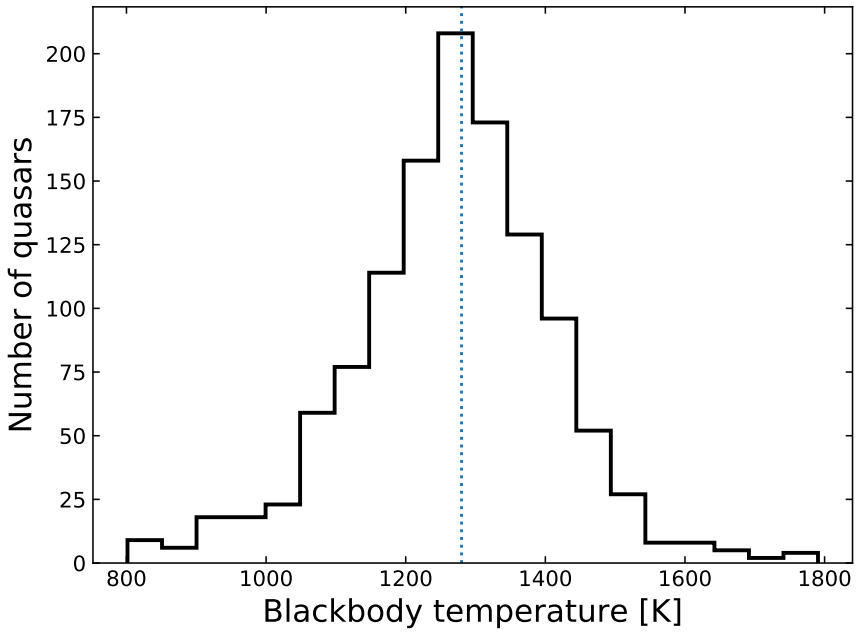

Figure 4.2: The distribution of blackbody temperatures in our sample of $1.2 < z < 1.5$, $Y < 18.1$ quasars. We find that the high-frequency cutoff to the infrared emission (i.e. the 1-3 μm region) can be well described by a 1280 K blackbody.

model might be over-fitting the data, while not increasing the number of objects with poor fits: for example, the number of quasars for which the χ^2 value per degree of freedom lies in the range 0.4-3.0 increases from 1098 to 1123 when fitting this simpler model.

We therefore proceed in the knowledge that the excess rest frame 1-3 μm emission in our sample of quasars can be adequately described using a fixed temperature $T = 1280$ K blackbody, consistent with an optically-thick emitting surface with the temperature set by dust sublimation. However, we ascribe no further significance to the exact value of this temperature, noting instead that it is merely the temperature describing the blackbody which best describes the infrared colours of the quasars, and not necessarily the physical temperature of the emitting dust. We show in Section 4.4.5 that our subsequent results remain unchanged when instead using a hotter or cooler blackbody in our model quasar SED.

4.3.3 *Primary sample*

Fixing the blackbody temperature allows us to fit our model to higher redshift objects, where we no longer have two independent data points probing the hottest dust emission.

For what we hereafter refer to in this chapter as our 'primary' sample, we take all quasars in the redshift range $1.2 < z < 2.0$, such

that the *W2* band is probing rest frame wavelengths where we expect the hot dust blackbody component to be dominant over the power-law continuum. We discuss the limitations of higher redshift samples in Section 4.4.7. As we require detections in all of the *JKW12* bands, and to avoid bias against hot dust faint objects which might drop out of one or more of these bands, we restrict our sample to $Y < 19.3$, where the sample is better than 95 per cent complete in all UKIDSS bands. Using unWISE as the source of data for *W1* and *W2* gives total sample of 12 294 objects. We show in Section 4.4.6 that our results are the same when instead using AllWISE as the source of WISE data. Only 243 objects are lost from the sample due to missing unWISE data, meaning our sample is better than 98 per cent complete in *W1* and *W2*. Some of these objects will be missing due to crowded fields as the WISE point spread function is significantly broader than that of SDSS. However, we cannot rule out the possibility that a small fraction of objects are lost due to intrinsically faint fluxes in the rest frame near-infrared.

We fit our primary sample with the model as described above, fixing $T_{\mathrm{blackbody}} = 1280\,\mathrm{K}$ and allowing the $E(B-V)$ and normalisation of the hot dust component to vary. Out of this sample, 5022 objects with $z > 1.56$ also have C IV line information from Rankine et al. (2020). As our primary sample is restricted to $z < 2.0$, Mg II emission is present in the SDSS spectra to enable black hole mass and Eddington ratio estimation.

4.4 RESULTS

We quantify our results using $L_{2\,\mu\mathrm{m,HD}}/L_{2\,\mu\mathrm{m,QSO}}$, the ratio of the luminosities at 2 μm of the hot dust blackbody and extended ultraviolet–optical power-law continuum in the best fitting model SED for each quasar. This ratio is effectively a measurement of the covering factor of the sublimation temperature dust around the ultraviolet continuum source.

For the primary sample described above, $L_{2\,\mu\mathrm{m,HD}}/L_{2\,\mu\mathrm{m,QSO}}$ takes values between 0 and ≈6, with a median value of 2.5.

4.4.1 *Trends with emission line outflow properties*

In Fig. 4.3 we show the strength of hot dust emission as a function of the blueshift of the median flux in the C IV emission line relative to the systemic frame. There is a clear trend: quasars with stronger emission from outflowing ionised gas also show stronger emission from the hottest temperature dust, when compared to their ultraviolet–optical continuum luminosity.

The median $L_{2\,\mu\mathrm{m,HD}}/L_{2\,\mu\mathrm{m,QSO}}$ for objects in our primary sample with C IV blueshift less than $200\,\mathrm{km\,s^{-1}}$ is 1.75, while the median

$L_{2\,\mu m,HD}/L_{2\,\mu m,QSO}$ is 3.09 for objects with C IV blueshift greater than $2000\,km\,s^{-1}$.

However, objects with fainter observed magnitudes will have larger photometric uncertainties, with the noisier photometry leading to increased uncertainty in our measurement of the hot dust luminosity. We would therefore expect the scatter in Fig. 4.3 to reduce if we restrict our sample to brighter objects. Taking only the objects with $Y < 18.3$, we find the median $L_{2\,\mu m,HD}/L_{2\,\mu m,QSO}$ for objects with C IV blueshift $< 200\,km\,s^{-1}$ decreases to 1.50, while the median $L_{2\,\mu m,HD}/L_{2\,\mu m,QSO}$ for objects with C IV blueshift $> 2000\,km\,s^{-1}$ increases to 3.14.

The covering fraction of hot dust around the continuum source in our sample of quasars is therefore increasing, on average, by a factor of at least two as we go from objects with C IV emission predominantly at the systemic redshift to objects where the kinematics of the C IV emission are dominated by outflowing gas. The presence of a strong nuclear outflow, such as described by a disc-driven wind, must therefore correlate with significant changes in either the geometry or extent (or both) of the hot dust emitting surface.

4.4.2 *Luminosity and Eddington fraction*

It is known that the C IV emission line properties are correlated with other intrinsic quasar properties (Rankine et al., 2020; Richards et al., 2011), with stronger outflow signatures seen in objects which are generally brighter and have a higher Eddington ratio. We therefore need to determine whether the variation in the hot dust emission observed in Fig. 4.3 is primarily driven by changes in the outflow properties of the BLR, or whether it is instead a by-product of a more fundamental correlation.

In Fig. 4.4, we show the median $L_{2\,\mu m,HD}/L_{2\,\mu m,QSO}$ in bins of luminosity, Eddington ratio and C IV blueshift. We recover the known relationship between C IV blueshift and L/L_{Edd}, in that only objects with larger Eddington fractions are observed to have strong emission-line outflow signatures. However, when controlling for the observed outflow properties, i.e. taking fixed values of C IV blueshift, we do not see any trend in the hot dust emission strength as a function of either the Eddington ratio or the continuum luminosity. There is no correlation between $L_{2\,\mu m,HD}/L_{2\,\mu m,QSO}$ and the black hole mass estimated from Mg II. In other words, the correlation between the strength of the hot dust emission and the blueshift of the C IV emission line is not a secondary effect driven by the black hole mass, continuum luminosity, or Eddington ratio.

We note that measuring an Eddington fraction requires knowledge of the bolometric luminosity of the quasar, and we have shown that some quasars show significantly more emission in the infrared than others of the same ultraviolet luminosity. Hence, it is possible that

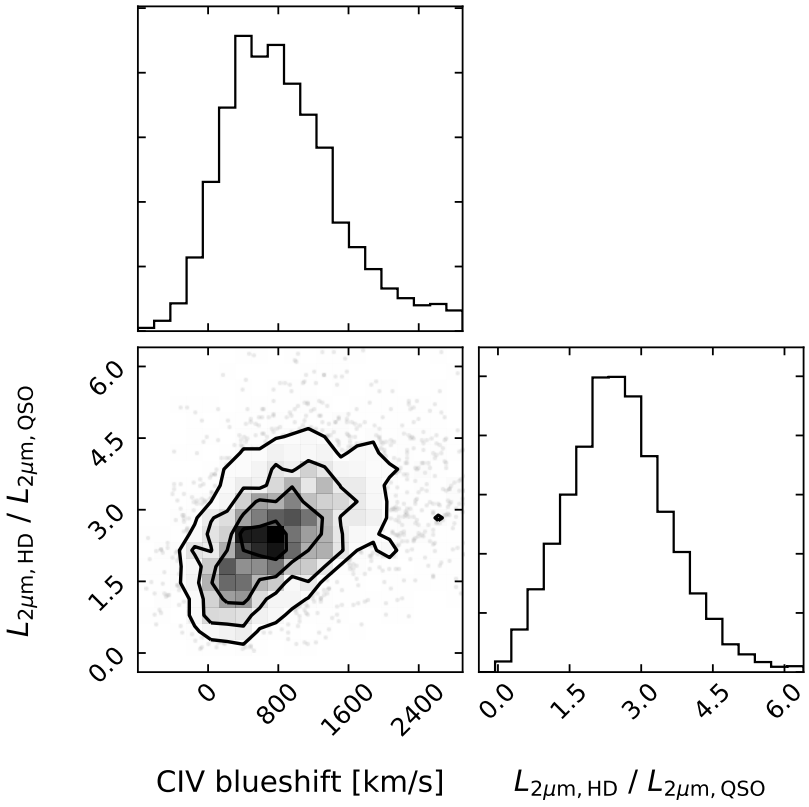

Figure 4.3: Results of fitting our model to the 5022 quasars from the primary sample with spectral coverage of C IV. The bottom left panel shows the distribution of our sample in the plane of C IV blueshift and hot dust strength, with points representing individual objects and darker shades representing regions of higher point density. The contours enclose 86, 68, 39 and 12 per cent of the sample respectively. The normalised 1-D distributions of each parameter are shown in the top left and bottom right. Objects with stronger C IV outflow signatures tend to have stronger hot dust emission.

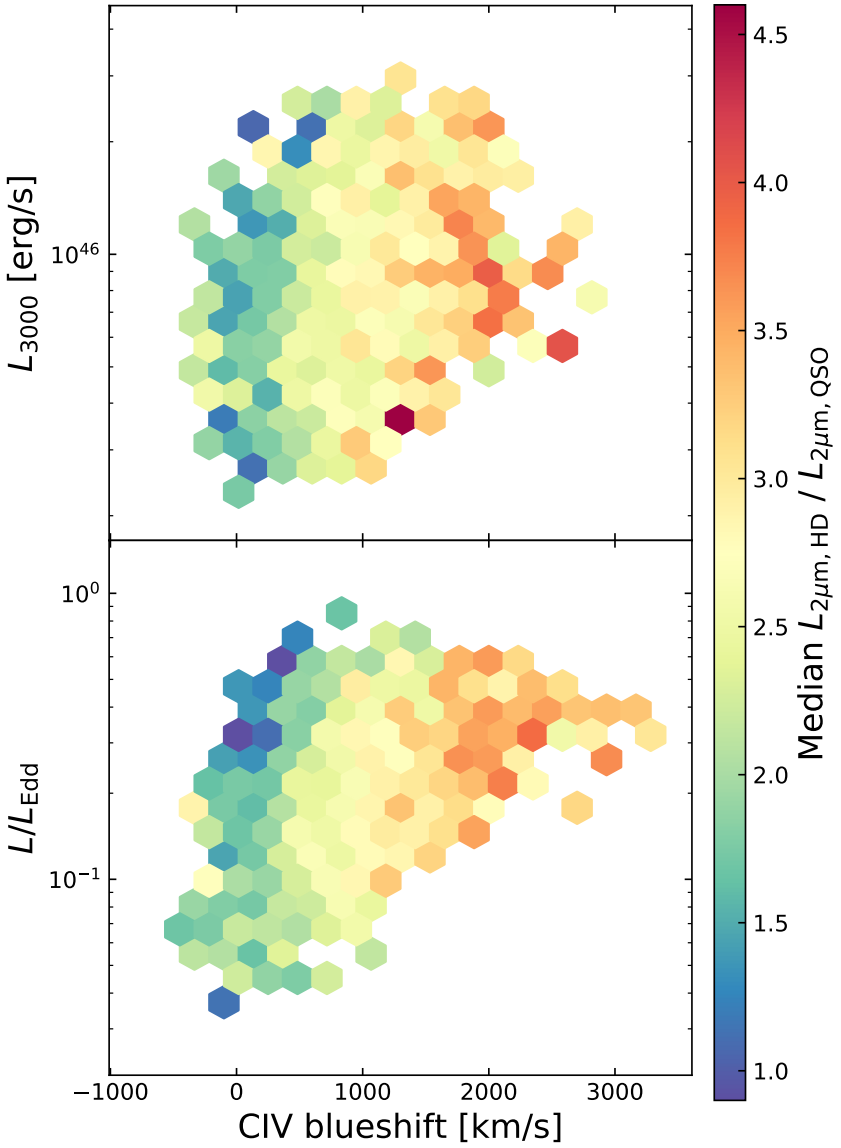

Figure 4.4: The median hot dust strength in binned regions of parameter space. Only bins with five or more objects are plotted. At fixed values of C IV blueshift, the relative strength of hot dust emission is not dependant on either the continuum luminosity or the Eddington ratio, although objects with stronger C IV outflow signatures and hence stronger hot dust emission are only found at $L/L_{Edd} \gtrapprox 0.2$.

objects with a larger $L_{2\,\mu m,HD}/L_{2\,\mu m,QSO}$ for a given 3000 Å luminosity have a slightly larger bolometric luminosity, and thus the Eddington ratios shown in Fig. 4.4 might be systematically under-estimated as we move to objects with stronger hot dust emission.

However, we note that a larger uncertainty in the estimation of a bolometric luminosity arises from the 'unseen' extreme ultraviolet continuum (e.g., Krawczyk et al., 2013), and that there are also inherent uncertainties in the estimation of black hole masses of order 0.5 dex, and so the uncertainty in L/L_{Edd} arising from the variation in the strength of the near-infrared emission from hot dust is sub-dominant compared to other uncertainties in that measurement.

4.4.3 *Broad absorption line quasars*

Using the spectral reconstructions presented in Rankine et al. (2020), we can also measure C IV emission line properties unaffected by absorption for those quasars which show high ionisation broad absorption features in their spectra ('HiBAL' quasars). For a given C IV blueshift and equivalent width, we find no significant difference in the hot dust emission strengths in HiBAL and non-BAL quasars, as shown in Fig. 4.5.

We note that quasars which show larger C IV emission line blueshifts also show faster and stronger broad absorption troughs (Rankine et al., 2020). We have shown above that the strength of hot dust emission is correlated with the C IV blueshift, and therefore expect quasars with the most extreme broad absorption features to also show stronger hot dust emission, consistent with the results of Zhang et al. (2014).

4.4.4 *Host galaxy flux*

The emission from the rest frame 1-3 μm portion of the galaxy SED is largely dominated by flux from older, cooler stellar populations, and hence it is extremely unlikely the emission is correlated with the AGN outflow properties when the quasar duty cycle is much shorter ($\sim 10^6$ years) than the age of these stars. Moreover, the flux λF_λ from starlight is reasonably flat across the $\simeq$ 0.7-2 μm portion of the SED, irrespective of the galaxy type (e.g. Rowan-Robinson et al., 2008), and it is very hard to explain the variation in the strength of the 1-3 μm excess observed in luminous quasars as due to any variation in the host galaxy. In other words, the changes in the slopes of the optical and near-infrared parts of the total SED are very different when varying the strength of the hot dust emission compared to those arising from a variable fractional host galaxy contribution, as shown by the 'mixing diagrams' of Hao et al. (2013). We are therefore confident in interpreting the variation in the 1-3 μm emission as arising from the sublimation-temperature dust around the AGN.

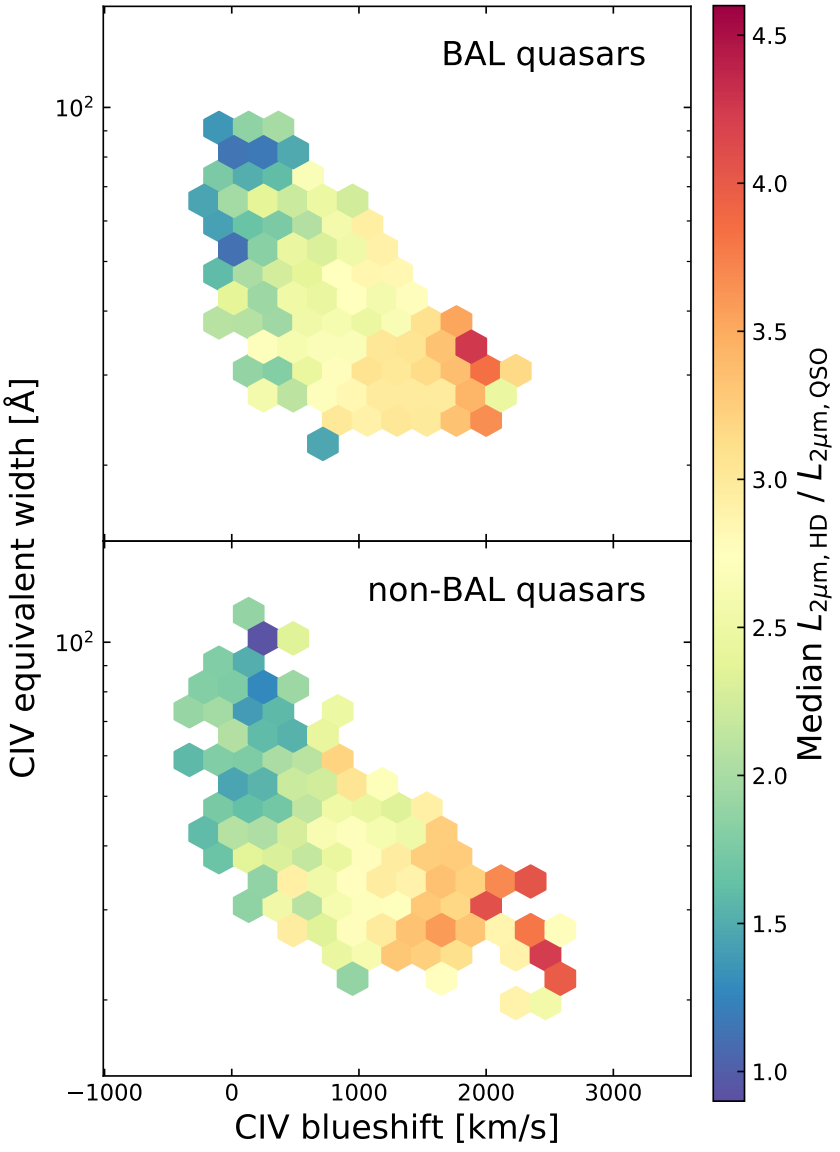

Figure 4.5: Comparison of the hot dust emission in quasars which show high ionisation broad absorption lines (top) and those which don't (bottom). Only bins with five or more objects are plotted. For a given C IV blueshift and line equivalent width, significant differences in the median strength of hot dust emission are not seen.

However, while we take steps to mitigate against the contamination of the rest frame 0.7-3 μm region by starlight from the host galaxy (i.e. requiring point-source detections in all UKIDSS bands), the possibility remains that the strength of hot dust emission is affected by some relatively small amount of flux from the host galaxy. We have therefore re-run our fitting routine, including an Sb galaxy template from the SWIRE library (Rowan-Robinson et al., 2008) in our SED model with a fixed normalisation such that the integrated galaxy flux in the wavelength interval 4000-5000 Å is 10 per cent of the integrated quasar flux across the same interval. For a model with an average amount of hot dust emission, this normalisation corresponds to a flux at 1 μm from starlight 0.5 times that of the flux due to the quasar.

The exact shape of the host galaxy SED does not matter; the desired effect is to add flux to the 1 μm inflexion-point of the total quasar SED. For the range of quasar extinctions in our sample of SDSS objects (i.e. $E(B-V) \lesssim 0.2$), our prescription is such that the starlight component has a negligible effect on the bluer parts of the total SED.

Including this additional galaxy-component in our model, we find that the median blackbody temperature (Section 4.3.2) decreases from 1280 to 1190 K, and adopt this temperature as a fixed parameter in the same way as described in Section 4.3. The inclusion of the galaxy template has the effect of flattening the 1 μm inflexion point in the total model SED for any given strength of hot dust emission. Combined with the difference in shape of the slightly cooler blackbody, this results in an increase in the normalisation at 2 μm of the best-fitting hot dust by a constant factor of about 50 per cent. The results and conclusions of this chapter remain unchanged.

4.4.5 *Blackbody temperature*

The effect of changing the temperature of the blackbody used to model the hot dust emission is shown in Fig. 4.6. Using 1180 K or 1380 K instead of our adopted 1280 K as the temperature of the blackbody in our SED model results in an increase in the median χ^2 per degree of freedom from 1.30 to 1.33 in each case, but our results are not sensitive to the exact temperature adopted. In short, if we were to adopt a different temperature blackbody to describe the near-infrared rest frame emission in our model SED, the conclusions of this chapter would remain unchanged.

4.4.6 *Comparing unWISE and AllWISE data*

In Fig. 4.7, we compare the effect of using AllWISE *W1* and *W2* photometry in place of unWISE when fitting to our primary sample. The unWISE catalogue presented by Schlafly, Meisner and Green (2019) makes use of additional data corresponding to the reactivation

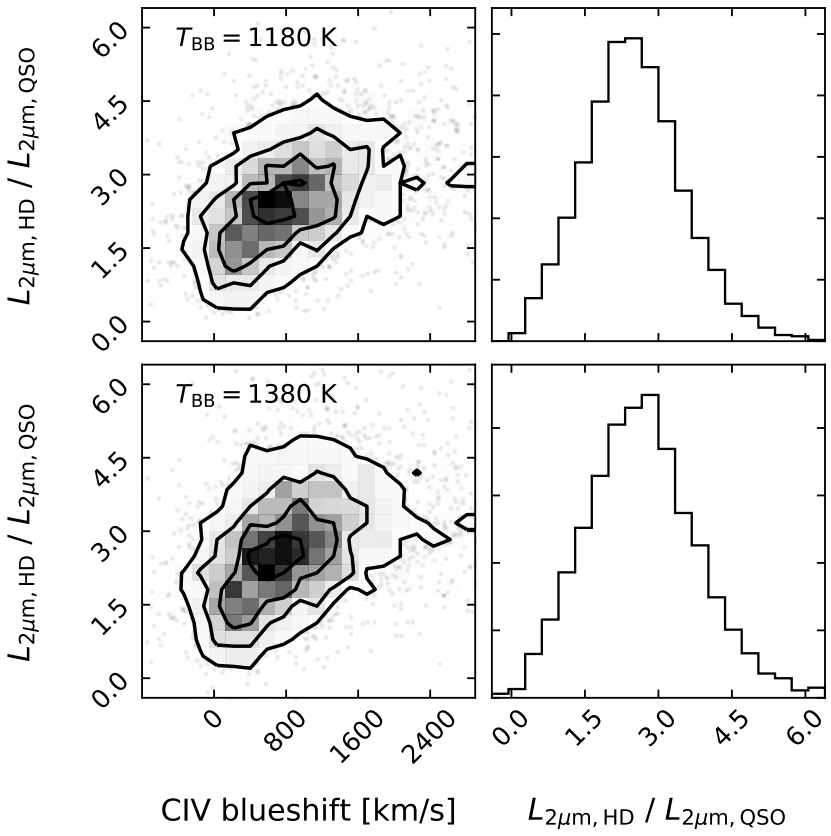

Figure 4.6: Comparison of the strengths of hot dust in the best fitting models when using a blackbody temperature of 1180 K (top) or 1380 K (bottom). On the left is the distribution of $L_{2\,\mu m,HD}/L_{2\,\mu m,QSO}$ as a function of C IV blueshift, and on the right is the normalised 1-D distribution. Our results (c.f. our adopted 1280 K model in Fig. 4.3) are not sensitive to the exact form of the blackbody we use to model the SED.

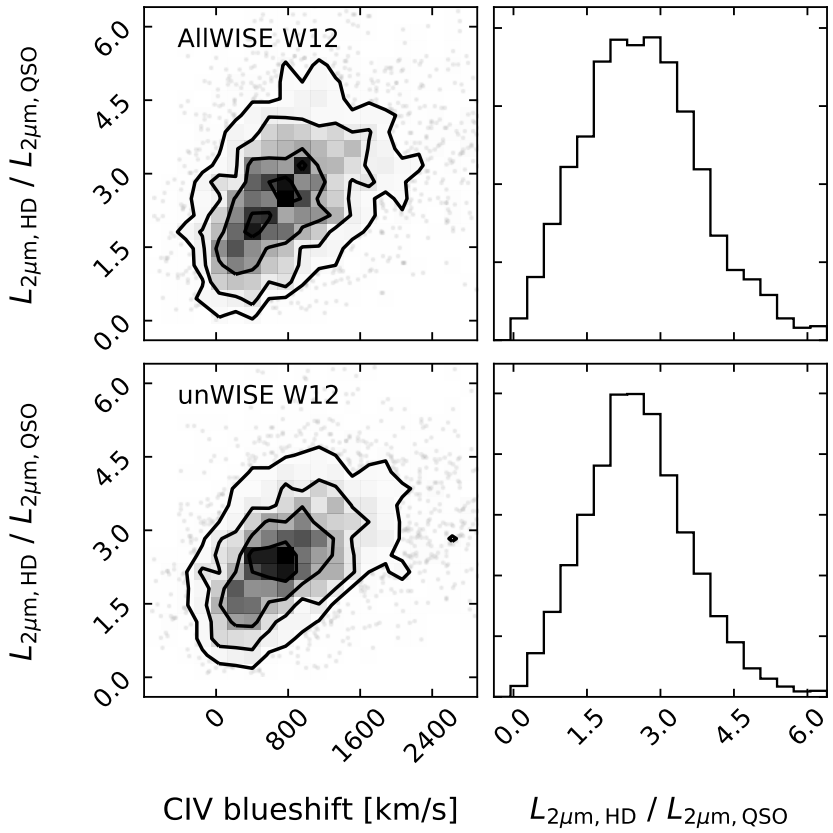

Figure 4.7: Comparison of the strength of hot dust in the primary sample when using AllWISE *W1* and *W2* (top) instead of unWISE data (bottom). On the left is the distribution of $L_{2\,\mu m,HD}/L_{2\,\mu m,QSO}$ as a function of C IV blueshift, and on the right is the normalised 1-D distribution. Using the deeper photometric data leads to a reduction in the scatter in best-fitting model parameters.

of the WISE satellite as NEOWISE. The vast majority of our sample are detected in both catalogues, but the additional depth of unWISE corresponds to reduced uncertainty in the *W1* and *W2* photometry, which leads to a noticeable reduction in the scatter of the normalisation of the best-fitting hot dust blackbody.

While all the results hold true whether AllWISE or unWISE is used, we have chosen to use unWISE data where possible to improve the detectability of trends in our results.

4.4.7 *Redshift evolution*

To investigate the hot dust properties in the quasar population at higher redshifts, it is necessary to make use of data at longer observed wavelengths. We have experimented with using the AllWISE *W3* band to constrain the properties of the hot dust emission. How-

ever, *W3* is a much broader band than either *W1* or *W2* (see Fig. 4.1) limiting us to a narrow redshift range where *W3* is not covering any wavelengths longer than 3 μm in the rest frame, while also not covering any wavelengths shorter than 1 μm.

We take all objects with $2.75 < z < 3.25$ and *rizYJHKW123* data. We exclude *g* due to Lyman suppression in the intergalactic medium at these redshifts. AllWISE *W3* is not as deep as the shorter wavelength bands and a brighter flux limit of $Y < 18.3$ is necessary to ensure the sample is more than 95 per cent complete in *W3*. The selection gives a total of 701 objects, where we use unWISE as the source of *W1* and *W2* data. Allowing the blackbody temperature to vary in the same way as described in Section 4.3.2 also gives a median $T_{blackbody}$ of 1280 K for this higher-redshift sample, and we fit our model using the same parameters as the primary sample.

The median strength of hot dust emission $L_{2\,\mu m,HD}/L_{2\,\mu m,QSO}$ in this higher-redshift sample is found to be 2.53, very similar to that of the primary sample. The strength of the hot dust emission in our $z \simeq 3$ sample also shows a significant correlation with the blueshift of the C IV emission line. However, the difference in filter response curves between *W2* and *W3*, coupled with the different noise properties of each photometric band, combine to give a significant difference in the scatter around the intrinsic hot dust strength. For example, a one-sigma change in the *W2* measurement for a $z = 2$ object will have a different effect on the best-fitting hot dust strength than that resulting from a one-sigma change in the *W3* measurement for a $z = 3$ object. For this reason, while the average amount of hot dust in our $z \simeq 3$ sample appears to be the same as in the primary sample, a detailed comparison of the distribution of hot dust properties within each redshift bin is not appropriate.

4.5 DISCUSSION

In the previous section, we have shown that the strength of the hot dust emission in type 1 quasars strongly correlates with the blueshift of the C IV emission line. Moreover, when holding the C IV blueshift constant, the hot dust emission does not correlate with luminosity, black hole mass, or Eddington ratio.

The variation in hot dust emission strength could be ascribed to one of two factors: either there is a change in the total area of the hot dust 'surface' which is surrounding the central continuum source, or the inclination of this surface is changing relative to the observer. In other words, if we assume that the hottest dust emission is coming from a thin 'zone' or surface, which is optically thick (so only cooler dust components emit from behind it), then the change in hot dust strength we observe could either be due to an increase in the vertical extent (or possibly the azimuthal covering fraction) of the hot dust such that it

is covering a larger physical surface area, or it could be that the total amount of hot dust is actually the same, but the opening angle of the hot dust emitting surface is changing such that more of it is projected onto the plane of the sky of the observer.

4.5.1 *'Failed wind' models of the broad line region*

One theory for the origin of the BLR which has gained popularity is that of a 'failed wind', where the BLR gas at the systemic redshift is gas which has failed to reach escape velocity and form a wind, and has instead fallen back to the disc (Baskin and Laor, 2018; Czerny and Hryniewicz, 2011; Czerny et al., 2017). The failed wind model is consistent with the first-order behaviour of the broad emission lines, where the equivalent width of lines such as C IV, C III], Lyman α, and indeed the Balmer lines, is observed to anticorrelate with the blueshift of the C IV line.

However, as discussed by Giustini and Proga (2019), a more nuanced version of this picture exists, in which the high and low ionisation parts of the BLR arise in different locations: the high ionisation lines (such as C IV) arise closer in and form from a failed line-driven wind, whereas the low ionisation lines (such as Mg II) form further out from a failed wind which would otherwise be driven by radiation pressure on dusty grains. This model of failed winds with multiple driving mechanisms is consistent with the picture of the BLR derived from reverberation mapping, which has a stratified velocity structure wherein high ionisation lines respond to the continuum on shorter time-scales than the low ionisation lines.

On first sight, our results would appear to be in slight tension with this model: one natural explanation for the correlation we observe between the hot dust emission and the C IV blueshift would be if the hot dust is itself providing the opacity to accelerate the outflow off the disc which we then observe in the ionised gas kinematics. On the other hand, however the outflow is formed, even if MHD driven (Elitzur and Shlosman, 2006; Murray et al., 1995), we would still expect dust to form inside the wind (Sarangi, Dwek and Kazanas, 2019). Thus, however the wind(s) are driven, there are perhaps good theoretical reasons to expect that they may correlate with dust emission. The fact that we observe this dust to be near the sublimation temperature therefore suggests that, if it is not already present and providing the opacity to drive the outflow through radiation pressure, the dust in the wind must be re-forming at (or near) a height above the disc corresponding to the limit of the dust sublimation region.

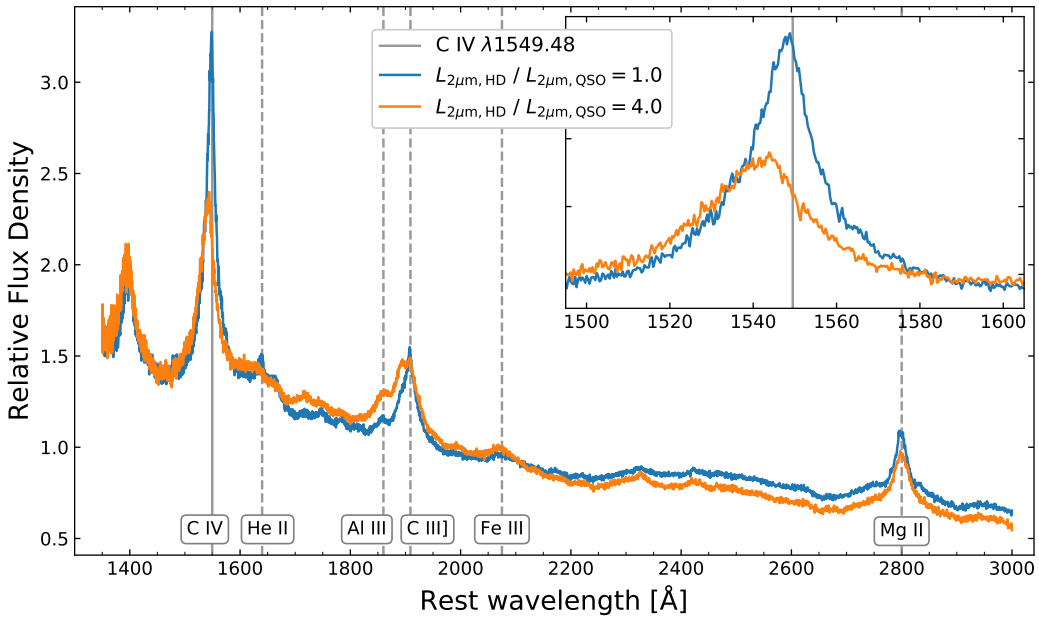

Figure 4.8: Composite spectra for objects with extremely strong (weak) hot dust emission, plotted in orange (blue). Both samples have average black hole mass $10^{9.3}\,M_\odot$ and average accretion rate $L/L_{Edd} = 0.26$. The rest frame wavelength of the C IV emission line is marked in solid gray. Objects with stronger hot dust emission tend to have stronger emission in the blue wing of the C IV line and weaker emission at the systemic wavelength, combining to give an asymmetric and blueshifted line profile indicative of outflowing gas. Such objects tend to have a bluer ultraviolet continuum, suggesting that the hot dust is not obscuring the central source. The objects with weaker hot dust emission have stronger emission from other broad lines such as He II λ1640 and C III] λ1909, consistent with a scenario in which part of the broad emission line region is produced from gas which fails to form an outflowing wind.

4.5.2 *Ultraviolet continuum slope*

In Fig. 4.8, we show stacked spectra in bins of hot dust strength. The two bins have been chosen to be matched in Eddington fraction: each quasar contributing to the composites has $-1.0 < \log(L/L_{Edd}) < -0.2$ and the average accretion rate in each composite is $L/L_{Edd} = 0.26$. Each bin contains 84 objects.

We can see that quasars with stronger hot dust emission tend to have slightly bluer UV continua on average, consistent with their observed photometry: quasars with $L_{2\,\mu m,HD}/L_{2\,\mu m,QSO} \simeq 1$ have a median colour $g - K = 2.32$, while quasars with $L_{2\,\mu m,HD}/L_{2\,\mu m,QSO} \simeq 4$ have a median colour $g - K = 1.98$. Equivalently, our best fitting SED models (Section 4.3) have average $E(B-V)$s of 0.020 and -0.017 respectively. We would expect any dust obscuration to redden the continuum, and so the fact that quasars with stronger hot dust emission are observed to have slightly bluer UV–optical continua suggests that the emitting hot dust does not intersect the line of sight to the accretion disc.

This finding is consistent with the results of Kim and Im (2018), who find that the hot dust emission is not significantly stronger in dust-reddened quasars (with $E(B-V) \approx 1$) when compared to their unobscured counterparts.

The correlation between SED slope and hot dust strength is consistent with known trends with the C IV line, where objects with larger emission line blueshifts tend to have bluer ultraviolet continua (Rankine et al., 2020; Richards et al., 2011). We can also see from Fig. 4.8 that the objects with stronger hot dust emission also have stronger Al III λ1860 and Fe III λ2075, consistent with the results of Chapter 2 which showed that quasars with stronger C IV outflow signatures show stronger emission from dense gas close-in to the central ionising source.

4.5.3 *Bolometric corrections and EUV flux*

Estimating an Eddington fraction requires knowledge of the bolometric luminosity of the quasar, and we have shown that some quasars show significantly more emission in the near infrared than others of the same 3000 Å luminosity. It is true that objects with a larger $L_{2\,\mu m,HD}/L_{2\,\mu m,QSO}$ for a given 3000 Å luminosity will have a larger contribution to their bolometric luminosity (and thus their Eddington fraction) from the rest-frame near infrared. However, a larger uncertainty in the inference of a bolometric luminosity arises from the 'unseen' extreme ultraviolet (EUV) continuum (e.g., Krawczyk et al., 2013). There are also inherent uncertainties in the estimation of black hole masses of order 0.5 dex, and so the uncertainty in L/L_{Edd} in Fig. 4.4 arising from the variation in the strength of the hot dust

emission is sub-dominant compared to other uncertainties in that measurement.

Indeed, it has been suggested that the ratio of EUV flux to optical flux varies as a function of Eddington fraction, with higher accretion rate AGN having stronger EUV emission by factors of at least a few (e.g. Jin, Ward and Done, 2012). If this change in EUV flux is responsible for driving the outflows inferred from the C IV line profiles, then it is possible that the relative strength of the EUV flux might be responsible for the correlation between C IV blueshift and hot dust emission reported in this work. Increasing the amount of EUV flux (at fixed L_{3000}) would increase the amount of energy which is available to heat the dust and therefore increase the strength of hot dust emission which we measure relative to the optical continuum. The relative weakness of He II emission seen in Fig. 4.8, despite the hypothesised increase in EUV flux, could then be explained decreasing the covering fraction of line-emitting clouds with increasing Eddington fraction, as discussed by Ferland et al. (2020). In this scenario, the assumption of a constant bolometric correction which we have made throughout this work would clearly be wrong, and the Eddington fractions which we have inferred would be biased high in low-blueshift objects and biased low in high-blueshift objects.

4.5.4 *Comparison with Jiang et al. (2010)*

Jiang et al. (2010) reported the discovery of two quasars (from a sample of 21) at redshift $z > 6$ with very weak hot dust emission, and suggested that these were 'first-generation quasars born in dust-free environments' in the early universe, i.e. quasars which were too young to have been able to form dust around them, or at least enough dust to be detected in the rest frame near-infrared. We note that these two quasars, J0005-0006 and J0303-0019, both show very narrow, symmetric C IV emission line profiles, as can be seen from their spectra (Kurk et al., 2009; Kurk et al., 2007). In our parametrization, these two objects would lie in the bottom-left corner of Fig. 4.3, and we believe that these two quasars are consistent with the trend between the hot dust emission and the emission line properties which we have identified at $z \leqslant 2$. Our results would therefore imply that the unusual infrared properties of these $z > 6$ objects are driven by the shape of their ionising SEDs, or whatever else is responsible for their (lack of) BLR outflows, and not by the dust content of their environments.

4.5.5 *Hot dust reverberation*

Reverberation mapping (RM) experiments have found that the time lag in the response of the hot dust emission to variations in the optical continuum (τ) is well enough correlated with the AGN luminosity

to lead to the idea of using the hot dust reverberation in AGN as a standardisable candle which could be used to test and constrain cosmological models (e.g. Hönig, 2014; Hönig et al., 2017).

The results of this chapter show that there are systematic changes in either the geometry or extent (or both) of the hot dust emitting surface in luminous quasars as a function of their ionised gas outflow properties. If the variable component of the hot dust emission is the same as the 'static' emission quantified in this work, then these changes could potentially introduce a C IV-blueshift dependant bias into the lag-luminosity relation which is used to estimate the intrinsic brightness of the AGN. However, theoretical work has shown that the infrared response function is not very sensitive to the exact distribution of the reverberating dust (Almeyda et al., 2020). RM experiments to date have found a small scatter in the lag-luminosity relation, which does not appear to increase with Eddington ratio (S. Hönig, priv. comm.), suggesting that any outflow-dependant changes in the hot dust reverberation properties are small compared to other sources of scatter in the $\tau - L$ relation. While there is therefore no direct evidence that the $\tau - L$ relation is affected by any outflow properties, we note that the majority of hot dust RM experiments have so far been conducted on local Seyfert galaxies with $L/L_{Edd} < 0.3$ (Koshida et al., 2014; Suganuma et al., 2006), where we do not expect to see large C IV blueshifts.

4.6 SUMMARY

Using photometric data from SDSS, UKIDSS-LAS and unWISE, we have investigated the properties of the hot dust emission in luminous type 1 quasars across the redshift range $1.2 < z < 2.0$. We find that the 1-3 μm excess in quasars can be well described by a single temperature blackbody, consistent with emission from sublimation temperature dust. We quantify the strength of the hot dust emission as the normalisation of this blackbody relative to the ultraviolet–optical power-law continuum at 2 μm. Our main results are as follows:

- The strength of the hot dust emission correlates with the strength of the blueshift of the C IV emission line. In a disc-wind model, this suggests objects with more wind-dominated emission have a larger surface of sublimation-temperature dust visible to the observer.

- When controlling for the emission line properties, the strength of the hot dust emission does not vary with luminosity, black hole mass, or Eddington fraction. In the picture presented by Giustini and Proga (2019), this would imply that the main driver of the wind, whether increased M_{BH} at lower L/L_{Edd}, or increased L/L_{Edd} at lower M_{BH}, does not affect the emission from hot dust.

- Stacking the rest frame ultraviolet spectra of these quasars, we find there is a small but significant change in the average slope of the ultraviolet continuum with varying hot dust emission strength: objects with stronger hot dust emission tend to have bluer continua. The parity of this change in slope suggests that the sublimation-temperature dust is not located along the line of sight towards the source of the ultraviolet continuum, and is consistent with previously reported empirical correlations between the quasar SED, the quasar outflow properties, and the strength of emission from He II λ1640.

- There appears to be no difference in the hot dust properties of BAL and non-BAL quasars at given C IV line properties, consistent with the result found by Rankine et al. (2020) that BALs and non-BALs are drawn from the same parent population.

Outflows off the accretion disc could be driven by radiation pressure on dusty gas, or by other mechanisms, and our results are not able to rule out any specific mechanism. However the winds are formed, they do correlate with the properties of the hottest emitting dust. Dust of this temperature cannot be heated by star formation, and therefore provides evidence of a direct link between the properties of the broad emission line region and properties of the dust emitting regions.

5

[O III] EMISSION IN HEAVILY REDDENED QUASARS

5.1 INTRODUCTION

Merger-driven models of galaxy evolution (e.g., Hopkins et al., 2008; Sanders et al., 1988) normally predict a reddened quasar phase: as the galaxy merger triggers luminous AGN activity, it also triggers a burst of intense star formation, which in turn produces large amounts of dust that redden the line of sight to the SMBH. Such models rely on a 'blowout' phase, where large scale outflows are driven from the AGN to disrupt the gas in the host galaxy, shutting down star formation and clearing obscuring material away from the line of sight to reveal a luminous blue quasar.

In particular, the Eddington limit given in Eq. 1.5 is modified to become smaller in the presence of dust, as the dust absorption cross-section is larger than the Thomson cross-section (Fabian, Celotti and Erlund, 2006; Fabian, Vasudevan and Gandhi, 2008). If the merger-driven paradigm of galaxy formation is correct, and if radiation pressure on dusty gas is a significant driver for AGN winds, one would therefore expect to see evidence for more powerful outflows in observations of luminous reddened quasars than in unobscured quasars, for example through broader wings in the [O III] emission line, while the dusty obscuring material is in the process of being cleared from the line of sight.

Recent work by several groups has shown that red and reddened quasars across a wide range of redshifts and luminosities often present evidence for ionised gas outflows (e.g., Brusa et al., 2015; DiPompeo et al., 2018; Harrison et al., 2016; Zakamska et al., 2016). The occurrence of such outflows has been interpreted as showing that the red selection (i.e. the selection of objects with more obscuring dust) is responsible for the observed outflow properties, and thus that the obscuring dust is at least in part responsible for driving AGN feedback mechanisms. However, there has been no systematic, luminosity-matched comparison of reddened and unobscured quasars at $z > 2$, corresponding to the epoch of peak star formation and peak AGN activity (Kulkarni, Worseck and Hennawi, 2019; Madau and Dickinson, 2014).

Using near-infrared data, Banerji et al. (2012, 2013, 2015) and Temple et al. (2019) have discovered a population of heavily dust-reddened ($E(B-V) \approx 1$), broad line (i.e., spectroscopic type 1) quasars at redshifts $z \approx 2$. These quasars have been selected to have extinctions similar to those in sub-millimetre galaxies, as one would expect following an intense burst of star formation triggered by a major merger.

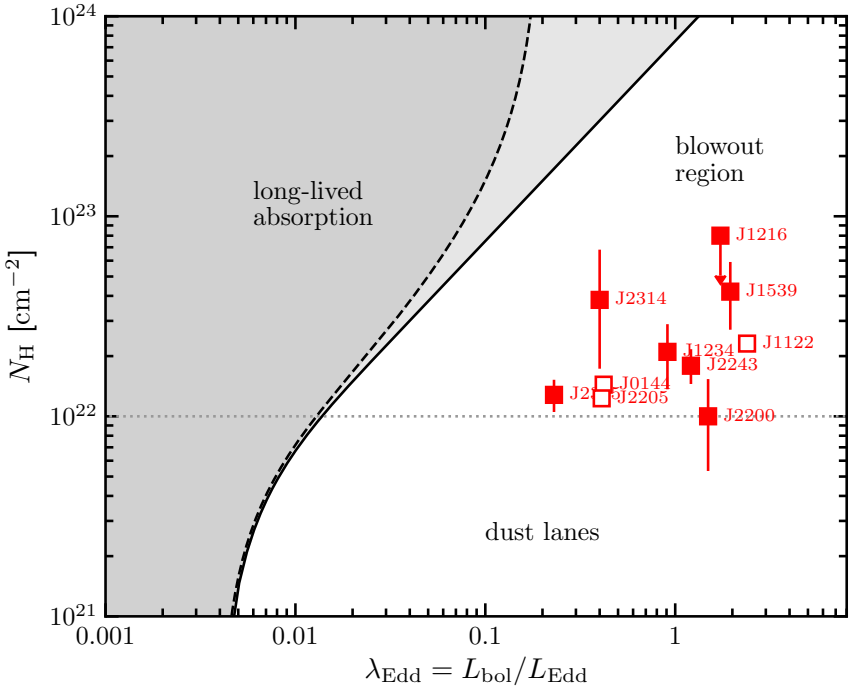

Figure 5.1: The plane of X-ray obscuring column density (N_H) and Eddington ratio for ten heavily reddened quasars, including eight objects from this chapter. The tracks show the effective Eddington limit for dusty material in the cases of single scattering (solid line; Fabian et al., 2009) and radiation trapping (dashed line; Ishibashi et al., 2018). All heavily reddened quasars are observed to lie to the right of these limits, where AGN are predicted to undergo a fast 'blowout' phase, and suggesting that we may expect to observe strong outflow signatures in [O III].
Credit: Lansbury et al. (2020), Fig. 6.

At the same time they show broad emission lines, proving that the obscuration is not solely due to simple orientation effects and also allowing their black hole masses to be estimated from virial methods.

Using X-ray observations from *XMM-Newton*, Lansbury et al. (2020) recently found that the heavily dust-reddened quasar population lies exclusively above the modified Eddington limit (Fig. 5.1). We therefore expect this population to present signatures of AGN-driven outflows, and to show evidence for stronger outflows when compared to unreddened objects in the same luminosity and redshift range. The aim of this chapter is to test this prediction using spectroscopic measurements to compare the ionised gas kinematics in the unobscured and heavily dust-reddened quasar populations at $L_{bol} \approx 10^{47}$ erg s^{-1} and $z > 2$. Quantifying the properties of the ionised gas emission in reddened and unobscured quasars allows us to compare the feedback mechanisms in the two populations, and simultaneously place constraints on the location of the obscuring material in the reddened quasars.

The structure of this chapter is as follows. In Section 5.2 we construct a sample of 22 heavily reddened quasars with redshifts $z > 2$ and spectral coverage of the [O III] λ5008 emission line. Our fitting procedure to derive Hα and [O III] emission line properties is described in Section 5.3. We compare the ionised gas kinematics in our heavily reddened sample with a large (> 100) sample of unobscured quasars from Coatman et al. (2019) in the same redshift and luminosity range in Section 5.4 and discuss our results in Section 5.5.

We correct for dust extinction using the quasar extinction law described in Section 3.3.6, which gives wavelength-dependent attenuations

$$A_\lambda = k(\lambda) \times E(B-V) \tag{5.1}$$

with $k(H\beta) = 3.57$, $k(5008\,\text{Å}) = 3.45$, $k(5100\,\text{Å}) = 3.38$, $k(V) = 3.10$, $k(H\alpha) = 2.53$, $k(\text{Pa}\,\gamma) = 1.41$ and $k(\text{Pa}\,\beta) = 1.17$.

5.2 SAMPLE SELECTION

Banerji et al. (2012, 2013, 2015) and Temple et al. (2019) have identified a population of 49 heavily dust-reddened quasars with extinctions $E(B-V) > 0.5$ and redshifts $2.0 < z < 2.7$. These objects were selected to be point sources in the K band and to have red colours (e.g. $(J-K)_{\text{Vega}} > 2.5$) in three near-infrared sky surveys: the UKIDSS Large Area Survey (UKIDSS-LAS; Lawrence et al., 2007), the VISTA Hemisphere Survey (VHS; McMahon et al., 2013), and the VISTA VIKING survey (Edge et al., 2013). Candidates were followed up with near-infrared spectrographs and confirmed to be quasars through the presence of broad Hα emission in the K band.

At redshifts $2.0 < z < 2.7$, [O III] and Hβ are both visible in the H band. The aim of this chapter is to quantify the kinematics of ionised gas outflows using the shape and strength of the [O III] emission, and so we select all 22 objects from the parent sample of 49 heavily reddened quasars which had H band spectra taken simultaneously with their K band discovery spectra. 16 of these objects have data from VLT-SINFONI, including 13 from Temple et al. (2019) and three from Banerji et al. (2012). A further six objects from Banerji et al. (2012) have Gemini-GNIRS data. The precise colour criteria used to select these quasars, together with the instrumental set-up, data reduction steps, and apertures used to extract 1-dimensional spectra, are described in Temple et al. (2019) and Banerji et al. (2012).

All 22 objects in this sample have spectral coverage of Hα and Hβ as well as [O III]. We can therefore use the kinematics of the Balmer emitting gas to estimate black hole masses and Eddington ratios. We model the emission from Hα, Hβ and [O III] in order to derive more robust properties for these emission lines. In order to measure line

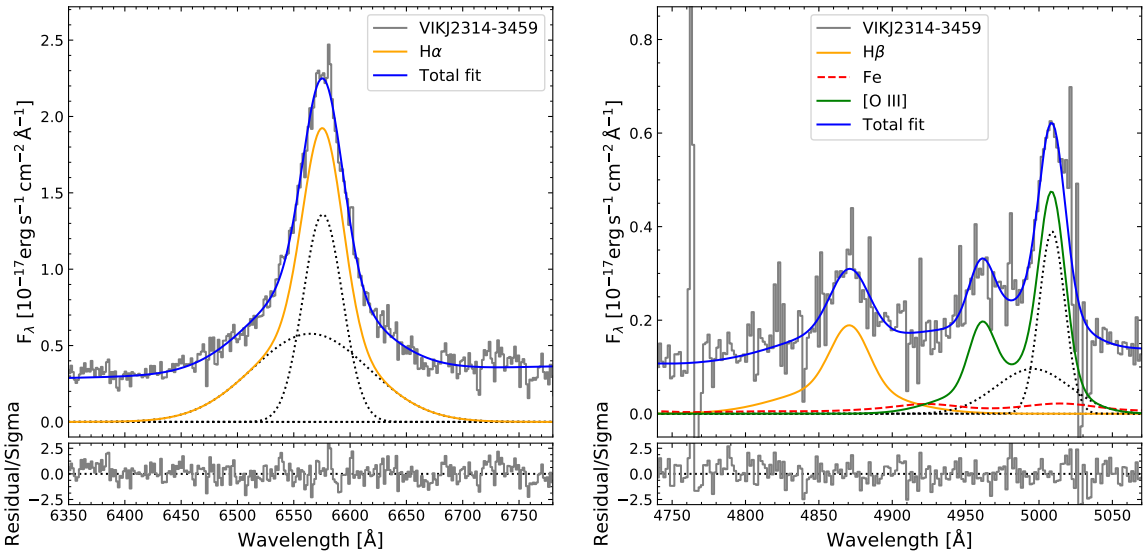

Figure 5.2: Examples of our fits to the Hα line (left) and the region around Hβ and [O III] (right). Individual Gaussian components in the fits to Hα and [O III] λ5008 are shown with dashed lines. Residuals are shown in the panels below, scaled by the noise. VIK J2314-3459 is typical of our sample of heavily reddened quasars in terms of its S/N properties, with the continuum flux being noticeably stronger at 6750 Å than at 4750 Å.

properties in a consistent manner across the whole sample, we carry out our own fits to these emission lines in the manner described below.

5.3 SPECTRAL FITTING AND BLACK HOLE MASSES

Our modelling procedure for the Hα, Hβ and [O III] emission lines is very similar to that used by Shen et al. (2011), with the main difference being that we constrain the shape of the Hβ line to be the same as that of Hα. Due to the large amount of dust extinction in these reddened quasars, the S/N is considerably higher in Hα than in Hβ and we find that we obtain better fits to the region around Hβ by constraining the shape of the emission line in this way.

5.3.1 *Hα modelling procedure*

A power-law continuum is fit to the data in the wavelength regions 6000-6350 and 6800-7000 Å, except for VIK J2238-2836, where the power-law is instead fit to the region 6800-7800 Å. This continuum is then subtracted from the spectrum and seven different models are fit to the Hα line in the window 6350-6800 Å.

We fit the continuum-subtracted Hα line with a model consisting of one, two, or three broad Gaussian components. In the case of two

Gaussians, this fit is done twice: once constraining both Gaussians to have the same centroid and once where the two components are unconstrained. For the three models with one or two broad components, a separate fit is also tried with the addition of a narrow line region (NLR) template. The NLR template consists of five Gaussians, each constrained to have the same width and velocity offset: one to fit any narrow component of Hα, and two each to fit the [N II] $\lambda\lambda$6548,6584 and [S II] $\lambda\lambda$6717,6731 doublets. The amplitudes of the [S II] doublet are constrained to be equal and those of [N II] are fixed at the expected ratio of 1 : 2.96. All components of all models are constrained to be non-negative.

Each fit is visually inspected, and models which contain physically unreasonable line widths ($\leqslant 200\,\mathrm{km\,s^{-1}}$) are rejected. A model with more free parameters is accepted in favour of a simpler model only if there is a greater than 10 per cent reduction in the χ^2 per degree of freedom in the fitting window. An example of these 'best' fits is shown in Fig. 5.2. Fits for the full sample are shown in Appendix A of Temple et al. (2019), and have a median reduced χ^2 value of 0.978. One object (VIK J2243-3504) is found to require the inclusion of the NLR template in order to best describe the shape of the Hα line profile; all the other objects are adequately described by up to three broad Gaussians.

5.3.2 *Hβ and [O III] modelling procedure*

The region outside the observed frame wavelengths 1.45-1.84 μm is first masked to exclude the portions of the spectrum which are severely affected by atmospheric absorption. The rest frame wavelength region 4435-5535 Å is then fit simultaneously with (i) a power-law, (ii) an iron template taken from Boroson and Green (1992), (iii) the profile of the best-fitting Hα model, with the normalisation free to vary to fit Hβ, and (iv) one of three models for the [O III] $\lambda\lambda$4960,5008 doublet. The iron template is first convolved with a Gaussian kernel, the width of which is allowed to vary up to the width of the profile of the best-fitting Hα model. In all objects, the resulting fits have an iron width consistent with that of the Hα emission. We show in Section 5.4.4 that our results are robust when comparing the use of different iron templates.

The [O III] λ4960 line is constrained to have the same shape as the λ5008 line, with the total flux in the lines fixed at the theoretical ratio of 1 : 2.98 (Storey and Zeippen, 2000). We try fitting zero, one, and two Gaussians to the λ5008 line, with an extra Gaussian accepted only if it leads to a greater than 10 per cent reduction in the χ^2 per degree of freedom in the wavelength range 4700-5100 Å. A fourth [O III] model with a third Gaussian component is found not to lead to a significant reduction in reduced χ^2 in any of the objects in this sample.

The λ4960 and λ5008 lines are fit simultaneously, although we only use the λ5008 line properties when presenting our results. Eleven objects are adequately fit with a single Gaussian describing the λ5008 line. Eight objects require a second Gaussian component to fully reproduce the λ5008 line profile, providing evidence for an asymmetric line profile in ≈ 42 per cent of the population, similar to the fraction found in unobscured quasars by Coatman et al. (2019). An example of these fits is shown in Fig. 5.2. Fits for the full sample are shown in Appendix A of Temple et al. (2019) and have a median reduced χ^2 value of 1.113 across the wavelength range 4700-5100 Å.

Three objects are found to be consistent with no [O III] emission. We do not make any estimate of the velocity width of the [O III] lines in these cases. In ULAS J1216-0313 and ULAS J1234+0907, we estimate an upper limit on the equivalent width of the [O III] emission line by fitting a template, generated by running our fitting routine over a median composite spectrum constructed from the 19 objects in our sample with reliable [O III] measurements. In one object, ULAS J0144-0014, we find no [O III] emission, even when constraining the shape of the line with the template.

5.3.3 *Black hole masses*

For intrinsically luminous, heavily reddened quasars at $z > 2$, it is known that host galaxy contamination does not significantly affect the JHK colours (Wethers et al., 2018). We therefore derive extinctions using the near-infrared photometric data from VISTA and UKIDSS. Where J-band photometry is available, we find the $E(B-V)$ required to best fit the observed $J-K$ colour when reddening our quasar model (Chapter 3). If J-band photometry is not available, we use the $H-K$ colour instead. Rest frame 5100 Å luminosities are corrected for dust extinction using this $E(B-V)$. We derive black hole masses using the prescription from Vestergaard and Peterson (2006), and use the correction from Coatman et al. (2017) to estimate the FWHM of Hβ from our fit to Hα:

$$\mathrm{FWHM(H\beta)} = 1.23 \times 10^3 \left(\frac{\mathrm{FWHM(H\alpha)}}{10^3\,\mathrm{km\,s^{-1}}} \right)^{0.97} \tag{5.2}$$

$$\mathrm{M_{BH}} = 10^{6.91} \left(\frac{\mathrm{L_{5100}}}{10^{44}\,\mathrm{erg\,s^{-1}}} \right)^{0.5} \left(\frac{\mathrm{FWHM(H\beta)}}{10^3\,\mathrm{km\,s^{-1}}} \right)^{2} \mathrm{M_\odot} \tag{5.3}$$

Eddington ratios are estimated assuming $L_{bol} = 8 \times L_{5100}$, and are given in Table 5.1, alongside the derived extinctions, dust-corrected luminosities and black hole masses.

We find extinctions in the range $0.5 < E(B-V) < 2.0$, as expected from the photometric selection criteria. For brighter objects

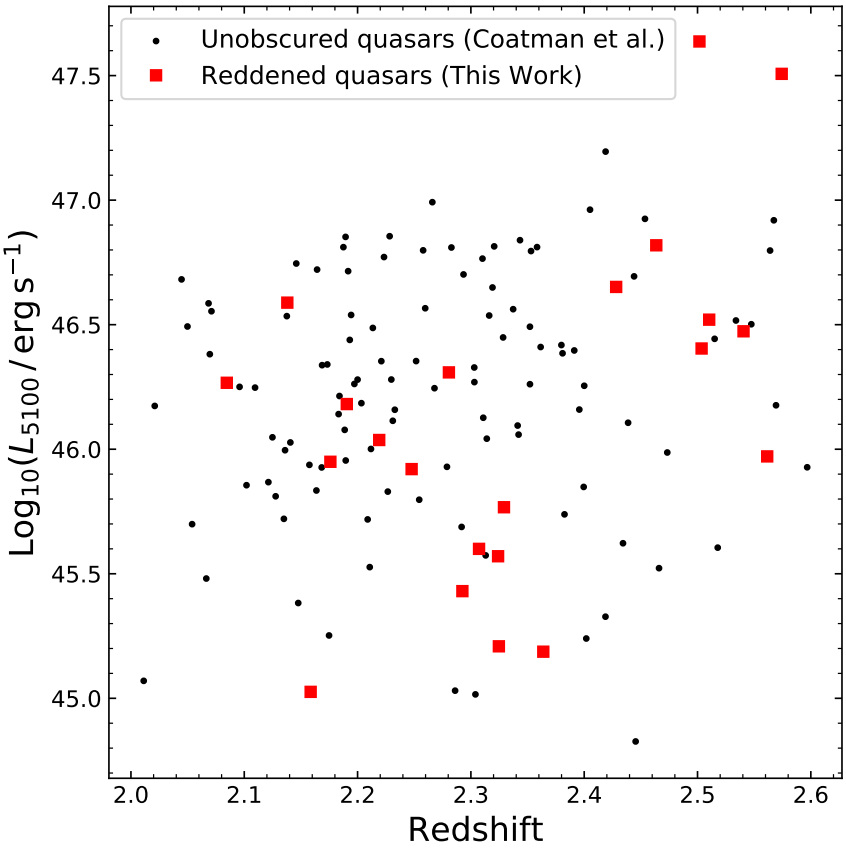

Figure 5.3: The distribution in redshift-luminosity space of our heavily reddened quasar sample and our comparison sample of 111 unobscured objects. Luminosities have been corrected for dust extinction, and have a typical uncertainty of 0.2 dex.

from UKIDSS-LAS and VHS, we find black hole masses in the range $10^{9.2-10.5}\,\mathrm{M}_{\odot}$, placing them among the most massive black holes known at these redshifts (e.g. Bischetti et al., 2017). For fainter objects selected from the deeper VIKING survey, we find smaller black hole masses in the range $10^{8.4-9.4}\,\mathrm{M}_{\odot}$. These quasars are intrinsically fainter than heavily reddened quasars selected from wider, shallower surveys and do not simply appear fainter due to increased extinction.

5.4 EMISSION LINE PROPERTIES

In this section we explore the [O III] λ5008 emission line properties in our sample of heavily reddened quasars. We use the best-fitting [O III] model as described in Section 5.3.2 to measure the shape and equivalent width of the line. For those objects which require multiple Gaussian components to best model the emission line, we do not ascribe any significance to individual components, but instead derive properties for the total line profile.

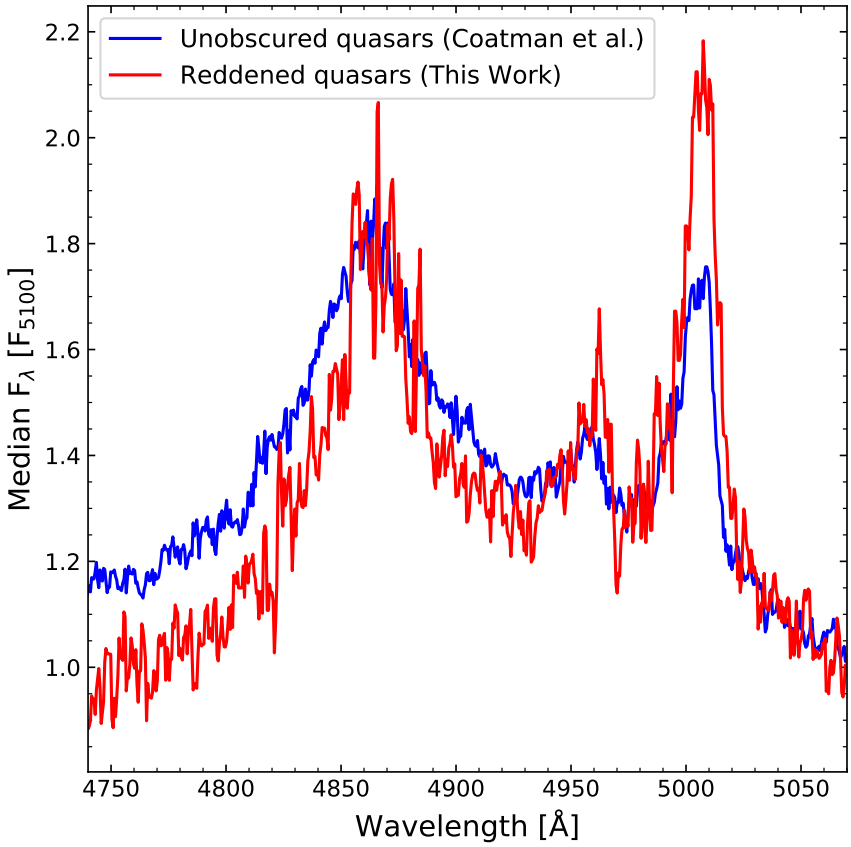

Figure 5.4: Composite spectra of 22 heavily reddened quasars and a matched sample of 22 unobscured quasars which are the nearest neighbours in $L_{5100} - z$ space. Fluxes have been normalised at 5100 Å in both samples, with no correction for dust extinction in the reddened sample.

We compare our heavily reddened quasars to a large sample of unobscured quasars in the same redshift and luminosity range. This comparison sample contains 111 quasars with $2.0 < z < 2.6$ and near-infrared spectra taken from the catalogue of Coatman et al. (2017) and Coatman et al. (2019, see Fig. 5.3), which are flagged in the catalogue as having robust measurements of the [O III] emission line properties. The selection of quasars in the Coatman et al. catalogue is described in detail by Coatman et al. (2017). In the context of this work, the comparison sample essentially provides an unbiased representation of the optical SEDs of unobscured quasars, matched in redshift and luminosity to our reddened quasar sample. We note that both our sample and the comparison sample consist of the most massive, most highly accreting black holes at these redshifts. Matching in luminosity therefore has the effect of also matching in black hole mass and accretion rate, at least within the usual uncertainties on black hole mass estimation. We also note that using a larger comparison sample taken from the full catalogue redshift range of $1.5 < z < 4.0$ does not alter any of the results in our subsequent analysis.

To help visualise the quality of data in the two samples, in Fig. 5.4 we show stacks of our spectra in the region around the [O III] emission line, normalised at 5100 Å. For the purposes of this stack only, we take a subsample of 22 objects from our comparison sample which are the nearest neighbours to each of our 22 reddened quasars in the redshift-luminosity space shown in Fig. 5.3. We apply no correction for dust obscuration before stacking, and the slope of the continuum across the narrow wavelength range shown is clearly redder in the reddened sample. Comparing the two stacks, it can be seen that (a) the reddened objects generally have lower S/N in this part of the spectrum, (b) the two samples have very similar [O III] line widths, and (c) the [O III] emission in the reddened sample is perhaps slightly stronger relative to the continuum. We will explore the shapes and strengths of the [O III] lines in our two samples further in Sections 5.4.1, 5.4.2 and 5.4.3.

Uncertainties on derived parameters are estimated using a Monte Carlo approach. One hundred realisations of each spectrum are generated by smoothing the observed quasar spectrum with a 5-pixel inverse-variance weighted top-hat filter, and then adding 'noise' drawn from a Gaussian distribution with dispersion equal to the spectrum flux uncertainty at each wavelength. Quoted parameter uncertainties are 1.48 times the median absolute deviation of the parameter distribution in the ensemble of simulations.

We compare the samples using the two-sample Kolmogorov-Smirnov (KS) test (Peacock, 1983), which tests the null hypothesis that two samples are drawn from the same underlying probability distribution (i.e., the same population). We also use the two-sample Anderson-Darling (AD) test (Anderson and Darling, 1952; Darling, 1957), which

tests the same null hypothesis, but is more sensitive to differences in the tails of the distributions.

We begin by comparing the strengths of the broad Hα emission in our samples, as measured by the equivalent width. Our heavily reddened quasars were selected by virtue of their red colours, leading to a selection bias towards objects which are bright in the K-band, i.e. those objects which might have stronger Hα emission in the redshift range $2.0 < z < 2.6$. As shown in Fig. 5.5, we find no systematic difference in the equivalent width of the broad line emission between the two samples, suggesting that the amount of ionised gas is not significantly different in the reddened and unobscured samples.

We note that, if one adopts a theoretical value for the unreddened Hα to Hβ ratio, the observed ratio can be used to estimate the extinction in front of the broad line emitting region. However, in addition to the statistical uncertainty of ~ 0.1 magnitudes arising from the low S/N in the Hβ lines of our heavily reddened quasars, further uncertainty arises due to the unknown temperatures and densities of the gas producing the Balmer emission, i.e. the assumption of a fixed intrinsic flux ratio (Korista and Goad, 2004). Adopting an intrinsic ratio of $\mathrm{H}\,\alpha : \mathrm{H}\,\beta = 2.86 : 1$ (Dopita and Sutherland, 2003), we find that the extinctions estimated in this way are consistent with the $E(B-V)$s we derive from photometry in Section 5.3. However, at a fixed value of the $E(B-V)$ derived from photometry, the scatter in the extinction we measure from the Balmer lines is ~ 0.5 magnitudes. We therefore use $E(B-V)$s from photometry in the rest of this chapter.

5.4.1 *The shape of the [O III] lines*

As described in Section 5.3.2, we have information about the shape of the [O III] lines in 19 of our 22 heavily reddened quasars. For these 19 objects, we first calculate the 80 per cent velocity width (w_{80}) of the λ5008 line profile. We take the best-fitting [O III] model and integrate to find the total flux under the line profile. The velocity width is then defined to be $w_{80} = v_{90} - v_{10}$, where v_{90} and v_{10} are the respective velocities at which 90 and 10 per cent of the cumulative flux in the line profile is found. We correct for instrumental broadening of $\sigma = 200\,\mathrm{km\,s^{-1}}$, noting that all of our [O III] lines are well resolved with the smallest velocity width in our sample being $w_{80,\mathrm{min}} = 600\,\mathrm{km\,s^{-1}}$ prior to applying the correction.

The [O III] velocity widths in our reddened sample and in the comparison sample of unobscured quasars are shown in Fig. 5.6. We find a weak correlation between w_{80} and continuum luminosity, as is also found in unobscured quasars at the same redshifts and luminosities (e.g. Coatman et al., 2019; Netzer et al., 2004; Shen, 2016). There is no such correlation between w_{80} and either the black hole mass, the Eddington ratio or the $E(B-V)$. Using the KS and AD

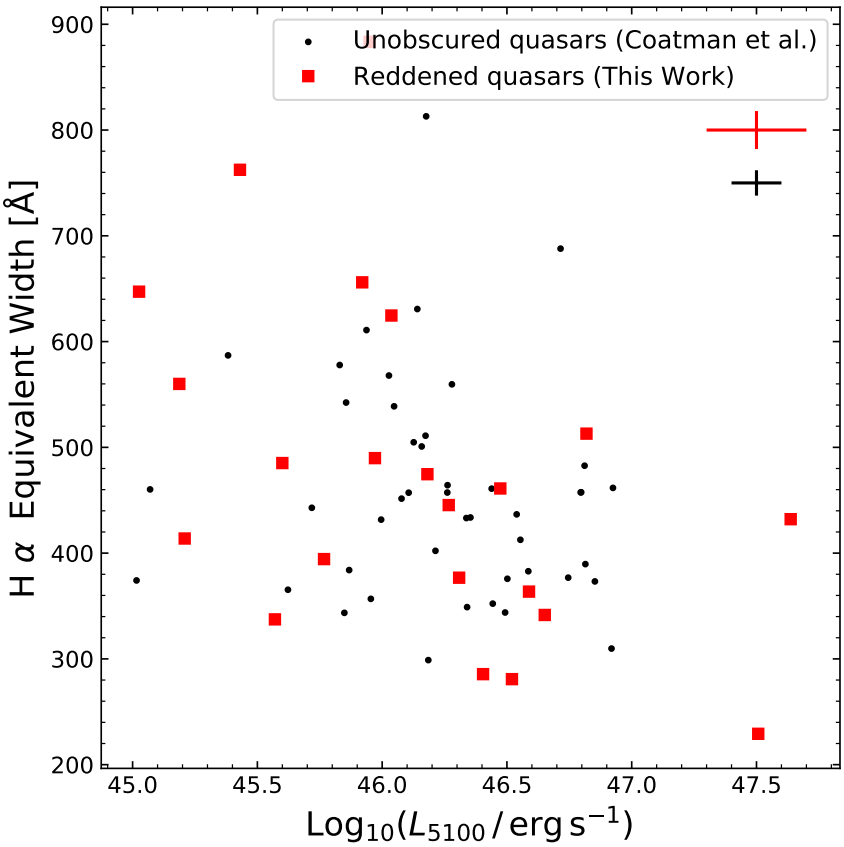

Figure 5.5: The broad Hα emission line equivalent widths in our reddened quasar sample and in the 47/111 objects from our comparison sample with spectral coverage of Hα, plotted against the dust-corrected 5100 Å luminosity. Typical uncertainties are shown in the top right. Using KS and AD tests, we find no significant difference between the Hα EWs in the two populations.

tests, we find no evidence to reject the null hypothesis that the two samples are drawn from the same underlying distribution of velocity widths. As the velocity widths in both samples are significantly larger than the velocity dispersion expected from virialised gas motions, it is reasonable to assume that most, it not all, of our velocity width measurements are dominated by emission from outflowing gas. Our results therefore suggest that the ionised gas outflows in the host galaxies of our reddened quasars are, on average, no faster or slower than those in the unobscured population.

In Section 5.3.2, we found that around 42 per cent of the quasars in both the reddened and unobscured samples show evidence for asymmetric [O III] emission, in that they are not adequately described by a single Gaussian line profile, and require a second Gaussian component in the fit to [O III]. For these objects, we quantify the asymmetry of the λ5008 line using $(v_{90} - v_{50})/(v_{50} - v_{10})$, and find no significant difference between the two samples in terms of the distribution of the amount of λ5008 line asymmetry.

5.4.2 *The equivalent width of the [O III] lines*

Due to the uncertainty in the location and physical scale of the [O III] emitting material and also the uncertainty in the location of the obscuring dust in heavily reddened quasars, the amount by which the [O III] emission in our sample is attenuated is unknown. We can assume that the [O III] attenuation is at least zero, but no more than the attenuation of the continuum: the obscuring dust might be located entirely in front of the [O III] emitting region, or behind the [O III] emitting region but in front of the continuum source. This unknown factor in the geometry of these objects leads to an uncertainty when deriving any measure of the intrinsic strength of the [O III] emission.

With this uncertainty in mind, we derive the equivalent width (EW) of the [O III] λ5008 line under two different assumptions: that the emission line is reddened by the same amount as the continuum, and that the continuum is reddened but that the emission line itself is completely unobscured. The first case will produce the largest possible EW, and the second will give the smallest possible EW, as de-reddening the continuum while leaving the emission line unchanged increases the flux in the continuum and hence lowers the EW. Any amount of 'intermediate' de-reddening of the [O III] emission will produce an EW somewhere between these two extremes.

In both cases, the cumulative distribution function (CDF) of the [O III] EWs in our sample is formed and shown in Fig. 5.7. For the case where the [O III] emission is unobscured and so does not need to be corrected for extinction, we find that we can reject the null hypothesis with $p < 0.001$, meaning that such a distribution of [O III]

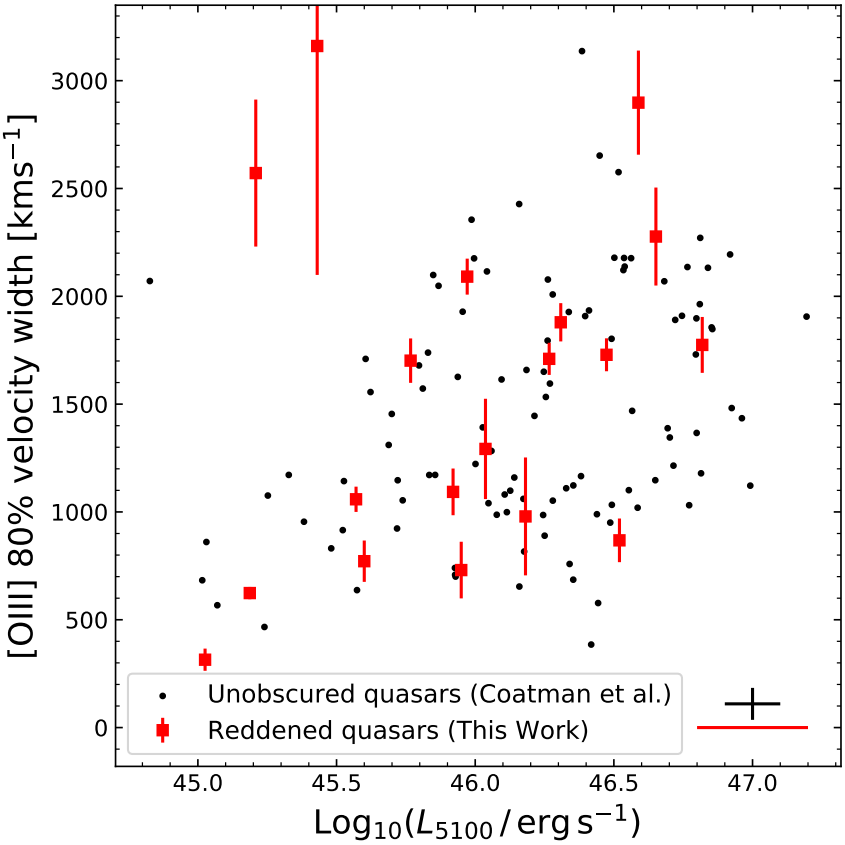

Figure 5.6: The [O III] 80 per cent velocity widths in our reddened sample and our comparison sample, plotted against the dust-corrected monochromatic 5100 Å luminosity. Typical uncertainties are shown in the bottom right. Using KS and AD tests, we find no significant difference between the [O III] velocity widths in the two populations.

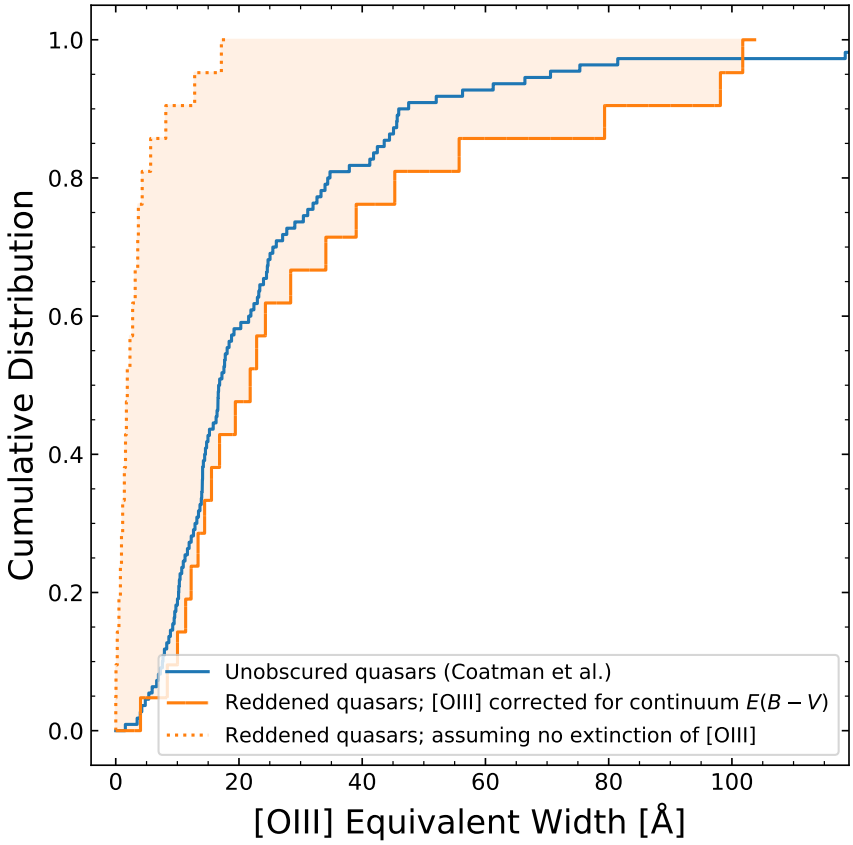

Figure 5.7: The [O III] EW distribution for our reddened quasars. When the continuum is corrected for extinction but the emission line is assumed to be completely unobscured (dotted orange), the [O III] EW distribution is not consistent with that of the comparison sample (shown in blue). However, the [O III] EWs in our reddened sample are consistent with having been drawn from the same distribution as that of the unobscured sample, if we assume that the emission line is subject to the same amount of extinction as the continuum (solid orange), suggesting that the obscuring dust is located outside the [O III] emitting region.

EWs is inconsistent with having been drawn from the same population as the unobscured quasars in Coatman et al. (2019).

However, we are unable to reject the null hypothesis ($p > 0.3$) in the case that the obscuring dust is located completely in front of the [O III] emitting gas, meaning that our results are consistent with a scenario in which the intrinsic distribution of [O III] EWs in our reddened sample is the same as that of the unobscured population, and where the amount of obscuration in our objects along the line of sight towards the [O III] emitting gas is is the same as the amount of obscuration along the line of sight to the continuum source.

5.4.3 *Degeneracy between the amount of ionised gas and the location of the reddening dust*

When deriving any measure of the strength of the [O III] emission line, such as the equivalent width, there is a degeneracy between the intrinsic amount of line emission and the amount of obscuration along the line of sight towards the emitting material. The measured equivalent width of the emission line will always depend on both of these factors. For the heavily dust-reddened objects presented in this chapter, we have no independent constraints on the location of the obscuring material - more specifically, the dust could lie inside or outside the [O III] emitting region, or could be co-located with it. Due to this degeneracy, we must make an assumption in order to draw any further conclusion about the relative strength of the ionised gas emission in reddened quasars compared to the unobscured population in the same redshift and luminosity range.

As the velocity widths of the [O III] lines, the continuum luminosities, and the Hα equivalent widths in our sample are consistent with having been drawn from the same distributions as those of the unobscured population, it is reasonable to assume that the amount of ionised gas in our reddened quasars is the same as in the unobscured population and so the intrinsic [O III] emission is not significantly stronger or weaker in the reddened population.

If we make this assumption, i.e. that there is no difference in the distribution of the amount of ionised gas in the two populations and hence that the two populations have the same intrinsic [O III] EW distribution, then we can fit the observed CDF of our reddened sample to that of the unobscured population, as shown in Fig. 5.8. We find that the amount of extinction required on average in the [O III] lines of our reddened objects to best fit the EW distribution is 0.92 times the $E(B-V)$ derived from the near-infrared photometry in Section 5.3.3: on average, just 8 per cent of the continuum extinction arises inside the [O III] emitting region. However, it is worth reemphasising the result in Section 5.4.2, in that, under the assumption that the two populations have the same [O III] EW distribution, our reddened

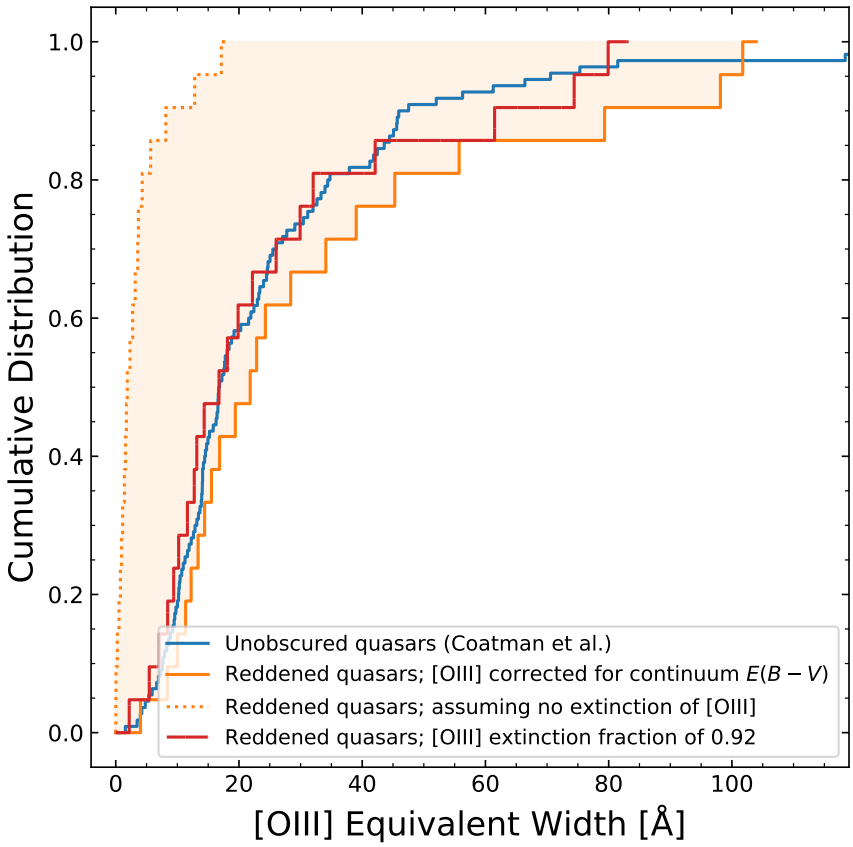

Figure 5.8: As Fig. 5.7, with (in red) the CDF when we assume that the intrinsic distribution of [O III] EWs is the same in both the reddened and unobscured samples, and vary the amount of reddening required in the [O III] emission line to match the CDF of the unobscured sample. We find the best-fitting [O III] extinction to be 92 per cent that of the continuum $E(B-V)$.

quasars are not inconsistent with having the obscuring material located entirely outside the [O III] emitting region.

We note that the two most luminous quasars in our reddened sample (ULAS J1216-0313 and ULAS J1234+0907) are the two most heavily reddened objects and also have very weak [O III] emission. Even if we correct the observed [O III] for the largest possible extinction, the EWs in these two objects are still less than half the median EW in the rest of the reddened sample, suggesting that the weakness of the observed [O III] emission in these objects cannot be explained purely by obscuration, and that the [O III] emission is intrinsically weak in these objects. This result is very similar to the fraction (~ 10 per cent) of unobscured quasars at these luminosities and redshifts which have very weak [O III] emission (i.e. EW< 1Å; Coatman et al., 2019), and we suggest that it is consistent with a scenario in which the most luminous quasars show weaker emission from the narrow line region (Netzer et al., 2004), either by overionising or by physically removing the emitting gas.

5.4.4 *Effect of Iron subtraction*

We test the sensitivity of our results to the assumed shape of the iron template by replacing the iron template of Boroson and Green (1992, BG92) with that of Kovačević, Popović and Dimitrijević (2010, KPD10) and re-deriving the [O III] line properties with an otherwise identical line fitting routine. The iron prescription of KPD10 is much more flexible, in that it allows the ratios of different groups of iron lines to vary, corresponding to an increase in the number of free parameters in the fit and enabling a more accurate description of the iron in objects where iron line ratios are different from I Zw 1, the NLS1 galaxy used to derive the template of BG92.

We compare the main results of this chapter under the two different iron prescriptions, as shown in Fig. 5.9. We visually inspect individual objects, such as VHS J1117-1528, which has $w_{80} = 2330, 3130\,\mathrm{km\,s^{-1}}$ and EW $= 22.7, 33.8$ Å when fit with BG92 and KPD10 respectively, making this the object from our sample with the biggest difference in the derived [O III] velocity widths. The fit in this quasar (Fig. 5.10) is sensitive to the form of the iron prescription due to the fact that the [O III] emission line is both broad ($w_{80} > 2000\,\mathrm{km\,s^{-1}}$) and weak (EW < 35 Å).

However, the population statistics in our sample do not change significantly when using a different iron prescription to fit our data; in particular, the results described in Section 5.4 are the same when derived with either prescription. Therefore, while we are cautious about the iron contribution in individual objects, we are confident that the precise form of the iron template used does not affect the conclusions of this chapter.

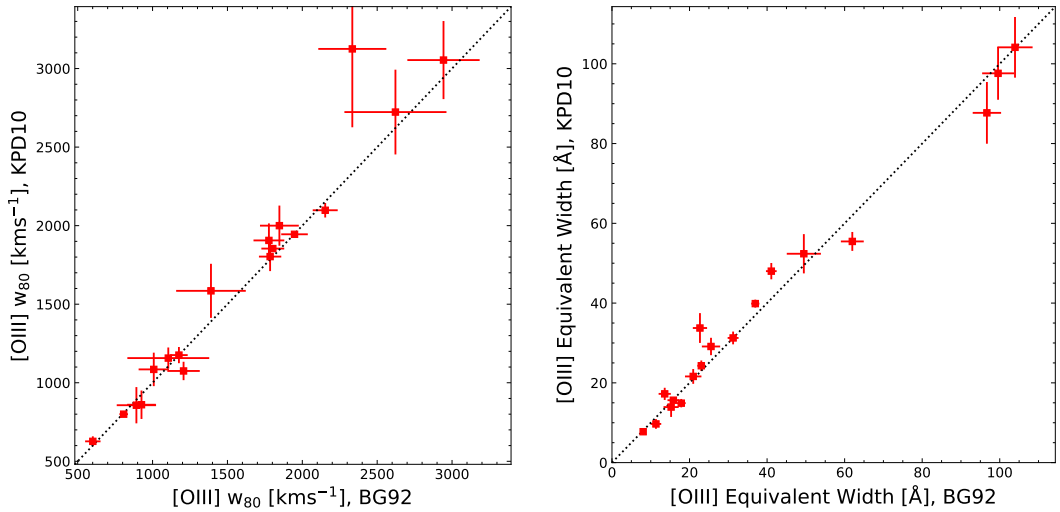

Figure 5.9: The [O III] 80 per cent velocity widths and equivalent widths for our sample of dust-reddened quasars, derived using the optical iron templates from Boroson and Green (1992, BG92) and Kovačević, Popović and Dimitrijević (2010, KPD10). VIK J2232-2844 is not well-fit by the KPD10 iron template and so is excluded. All other aspects of the fitting routine are the same for both templates, and are as described in the main text. The dashed line is the 1:1 relation, and we find the two iron prescriptions give very similar results when considering the distributions of [O III] line properties across the whole sample.

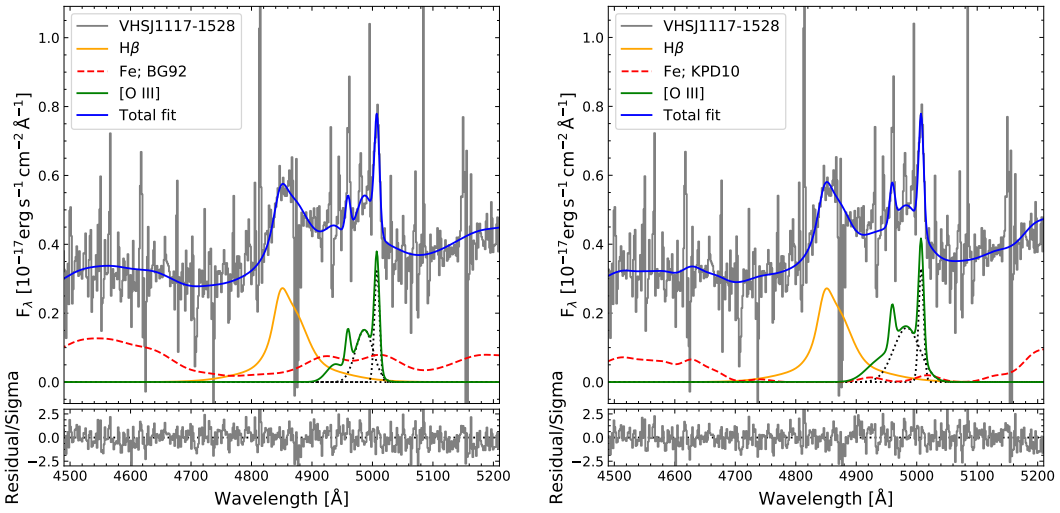

Figure 5.10: The Hβ - [O III] region in VHS J1117-1528, fit using the iron prescriptions from Boroson and Green (1992, BG92) and Kovačević, Popović and Dimitrijević (2010, KPD10). For individual quasars, the derived line properties are sensitive to the form of the iron prescription used to model the data when the [O III] emission line is both broad ($w_{80} > 2000\,\mathrm{km\,s^{-1}}$) and weak (EW < 35 Å).

5.5 DISCUSSION

5.5.1 *Comparison to the literature*

Wu et al. (2018) report the detection of [O III] in W1136+4236, a *WISE*-selected Hot Dust-Obscured Galaxy (HotDOG). W1136+4263 is at $z = 2.41$, with a dust-corrected luminosity of $L_{5100} \approx 10^{46.5}\,\mathrm{erg\,s^{-1}}$ and an extinction of $E(B-V) = 2.5$: while it is more reddened than the reddened quasars in our sample, it lies in the same luminosity and redshift range. We note that this HotDOG has an [O III] velocity width of $w_{80} \approx 2500\,\mathrm{km\,s^{-1}}$, placing it within the range spanned by our data in Fig. 5.6. It is hard to draw conclusions from this single object, which is the least obscured HotDOG studied by Wu et al., but there is currently no evidence to suggest that the ionised gas kinematics in HotDOGs are any more extreme than those in our heavily reddened quasar population. Similarly, the red quasars presented by Urrutia et al. (2012) with $L_{bol} \approx 10^{46}\,\mathrm{erg\,s^{-1}}$ show [O III] emission with the width of the broad component up to $1600\,\mathrm{km\,s^{-1}}$ (Brusa et al., 2015), which coincides with the area of parameter space populated by our heavily reddened quasars.

Comparing to type 2 quasars, we note that the ionised gas kinematics in our reddened quasars are similar to the [O III] velocity widths in the sample of type 2 quasars at $z < 0.8$ studied by Zakamska and Greene (2014), who find $w_{80} = 280 - 3000\,\mathrm{km\,s^{-1}}$. These quasars have $L_{[O\,III]} = 10^{42-43.5}\,\mathrm{erg\,s^{-1}}$. However, the broad line and continuum emitting regions in these objects are obscured by dust on nuclear scales which is unlikely to be obscuring the [O III] emitting region, and so it is hard to directly compare the luminosities of these quasars with the objects in our sample.

Our results complement those of Harrison et al. (2016), who examined the [O III] properties of an X-ray selected sample of optically unobscured AGN at $1.1 < z < 1.7$. The AGN in their sample have [O III] w_{80} in the range $200 - 1000\,\mathrm{km\,s^{-1}}$, $L_{[O\,III]} \approx 10^{42}\,\mathrm{erg\,s^{-1}}$ and $L_X \approx 10^{44}\,\mathrm{erg\,s^{-1}}$. They are therefore around an order of magnitude fainter than our heavily reddened quasars (Lansbury et al., 2020) and also appear to have narrower [O III] line profiles in comparison to our quasars. Harrison et al. (2016) found no significant difference between the ionised gas kinematics in X-ray obscured and X-ray unobscured objects. Taken with our results, this supports a scenario where the most powerful ionised gas outflows in massive galaxies are driven by the luminosity of the central quasar, independently of the column density of any obscuring material along the line of sight to the observer.

By contrast, DiPompeo et al. (2018) do find a difference in the [O III] properties of red and blue colour-selected AGN, with the redder AGN having broader, more blueshifted [O III] emission on average. However, the DiPompeo et al. AGN are significantly less luminous and

at much lower redshifts than the heavily reddened quasars we consider. The two results are therefore not inconsistent and could indicate different redshift evolution in the outflow properties of reddened and unobscured AGN.

We note that the heavily reddened quasars in our sample do not show the same extreme [O III] kinematics as the four rare (i.e. out of 97 ERQs; Hamann et al. 2017) objects presented in Zakamska et al. (2016), which are in the same luminosity and redshift range as our heavily reddened quasars. Similar results have also been reported for the same population by Perrotta et al. (2019). However, the Zakamska et al. quasars were also selected to have high equivalent width C IV emission, and it is conceivable that the extreme [O III] kinematics seen in that sample could be linked to this selection (Villar Martín et al., 2020). Alternatively, Coatman et al. (2019) find similarly rare (18/354) unobscured quasars with ionised gas kinematics that are almost as extreme, and so it could be that $\lesssim 5$ per cent of the most luminous quasars at $z > 2$ have ionised gas outflows of up to $5000\,\mathrm{km\,s^{-1}}$, irrespective of reddening, and that if we were to increase our sample of luminous heavily dust-reddened quasars by a factor of ~ 5 we might also observe such extreme outflows.

5.5.2 *Ionised gas kinematics*

In Section 5.4.1, we found no significant difference between the kinematics of the [O III] emitting gas in the heavily reddened and unobscured quasar populations at $z > 2$, as traced by either the velocity width or the asymmetry of the [O III] line profile, although we do note that there would need to be a large dissimilarity between the two populations in order to find a statistically significant difference between our samples, due to the small sample sizes. Thus, while the kinematics of the [O III] emission are not observed to be significantly different, we cannot rule out the possibility of smaller differences in the ionised gas emission properties of unobscured and heavily reddened quasars. We also show that the [O III] velocity width tends to increase with increasing AGN luminosity in both populations, a trend that has also been seen in lower redshift AGN (Harrison et al., 2016; Zakamska and Greene, 2014).

If the objects in our reddened sample do indeed represent the 'blowout' phase for luminous quasars at redshifts $z \approx 2$, then, as the signatures of fast outflows are also seen in the unobscured population at the same redshift, our results suggest that the outflowing gas persists after the obscuring dust has been cleared from the line of sight (similar to the model of Zubovas and Nardini, 2020). In particular, the asymmetries and large velocity widths seen in the [O III] emission in our comparison sample of unobscured quasars would be due to outflows which have already cleared any obscuring material

away from the line of sight to the continuum source. The 'blowout' predicted to be driven by radiation pressure on dusty gas is expected to be relatively short lived ($\sim 10^5$ yr) for heavily reddened quasars (Lansbury et al., 2020), and so it is not unreasonable to expect ionised gas outflows moving at 'only' $\sim 10^3\,\mathrm{km\,s^{-1}}$ to persist on kilo-parsec scales in the host galaxies of luminous quasars for longer than this time.

It takes 10^6 yr to move 1 kpc at 10^3 km s^{-1}

5.5.3 *Obscuring dust*

In Sections 5.4.2 and 5.4.3, we found that the obscuring dust in our sample of heavily reddened quasars was most likely to be located almost entirely outside the [O III] emitting region, suggesting that the obscuration in heavily reddened quasars arises on kilo-parsec scales. Using data from ALMA, Banerji et al. (2018) find large (i.e. galaxy scale) dust emitting regions in at least some heavily reddened quasars, consistent with this result. Deeper observations providing spatially resolved information about either the location of the dust or the location of the ionised gas are necessary to place firmer constraints on the physical scales and covering factor of the dust relative to the ionised gas in our sample.

We note that our results could be interpreted with a model whereby our reddened quasars are in fact unobscured quasars which are viewed along a line-of-sight that is skimming the plane of the host galaxy. However, we disfavour such a model as it would (a) require a significant disc component to the host galaxy, which would not be consistent with a merger-driven AGN triggering event, and (b) require the [O III] emitting gas to be located very close in to the centre of the galaxy, in contrast with local AGN.

5.6 SUMMARY

We have constructed a sample of 22 heavily reddened quasars with extinctions $0.5 < E(B-V) < 2.0$, luminosities $10^{45} < L_{5100} < 10^{48}\,\mathrm{erg\,s^{-1}}$, redshifts $2.0 < z < 2.6$, and spectra covering the Hα, Hβ, and [O III] emission lines. Using the [O III] line, we derive parameters describing the ionised gas kinematics and compare to a large sample of 111 unobscured quasars in the same redshift and luminosity range. Our main results are as follows:

- There is no significant difference between the two populations in the velocity widths or asymmetries of their [O III] lines, suggesting that ionised gas outflows are moving, on average, no faster or slower in the reddened population than in the unobscured population.

- As our samples are drawn from the same luminosity and redshift range, this suggests that the outflow driving mechanisms are not significantly different in the reddened and unobscured populations.
- The [O III] equivalent width distributions in the two populations are consistent with a scenario in which the reddened quasars have the same strength of ionised gas emission as the unobscured quasars, and the [O III] emission in the reddened objects is subject to the same amount of extinction as the continuum. In other words, the obscuring dust is most probably located outside the [O III] emitting region on kilo-parsec scale distances from the central SMBH.

We suggest that our results are best explained by a model in which, following a starburst episode, quasar-driven ionised gas outflows persist for some time after any obscuring dust has been cleared from the line of sight. Such an episode of star formation would most likely be triggered by a major galaxy merger, which would also provide fuel for black hole accretion and hence the trigger for quasar activity.

Name	Redshift	$E(B-V)$ [magnitudes]	$Log_{10}(M_{BH})$ [$M_\odot$]	$Log_{10}(L_{5100})$ [$erg\,s^{-1}$]	L/L_{Edd}	EW(Hα) [Å]	$Log_{10}(L_{[O\,III]})$ [$erg\,s^{-1}$]	[O III] w_{80} [$km\,s^{-1}$]
ULAS J0016-0038	2.176	0.55	9.20	45.95	0.36	883	43.22±0.07	730±131
ULAS J0041-0021	2.510	0.81	9.52	46.52	0.64	281	43.18±0.06	868±101
ULAS J0141+0101	2.562	0.58	9.43	45.97	0.22	490	43.79±0.05	2091±83
ULAS J0144-0014	2.504	0.68	9.58	46.40	0.42	286	-	-
ULAS J0144+0036	2.281	0.74	9.65	46.31	0.29	377	43.31±0.06	1880±89
ULAS J0221-0019	2.248	0.58	8.86	45.92	0.73	656	43.24±0.06	1093±108
VHS J1117-1528	2.428	1.25	9.52	46.65	0.87	342	43.16±0.06	2277±227
VHS J1122-1919	2.464	1.09	9.24	46.82	2.39	513	43.81±0.05	1775±130
ULAS J1216-0313	2.574	1.62	10.07	47.51	1.73	229	< 42.60*	-
ULAS J1234+0907	2.502	1.94	10.48	47.64	0.91	432	< 42.20*	-
VHS J1301-1624	2.138	1.24	9.40	46.59	0.99	364	43.41±0.06	2898±241
ULAS J2200+0056	2.541	0.55	9.10	46.47	1.49	461	44.15±0.05	1729±76
VIK J2205-3132	2.307	0.58	8.79	45.60	0.41	485	42.71±0.07	772±96
ULAS J2224-0015	2.219	0.61	8.98	46.04	0.73	624	43.20±0.07	1292±233
VIK J2228-3205	2.364	0.57	8.48	45.19	0.32	560	43.24±0.05	624±28
VIK J2232-2844	2.292	0.65	9.02	45.43	0.16	762	42.47±0.09	3161±1062
VIK J2243-3504	2.085	1.05	8.99	46.27	1.21	445	43.68±0.05	1710±75
VIK J2256-3114	2.329	0.69	9.16	45.77	0.26	394	43.18±0.05	1702±103
VIK J2309-3433	2.159	0.52	9.39	45.03	0.03	647	42.54±0.06	315±51
VIK J2314-3459	2.325	0.53	8.41	45.21	0.40	414	43.32±0.05	2572±341
VIK J2323-3222	2.191	0.99	9.09	46.18	0.79	475	42.98±0.06	979±273
VIK J2350-3019	2.324	0.58	8.58	45.57	0.62	337	43.03±0.05	1059±59

Table 5.1: Derived properties for the 22 heavily reddened quasars with coverage of Hα, Hβ, and [O III]. Redshifts are taken from the broad component of the fit to the Hα line. The $E(B-V)$ is estimated from the near-infrared photometry, and has an uncertainty of ~ 0.15 magnitudes. Rest frame 5100 Å luminosities have been corrected for dust extinction using the $E(B-V)$, giving rise to an uncertainty of ~ 0.2 dex. Black hole masses are derived using the prescription from Vestergaard and Peterson (2006), and have an uncertainty of ~ 0.4 dex. Eddington ratios are estimated assuming $L = 8 \times L_{5100}$, and have an associated uncertainty of a factor of 4. Hα equivalent widths are given in the rest frame. [O III] λ5008 line luminosities are given in the observed frame with no correction for extinction. 80 per cent velocity widths have been corrected for instrumental broadening of $\sigma = 200\,km\,s^{-1}$.
*Indicates that object is consistent with having no [O III] emission, and an upper bound on the line luminosity has been estimated from a template fit.

6

SUMMARY AND FUTURE PROSPECTS

6.1 SUMMARY

6.1.1 *Fe III in quasars*

Recent improvements to atomic energy-level data now allow accurate predictions to be made for the Fe III line emission strengths in the spectra of luminous quasars. The Fe III emitting gas must be primarily photoionised, consistent with observations of line reverberation. We have used CLOUDY models exploring a wide range of parameter space, together with ≃26,000 rest frame ultraviolet spectra from SDSS, to constrain the physical conditions of the line emitting gas. The observed Fe III emission is best accounted for by dense ($n_H \simeq 10^{14}\,cm^{-3}$) gas which is microturbulent, leading to smaller line optical depths and fluorescent excitation. Such high density gas appears to be present in the central regions of the majority of luminous quasars from SDSS, and the strength of emission from this gas is observed to correlate with the C IV emission line blueshift. Using our favoured model, we have presented theoretical predictions for the relative strengths of the Fe III UV34 λλ1895,1914,1926 multiplet. This multiplet is blended with the Si III] λ1892 and C III] λ1909 emission lines and an accurate subtraction of UV34 is essential when using these lines to infer information about the physics of the broad line region in quasars.

6.1.2 *Modelling quasar colours*

We have constructed a parametric SED model which is capable of reproducing the median SDSS, UKIDSS and WISE colours of tens of thousands of quasars at redshifts $0.1 < z < 3.5$ to within ∼0.1 magnitudes. There are systematic changes in the average quasar colours as a function of apparent i-band magnitude, which are well explained in our model setup by changes in the strength of the emission lines and the contribution of the host galaxy. We have quantified the changes in the model parameters as a function of i-band magnitude, and extrapolated to fainter magnitudes in order to make predictions for what the median LSST and Euclid colours of new populations of AGN might be. This extrapolation assumes that the trends observed in SDSS continue for another 3 magnitudes in flux - in reality we expect our predictions for the average colours to break down before we reach $i_{AB} = 24$. When and how they break down will provide an insight into the physics of

the fainter quasars will be discovered in the next generations of wide area surveys.

6.1.3 *Hot dust in quasars*

Using data from SDSS, UKIDSS and WISE, we have investigated the properties of the high-frequency cutoff to the infrared emission in ≃5000 carefully selected luminous quasars. The strength of $\simeq 2\,\mu m$ emission, corresponding to emission from the hottest ($T > 1200\,K$) dust in the sublimation zone surrounding the central continuum source, is observed to correlate with the blueshift of the C IV λ1549 emission line. We therefore find that objects with stronger signatures of nuclear outflows tend to have a larger covering fraction of sublimation-temperature dust. When controlling for the observed outflow strength, the hot dust covering fraction does not vary significantly across our sample as a function of luminosity, black hole mass or Eddington fraction. The correlation between the hot dust and the C IV line blueshifts, together with the lack of correlation between the hot dust and other parameters, provides evidence of a direct link between the properties of the broad emission line region and the infrared-emitting dusty regions in quasars.

6.1.4 *[O III] emission in heavily reddened quasars*

We have quantified the Hα, Hβ and [O III] emission line properties in 22 heavily reddened quasars with $L_{bol} \approx 10^{47}\,erg\,s^{-1}$ and $z > 2$, and carried out the first comparison of the [O III] line properties in high luminosity reddened quasars to a large sample of 111 unobscured quasars in the same luminosity and redshift range. Broad wings extending to velocities of $2500\,km\,s^{-1}$ are seen in the [O III] emission line profiles of our reddened quasars, suggesting that strong outflows are affecting the ionised gas kinematics. However, there is no significant difference between the kinematics of the [O III] emission in reddened and unobscured quasars when the two samples are matched in luminosity and redshift. These results are consistent with a model where quasar-driven outflows persist for some time after the obscuring dust has been cleared from along the line of sight. Assuming the amount of ionised gas in reddened and unobscured quasars is similar, we have used the equivalent width distribution of the [O III] emission to constrain the location of the obscuring dust in our reddened quasars: the dust is most likely to be located on galactic scales, outside the [O III] emitting region.

6.2 DISCUSSION

6.2.1 *Quantifying the variance in quasar properties*

We now address the question 'What is the dominant source of variation in the properties of $z \simeq 2$ quasars?', in a manner directly analogous to that used by Boroson and Green (1992) to investigate the variance seen in low redshift quasar spectra.

We take 981 objects which appear in the overlap between the samples used in Chapters 2 and 4, viz. all objects in $1.56 < z < 2.0$ with SDSS spectral S/N > 10 and photometry from UKIDSS and unWISE with $Y < 19.3$. From Chapter 2 we take the equivalent widths of Fe III UV34 and the C III] λ1909 and Si III] λ1892 lines. From Chapter 4 we use the best-fitting blackbody normalisation and the $E(B-V)$ measured when allowing the slope of the continuum to simultaneously vary. We measure the strength of Fe II in the ultraviolet region 2200-3000 Å and the FWHM of the Mg II line, and take the equivalent width and blueshift of the C IV line from Rankine et al. (2020). A Principal Component Analysis (PCA) is carried out to understand which correlations are responsible for the largest amount of variance between these ten properties in our sample of 981 quasars.

The results are shown in Table 6.1 (cf. Table 4 of Boroson and Green, 1992). Here we list the 5 eigenvectors from our PCA which account for the largest fraction of variance in the properties of the sample we use. At the top of each column is listed the cumulative percentage of the variance accounted for by the eigenvectors up to that point.

As expected from the work of Rankine et al. (2020) and Richards et al. (2011), the largest fraction of variance (our 'Eigenvector 1') in the quasar properties we examine is explained by the strong anti-correlation between the equivalent width and blueshift of the C IV line, together with the strong correlation between the equivalent widths of He II and C IV. This eigenvector is also observed to correlate with strength of the C III] line, and anti-correlate with the strengths of Fe III and hot dust, as expected from the results of Chapters 2 and 4.

Our second eigenvector can be interpreted as a set of correlations between the equivalent widths of most of the emission lines (not He II) and the hot dust strength. In other words, it measures the variance in the ultraviolet continuum under the lines which is used to normalise the line strengths, and illustrates the fact that the SED of the continuum which is photoionising the BLR is not necessarily the same as the SED we observe.

The largest amount of variance in the FWHM of Mg II and the strength of the ultraviolet Fe II blends is accounted for by our third eigenvector. We recall that the first eigenvector found by Boroson and Green (1992) was a correlation between the FWHM of Hβ and the strength of the optical Fe II emission, and our third eigenvector may

	Eigenvector 1	Eigenvector 2	Eigenvector 3	Eigenvector 4	Eigenvector 5
	36.8%	53.6%	64.8%	74.5%	82.2%
C IV blueshift	0.450	0.091	-0.050	0.135	-0.175
EW(C IV)	-0.420	0.335	-0.090	-0.083	-0.033
EW(He II λ1640)	-0.456	0.043	-0.281	-0.135	-0.142
$L_{2\,\mu m,HD}/L_{2\,\mu m,QSO}$	0.221	0.444	-0.029	-0.152	0.485
$E(B-V)$	-0.134	-0.146	-0.155	0.903	0.286
EW(Fe III UV34)	0.318	0.401	0.085	0.234	-0.332
EW(C III] λ1909)	-0.386	0.269	-0.243	0.095	-0.038
EW(Si III] λ1892)	0.082	0.532	-0.169	0.025	0.361
FWHM(Mg II)	-0.226	-0.040	0.736	-0.014	0.427
EW(Fe II UV)	-0.197	0.377	0.499	0.230	-0.456

Table 6.1: Correlations of eigenvectors with quasar properties.

be analogous to that. If so, that suggests that the variance observed in the C IV line properties is not necessarily the same as the variance observed in the optical lines, and so may be driven by different factors.

Our fourth eigenvector is dominated by a single property, the change in continuum slope inferred from photometry, and shows that the $E(B-V)$ we derive in Chapter 4 must be accounting for variable dust extinction which is independent of the emission line properties in addition to any changes in the slope of the intrinsic SED.

The fact that no one eigenvector accounts for the majority of the variance shows that there must be multiple drivers for the diversity seen in the ultraviolet spectra (and broadband SEDs) of luminous quasars at $z \simeq 2$.

6.2.2 *Far-infrared properties of luminous quasars*

Debate has raged over the origin of the far-infrared (FIR) emission in luminous AGN. As the emission from the toriodal obscuring structure is insufficient to account for the observed FIR flux, it is usually argued that the FIR emission is predominantly due to dust heated by young stars and supernovae, and thus used as an indicator of the star formation rate (e.g. Harris et al., 2016, and references therein). However, such arguments are based on the assumption that all quasars have the same SED, which is not true (e.g. Krawczyk et al., 2013). The question then arises as to whether or not the diversity of AGN SEDs could encompass variation in the longer wavelength FIR emission, especially in objects with evidence for AGN-driven winds. For example, Symeonidis (2017) argued that the FIR emission in $z \approx 2$ quasars is instead due to dust on kilo-parsec scales which is being heated by the AGN.

To simplify the following qualitative discussion, we do not distinguish between AGN-driven outflows on different scales, but instead consider a toy model where objects either do or do not show evidence for what we hereafter refer to as 'winds'.

Within this model, quasars at $z \approx 2$ which are actively driving winds are expected to show larger C IV blueshifts in their spectra. Maddox et al. (2017) showed that the individual FIR detection rate of such quasars is higher than would be expected for their optical luminosities. More specifically, objects which are detected in the Herschel-ATLAS survey at 100-500 μm are disproportionately more likely to show large C IV blueshifts. Equivalently, quasars with large C IV blueshifts have weaker C IV equivalent widths, and Harris et al. (2016) showed that these objects have stronger Herschel emission when stacking optically selected objects in order to quantify the FIR emission below the individual-object detection limit.

More recently, Baron and Netzer (2019) have shown that type 2 AGN at $z \approx 0.1$ with outflow signatures in [O III] show an excess of emission in the mid-infrared ($3\,\mu m < \lambda < 20\,\mu m$). Together with the result found in Chapter 4 of this thesis, that objects with stronger winds have brighter near-infrared emission, a picture is therefore emerging where objects with stronger winds show stronger emission from dust across a wide range of temperatures. However, while previous works have attributed the brighter FIR emission in objects with stronger winds to increased rates of star formation, the stronger emission from hot, near-sublimation temperature dust which we report in Chapter 4 cannot be ascribed to dust which is being heated by young stars. The evidence we have presented that quasar-driven outflows are affecting the emission from AGN-heated dust structures therefore provides support for the idea that the increased FIR emission in windy quasars has a significant component due to AGN-heated dust and is not solely due to increased rates of star formation.

This scenario is also consistent with the results of Leipski et al. (2014) who showed that FIR-bright quasars have weaker H α and Ly α emission, and that objects with FIR detections are preferentially brighter in the rest frame near-infrared. In the models discussed in Section 4.5.1, quasars which fail to drive strong winds have larger amounts of gas falling back to form the BLR and hence emit stronger broad lines. These objects are also less likely to drive galaxy-scale outflows which in turn removes a source of AGN-heated dust and they thus possess fainter FIR emission.

In Chapter 5 we showed that the [O III] outflow properties in dust-reddened and unobscured quasars are consistent with a model of galaxy formation and evolution where outflows persist after the obscuring dust has cleared from the line of sight. The FIR emission on galaxy scales in unobscured quasars could then be attributed to dust heated by outflows which have been launched from the accretion

disc long in the past, specifically during a previous SMBH fuelling episode and thus at a time when the physical conditions in the inner regions of the AGN were perhaps very different to what they are today (Zubovas and Nardini, 2020). In this light, the interplay between star formation, outflows, and the presence and clearing of dust in massive galaxies needs to be considered as a function of AGN activity over Myr timescales, and not just as a function of their current SMBH accretion rates.

6.3 FUTURE PROSPECTS

All of the work presented in this thesis has made use of single-epoch data. The most exciting prospect in the near future is the large number of surveys which will begin to take multi-epoch data, and thus explore how the properties of quasars and other AGN are varying as a function of time.

The 'Black Hole Mapper' component of SDSS-V (Kollmeier et al., 2017) and the 4MOST Time-Domain Extragalactic Survey (TiDES; Swann et al., 2019) are planning to take hundreds of epochs of spectroscopy for more than a thousand quasars each, with many of those at the redshifts $z \simeq 2$. These observations will provide an insight into how the rest frame ultraviolet emission lines such as C IV and Fe III are varying in response to variations in the continuum flux. It is still not known whether or not the outflowing component of the gas which is emitting C IV is co-located with the component at the systemic redshift, and using reverberation mapping techniques to constrain the radial location of these (possibly disparate) regions of ionised gas would be a major step forward in our understanding of quasar properties.

At the same time, photometric surveys such as LSST will provide high-quality light curves for paradigm-changing numbers of quasars. Of particular relevance are photometric surveys in the infrared such as VEILS (Hönig et al., 2017) which have already started to measure hot dust reverberation lags in large numbers of AGN. Pushing such measurements out to higher redshifts, where the signatures of high ionisation BLR outflows (such as C IV) can be quantified using observed frame optical spectra, will give a new insight into how outflows from the broad line region are involved in shaping their dusty surroundings.

Within the next decade, upcoming data-sets should therefore enable future studies to build on the work presented in this thesis and further understand the interplay between dust emission and outflows on different scales in luminous quasars.

BIBLIOGRAPHY

Alexander, D. M. and R. C. Hickox (2012). 'What drives the growth of black holes?' In: *New A Rev.* 56, pp. 93–121. DOI: 10.1016/j.newar.2011.11.003.

Almeyda, T. et al. (2020). 'Modeling the Infrared Reverberation Response of the Circumnuclear Dusty Torus in AGNs: An Investigation of Torus Response Functions'. In: *ApJ* 891.1, 26, p. 26. DOI: 10.3847/1538-4357/ab6aa1.

Anderson, T. W. and D. A. Darling (1952). 'Asymptotic Theory of Certain "Goodness of Fit" Criteria Based on Stochastic Processes'. In: *Ann. Math. Statist.* 23.2, pp. 193–212. DOI: 10.1214/aoms/1177729437. URL: https://doi.org/10.1214/aoms/1177729437.

Antonucci, R. R. J. and J. S. Miller (1985). 'Spectropolarimetry and the nature of NGC 1068.' In: *ApJ* 297, pp. 621–632. DOI: 10.1086/163559.

Antonucci, R. (1993). 'Unified models for active galactic nuclei and quasars'. In: *ARA&A* 31, pp. 473–521. DOI: 10.1146/annurev.aa.31.090193.002353.

Astropy Collaboration et al. (2013). 'Astropy: A community Python package for astronomy'. In: *A&A* 558, A33, A33. DOI: 10.1051/0004-6361/201322068.

Astropy Collaboration et al. (2018). 'The Astropy Project: Building an Open-science Project and Status of the v2.0 Core Package'. In: *AJ* 156.3, 123, p. 123. DOI: 10.3847/1538-3881/aabc4f.

Badnell, N. R. and C. P. Ballance (2014). 'Electron-impact Excitation of Fe^{2+}: A Comparison of Intermediate Coupling Frame Transformation, Breit-Pauli and Dirac R-matrix Calculations'. In: *ApJ* 785, 99, p. 99. DOI: 10.1088/0004-637X/785/2/99.

Baldwin, J. A. et al. (1996). 'Very High Density Clumps and Outflowing Winds in QSO Broad-Line Regions'. In: *ApJ* 461, p. 664. DOI: 10.1086/177093.

Baldwin, J. A. et al. (2004). 'The Origin of Fe II Emission in Active Galactic Nuclei'. In: *ApJ* 615, pp. 610–624. DOI: 10.1086/424683.

Baldwin, J. et al. (1995). 'Locally Optimally Emitting Clouds and the Origin of Quasar Emission Lines'. In: *ApJL* 455, pp. L119+. DOI: 10.1086/309827.

Baldwin, J. A. (1977). 'Luminosity Indicators in the Spectra of Quasi-Stellar Objects'. In: *ApJ* 214, pp. 679–684. DOI: 10.1086/155294.

Banerji, M. et al. (2012). 'Heavily reddened quasars at $z \sim 2$ in the UKIDSS Large Area Survey: a transitional phase in AGN evolution'. In: *MNRAS* 427, pp. 2275–2291. DOI: 10.1111/j.1365-2966.2012.22099.x.

Banerji, M. et al. (2013). 'Hyperluminous reddened broad-line quasars at $z \sim 2$ from the VISTA Hemisphere Survey and WISE all-sky survey'. In: *MNRAS* 429, pp. L55–L59. DOI: 10.1093/mnrasl/sls023.

Banerji, M. et al. (2015). 'Heavily reddened type 1 quasars at $z > 2$ - I. Evidence for significant obscured black hole growth at the highest quasar luminosities'. In: *MNRAS* 447, pp. 3368–3389. DOI: 10.1093/mnras/stu2649.

Banerji, M. et al. (2017). 'The discovery of gas-rich, dusty starbursts in luminous reddened quasars at $z \sim 2.5$ with ALMA'. In: *MNRAS* 465, pp. 4390–4405. DOI: 10.1093/mnras/stw3019.

Banerji, M. et al. (2018). 'The interstellar medium properties of heavily reddened quasars and companions at $z \sim 2.5$ with ALMA and JVLA'. In: *MNRAS* 479, pp. 1154–1169. DOI: 10.1093/mnras/sty1443.

Baron, D. and H. Netzer (2019). 'Discovering AGN-driven winds through their infrared emission - I. General method and wind location'. In: *MNRAS* 482, pp. 3915–3932. DOI: 10.1093/mnras/sty2935.

Barvainis, R. (1987). 'Hot Dust and the Near-Infrared Bump in the Continuum Spectra of Quasars and Active Galactic Nuclei'. In: *ApJ* 320, p. 537. DOI: 10.1086/165571.

Baskin, A. and A. Laor (2005). 'What controls the [OIII] λ5007 line strength in active galactic nuclei?' In: *MNRAS* 358, pp. 1043–1054. DOI: 10.1111/j.1365-2966.2005.08841.x.

Baskin, A. and A. Laor (2018). 'Dust inflated accretion disc as the origin of the broad line region in active galactic nuclei'. In: *MNRAS* 474.2, pp. 1970–1994. DOI: 10.1093/mnras/stx2850.

Bernstein, R. A., W. L. Freedman and B. F. Madore (2002). 'The First Detections of the Extragalactic Background Light at 3000, 5500, and 8000 Å. III. Cosmological Implications'. In: *ApJ* 571.1, pp. 107–128. DOI: 10.1086/339424.

Bischetti, M. et al. (2017). 'The WISSH quasars project. I. Powerful ionised outflows in hyper-luminous quasars'. In: *A&A* 598, A122, A122. DOI: 10.1051/0004-6361/201629301.

Boroson, T. A. and R. F. Green (1992). 'The emission-line properties of low-redshift quasi-stellar objects'. In: *ApJS* 80, pp. 109–135. DOI: 10.1086/191661.

Bottorff, M. et al. (2000). 'Observational Constraints on the Internal Velocity Field of Quasar Emission-Line Clouds'. In: *ApJ* 542, pp. 644–654. DOI: 10.1086/317051.

Boyle, B. J. et al. (2000). 'The 2dF QSO Redshift Survey - I. The optical luminosity function of quasi-stellar objects'. In: *MNRAS* 317.4, pp. 1014–1022. DOI: 10.1046/j.1365-8711.2000.03730.x.

Brusa, M. et al. (2015). 'X-shooter reveals powerful outflows in $z \sim 1.5$ X-ray selected obscured quasi-stellar objects'. In: *MNRAS* 446, pp. 2394–2417. DOI: 10.1093/mnras/stu2117.

Casebeer, D. A., K. M. Leighly and E. Baron (2006). 'FUSE Observation of the Narrow-Line Seyfert 1 Galaxy RE 1034+39: Dependence of Broad Emission Line Strengths on the Shape of the Photoionizing Spectrum'. In: *ApJ* 637.1, pp. 157–182. DOI: 10.1086/498125.

Cicone, C. et al. (2014). 'Massive molecular outflows and evidence for AGN feedback from CO observations'. In: *A&A* 562, A21, A21. DOI: 10.1051/0004-6361/201322464.

Clerk Maxwell, J. (1865). 'A Dynamical Theory of the Electromagnetic Field'. In: *Philosophical Transactions of the Royal Society* 155, pp. 459–512.

Coatman, L. et al. (2016). 'C IV emission-line properties and systematic trends in quasar black hole mass estimates'. In: *MNRAS* 461, pp. 647–665. DOI: 10.1093/mnras/stw1360.

Coatman, L. et al. (2017). 'Correcting C IV-based virial black hole masses'. In: *MNRAS* 465, pp. 2120–2142. DOI: 10.1093/mnras/stw2797.

Coatman, L. et al. (2019). 'Kinematics of C IV and [O III] emission in luminous high-redshift quasars'. In: *MNRAS* 486.4, pp. 5335–5348. DOI: 10.1093/mnras/stz1167.

Croom, S. M. et al. (2001). 'The 2dF QSO Redshift Survey - V. The 10k catalogue'. In: *MNRAS* 322.4, pp. L29–L36. DOI: 10.1046/j.1365-8711.2001.04474.x.

Croom, S. M. et al. (2004). 'The 2dF QSO Redshift Survey - XII. The spectroscopic catalogue and luminosity function'. In: *MNRAS* 349.4, pp. 1397–1418. DOI: 10.1111/j.1365-2966.2004.07619.x.

Czerny, B. and K. Hryniewicz (2011). 'The origin of the broad line region in active galactic nuclei'. In: *A&A* 525, L8, p. L8. DOI: 10.1051/0004-6361/201016025.

Czerny, B. et al. (2017). 'Failed Radiatively Accelerated Dusty Outflow Model of the Broad Line Region in Active Galactic Nuclei. I. Analytical Solution'. In: *ApJ* 846.2, 154, p. 154. DOI: 10.3847/1538-4357/aa8810.

Darling, D. A. (1957). 'The Kolmogorov-Smirnov, Cramer-von Mises Tests'. In: *Ann. Math. Statist.* 28.4, pp. 823–838. DOI: 10.1214/aoms/1177706788. URL: https://doi.org/10.1214/aoms/1177706788.

Di Matteo, T., V. Springel and L. Hernquist (2005). 'Energy input from quasars regulates the growth and activity of black holes and their host galaxies'. In: *Nature* 433, pp. 604–607. DOI: 10.1038/nature03335.

DiPompeo, M. A. et al. (2018). 'The [O III] Profiles of Infrared-selected Active Galactic Nuclei: More Powerful Outflows in the Obscured Population'. In: *ApJ* 856, 76, p. 76. DOI: 10.3847/1538-4357/aab365.

Dopita, M. A. and R. S. Sutherland (2003). *Astrophysics of the diffuse universe*. Springer, Astronomy and astrophysics library, ISBN 3540433627.

Draine, B. T. (2003). 'Interstellar Dust Grains'. In: *ARA&A* 41, pp. 241–289. DOI: 10.1146/annurev.astro.41.011802.094840.

Eddington, A. S. (1925). 'A limiting case in the theory of radiative equilibrium'. In: *MNRAS* 85, p. 408. DOI: 10.1093/mnras/85.5.408.

Edge, A. et al. (2013). 'The VISTA Kilo-degree Infrared Galaxy (VIKING) Survey: Bridging the Gap between Low and High Redshift'. In: *The Messenger* 154, pp. 32–34.

Einstein, A. (1915). 'Die Feldgleichungen der Gravitation'. In: *Sitzungsber. Königl. Preuss. Akad. Wissenschaften*, pp. 844–847.

Elitzur, M. and I. Shlosman (2006). 'The AGN-obscuring Torus: The End of the "Doughnut" Paradigm?' In: *ApJL* 648.2, pp. L101–L104. DOI: 10.1086/508158.

Elvis, M. et al. (1994). 'Atlas of Quasar Energy Distributions'. In: *ApJS* 95, p. 1. DOI: 10.1086/192093.

Euclid Collaboration et al. (2019). 'Euclid preparation. V. Predicted yield of redshift $7 < z < 9$ quasars from the wide survey'. In: *A&A* 631, A85, A85. DOI: 10.1051/0004-6361/201936427.

Event Horizon Telescope Collaboration et al. (2019). 'First M87 Event Horizon Telescope Results. I. The Shadow of the Supermassive Black Hole'. In: *ApJL* 875.1, L1, p. L1. DOI: 10.3847/2041-8213/ab0ec7.

Fabian, A. C. (2012). 'Observational Evidence of Active Galactic Nuclei Feedback'. In: *ARA&A* 50, pp. 455–489. DOI: 10.1146/annurev-astro-081811-125521.

Fabian, A. C., A. Celotti and M. C. Erlund (2006). 'Radiative pressure feedback by a quasar in a galactic bulge'. In: *MNRAS* 373.1, pp. L16–L20. DOI: 10.1111/j.1745-3933.2006.00234.x.

Fabian, A. C., R. V. Vasudevan and P. Gandhi (2008). 'The effect of radiation pressure on dusty absorbing gas around active galactic nuclei'. In: *MNRAS* 385.1, pp. L43–L47. DOI: 10.1111/j.1745-3933.2008.00430.x.

Fabian, A. C. et al. (2009). 'Radiation pressure and absorption in AGN: results from a complete unbiased sample from Swift'. In: *MNRAS* 394.1, pp. L89–L92. DOI: 10.1111/j.1745-3933.2009.00617.x.

Faucher-Giguère, C.-A. et al. (2008). 'A Direct Precision Measurement of the Intergalactic Lyα Opacity at $2 <= z <= 4.2$'. In: *ApJ* 681.2, pp. 831–855. DOI: 10.1086/588648.

Ferland, G. J. (1992). 'N III Line Emission in Planetary Nebulae: Continuum Fluorescence'. In: *ApJL* 389, p. L63. DOI: 10.1086/186349.

Ferland, G. J. et al. (2017). 'The 2017 Release Cloudy'. In: *Revista Mexicana de Astronomia y Astrofisica* 53, pp. 385–438.

Ferland, G. J. et al. (2020). 'State-of-the-art AGN SEDs for photoionization models: BLR predictions confront the observations'. In: *MNRAS* 494.4, pp. 5917–5922. DOI: 10.1093/mnras/staa1207.

Ferrarese, L. and D. Merritt (2000). 'A Fundamental Relation between Supermassive Black Holes and Their Host Galaxies'. In: *ApJL* 539.1, pp. L9–L12. DOI: 10.1086/312838.

Feruglio, C. et al. (2010). 'Quasar feedback revealed by giant molecular outflows'. In: *A&A* 518, L155, p. L155. DOI: 10.1051/0004-6361/201015164.

Fian, C. et al. (2018). 'Microlensing and Intrinsic Variability of the Broad Emission Lines of Lensed Quasars'. In: *ApJ* 859.1, 50, p. 50. DOI: 10.3847/1538-4357/aabc0d.

Figaredo, C. S. et al. (2020). 'Dust Reverberation of 3C 273: Torus Structure and Lag-Luminosity Relation'. In: *AJ* 159.6, 259, p. 259. DOI: 10.3847/1538-3881/ab89b1.

Finkelstein, D. (1958). 'Past-Future Asymmetry of the Gravitational Field of a Point Particle'. In: *Physical Review* 110.4, pp. 965–967. DOI: 10.1103/PhysRev.110.965.

Fiore, F. et al. (2017). 'AGN wind scaling relations and the co-evolution of black holes and galaxies'. In: *A&A* 601, A143, A143. DOI: 10.1051/0004-6361/201629478.

Fitzpatrick, E. L. and D. Massa (2009). 'An Analysis of the Shapes of Interstellar Extinction Curves. VI. The Near-IR Extinction Law'. In: *ApJ* 699.2, pp. 1209–1222. DOI: 10.1088/0004-637X/699/2/1209.

Foreman-Mackey, D. (2016). 'corner.py: Scatterplot matrices in Python'. In: *Journal of Open Source Software* 1.2, p. 24. DOI: 10.21105/joss.00024.

Foreman-Mackey, D. et al. (2013). 'emcee: The MCMC Hammer'. In: *PASP* 125.925, p. 306. DOI: 10.1086/670067.

Francis, P. J. et al. (1991). 'A High Signal-to-Noise Ratio Composite Quasar Spectrum'. In: *ApJ* 373, p. 465. DOI: 10.1086/170066.

Gallerani, S. et al. (2010). 'The extinction law at high redshift and its implications'. In: *A&A* 523, A85, A85. DOI: 10.1051/0004-6361/201014721.

Gebhardt, K. et al. (2000). 'A Relationship between Nuclear Black Hole Mass and Galaxy Velocity Dispersion'. In: *ApJL* 539.1, pp. L13–L16. DOI: 10.1086/312840.

Gillessen, S. et al. (2009). 'Monitoring Stellar Orbits Around the Massive Black Hole in the Galactic Center'. In: *ApJ* 692.2, pp. 1075–1109. DOI: 10.1088/0004-637X/692/2/1075.

Giustini, M. and D. Proga (2019). 'A global view of the inner accretion and ejection flow around super massive black holes. Radiation-driven accretion disk winds in a physical context'. In: *A&A* 630, A94, A94. DOI: 10.1051/0004-6361/201833810.

Glikman, E., D. J. Helfand and R. L. White (2006). 'A Near-Infrared Spectral Template for Quasars'. In: *ApJ* 640.2, pp. 579–591. DOI: 10.1086/500098.

Goad, M. R., K. T. Korista and A. J. Ruff (2012). 'The broad emission-line region: the confluence of the outer accretion disc with the inner edge of the dusty torus'. In: *MNRAS* 426.4, pp. 3086–3111. DOI: 10.1111/j.1365-2966.2012.21808.x.

Goodman, J. and J. Weare (2010). 'Ensemble samplers with affine invariance'. In: *Communications in Applied Mathematics and Computational Science* 5.1, pp. 65–80. DOI: 10.2140/camcos.2010.5.65.

Graham, M. J., R. G. Clowes and L. E. Campusano (1996). 'A quasar with ultrastrong, ultraviolet Fe II emission.' In: *MNRAS* 279.4, pp. 1349–1356. DOI: 10.1093/mnras/279.4.1349.

Grandi, S. A. (1982). 'The 3000 A bump in quasars'. In: *ApJ* 255, pp. 25–38. DOI: 10.1086/159799.

Gravity Collaboration et al. (2020). 'The resolved size and structure of hot dust in the immediate vicinity of AGN'. In: *A&A* 635, A92, A92. DOI: 10.1051/0004-6361/201936767.

Green, R. F. et al. (1980). 'Observations of quasars with the International Ultraviolet Explorer satellite.' In: *ApJ* 239, pp. 483–494. DOI: 10.1086/158132.

Greene, J. E., N. L. Zakamska and P. S. Smith (2012). 'A Spectacular Outflow in an Obscured Quasar'. In: *ApJ* 746, 86, p. 86. DOI: 10.1088/0004-637X/746/1/86.

Greene, J. E. et al. (2011). 'Feedback in Luminous Obscured Quasars'. In: *ApJ* 732, 9, p. 9. DOI: 10.1088/0004-637X/732/1/9.

Greenstein, J. L. (1963). 'Red-Shift of the Unusual Radio Source: 3C 48'. In: *Nature* 197.4872, pp. 1041–1042. DOI: 10.1038/1971041a0.

Grier, C. J. et al. (2019). 'The Sloan Digital Sky Survey Reverberation Mapping Project: Initial C IV Lag Results from Four Years of Data'. In: *ApJ* 887.1, 38, p. 38. DOI: 10.3847/1538-4357/ab4ea5.

Hamann, F. et al. (2017). 'Extremely red quasars in BOSS'. In: *MNRAS* 464, pp. 3431–3463. DOI: 10.1093/mnras/stw2387.

Hao, H. et al. (2013). 'A quasar-galaxy mixing diagram: quasar spectral energy distribution shapes in the optical to near-infrared'. In: *MNRAS* 434.4, pp. 3104–3121. DOI: 10.1093/mnras/stt1228.

Harris, C. R. et al. (2020). 'Array Programming with NumPy'. In: *Nature* 585, pp. 357–362. DOI: 10.1038/s41586-020-2649-2.

Harris, K. et al. (2016). 'Star formation rates in luminous quasars at $2 < z < 3$'. In: *MNRAS* 457.4, pp. 4179–4194. DOI: 10.1093/mnras/stw286.

Harrison, C. M. (2017). 'Impact of supermassive black hole growth on star formation'. In: *Nature Astronomy* 1, 0165, p. 0165. DOI: 10.1038/s41550-017-0165.

Harrison, C. M. et al. (2014). 'Kiloparsec-scale outflows are prevalent among luminous AGN: outflows and feedback in the context of the overall AGN population'. In: *MNRAS* 441, pp. 3306–3347. DOI: 10.1093/mnras/stu515.

Harrison, C. M. et al. (2016). 'The KMOS AGN Survey at High redshift (KASHz): the prevalence and drivers of ionized outflows in the host galaxies of X-ray AGN'. In: *MNRAS* 456, pp. 1195–1220. DOI: 10.1093/mnras/stv2727.

Harrison, C. M. et al. (2018). 'AGN outflows and feedback twenty years on'. In: *Nature Astronomy* 2, pp. 198–205. DOI: 10.1038/s41550-018-0403-6.

Hazard, C., M. B. Mackey and A. J. Shimmins (1963). 'Investigation of the Radio Source 3C 273 By The Method of Lunar Occultations'. In: *Nature* 197.4872, pp. 1037–1039. DOI: 10.1038/1971037a0.

Hewett, P. C. et al. (2006). 'The UKIRT Infrared Deep Sky Survey ZY JHK photometric system: passbands and synthetic colours'. In: *MNRAS* 367.2, pp. 454–468. DOI: 10.1111/j.1365-2966.2005.09969.x.

Hönig, S. F. (2014). 'Dust Reverberation Mapping in the Era of Big Optical Surveys and its Cosmological Application'. In: *ApJL* 784.1, L4, p. L4. DOI: 10.1088/2041-8205/784/1/L4.

Hönig, S. F. et al. (2017). 'Cosmology with AGN dust time lags-simulating the new VEILS survey'. In: *MNRAS* 464.2, pp. 1693–1703. DOI: 10.1093/mnras/stw2484.

Hönig, S. F. (2019). 'Redefining the Torus: A Unifying View of AGNs in the Infrared and Submillimeter'. In: *ApJ* 884.2, 171, p. 171. DOI: 10.3847/1538-4357/ab4591.

Hopkins, P. F. et al. (2008). 'A Cosmological Framework for the Co-Evolution of Quasars, Supermassive Black Holes, and Elliptical Galaxies. I. Galaxy Mergers and Quasar Activity'. In: *ApJS* 175, pp. 356–389. DOI: 10.1086/524362.

Hopkins, P. F. et al. (2004). 'Dust Reddening in Sloan Digital Sky Survey Quasars'. In: *AJ* 128.3, pp. 1112–1123. DOI: 10.1086/423291.

Hu, C. et al. (2015). 'Supermassive Black Holes with High Accretion Rates in Active Galactic Nuclei. III. Detection of Fe II Reverberation in Nine Narrow-line Seyfert 1 Galaxies'. In: *ApJ* 804.2, 138, p. 138. DOI: 10.1088/0004-637X/804/2/138.

Hunter, J. D. (2007). 'Matplotlib: A 2D graphics environment'. In: *Computing In Science & Engineering* 9.3, pp. 90–95. DOI: 10.1109/MCSE.2007.55.

Ishibashi, W., M. Banerji and A. C. Fabian (2017). 'AGN radiative feedback in dusty quasar populations'. In: *MNRAS* 469, pp. 1496–1501. DOI: 10.1093/mnras/stx921.

Ishibashi, W. and A. C. Fabian (2015). 'AGN feedback: galactic-scale outflows driven by radiation pressure on dust'. In: *MNRAS* 451, pp. 93–102. DOI: 10.1093/mnras/stv944.

Ishibashi, W. et al. (2018). 'Revisiting the 'forbidden' region: AGN radiative feedback with radiation trapping'. In: *MNRAS* 479.3, pp. 3335–3342. DOI: 10.1093/mnras/sty1620.

Ivezić, Ž. et al. (2019). 'LSST: From Science Drivers to Reference Design and Anticipated Data Products'. In: *ApJ* 873.2, 111, p. 111. DOI: 10.3847/1538-4357/ab042c.

Jiang, L. et al. (2010). 'Dust-free quasars in the early Universe'. In: *Nature* 464.7287, pp. 380–383. DOI: 10.1038/nature08877.

Jin, C., M. Ward and C. Done (2012). 'A combined optical and X-ray study of unobscured type 1 active galactic nuclei - III. Broad-band SED properties'. In: *MNRAS* 425.2, pp. 907–929. DOI: 10.1111/j.1365-2966.2012.21272.x.

Karouzos, M., J.-H. Woo and H.-J. Bae (2016). 'Unraveling the Complex Structure of AGN-driven Outflows. I. Kinematics and Sizes'. In: *ApJ* 819, 148, p. 148. DOI: 10.3847/0004-637X/819/2/148.

Kerr, R. P. (1963). 'Gravitational Field of a Spinning Mass as an Example of Algebraically Special Metrics'. In: *Phys. Rev. Lett.* 11.5, pp. 237–238. DOI: 10.1103/PhysRevLett.11.237.

Kim, D. and M. Im (2018). 'What makes red quasars red?. Observational evidence for dust extinction from line ratio analysis'. In: *A&A* 610, A31, A31. DOI: 10.1051/0004-6361/201731963.

King, A. and K. Pounds (2015). 'Powerful Outflows and Feedback from Active Galactic Nuclei'. In: *ARA&A* 53, pp. 115–154. DOI: 10.1146/annurev-astro-082214-122316.

Kishimoto, M. et al. (2009). 'Exploring the inner region of type 1 AGNs with the Keck interferometer'. In: *A&A* 507.3, pp. L57–L60. DOI: 10.1051/0004-6361/200913512.

Kishimoto, M. et al. (2011). 'The innermost dusty structure in active galactic nuclei as probed by the Keck interferometer'. In: *A&A* 527, A121, A121. DOI: 10.1051/0004-6361/201016054.

Kollmeier, J. A. et al. (2017). 'SDSS-V: Pioneering Panoptic Spectroscopy'. In: *arXiv e-prints*, arXiv:1711.03234, arXiv:1711.03234.

Konigl, A. and J. F. Kartje (1994). 'Disk-driven hydromagnetic winds as a key ingredient of active galactic nuclei unification schemes'. In: *ApJ* 434, pp. 446–467. DOI: 10.1086/174746.

Koposov, S. and O. Bartunov (2006). 'Q3C, Quad Tree Cube – The new Sky-indexing Concept for Huge Astronomical Catalogues and its Realization for Main Astronomical Queries (Cone Search and Xmatch) in Open Source Database PostgreSQL'. In: *Astronomical Data Analysis Software and Systems XV*. Ed. by C. Gabriel et al. Vol. 351. Astronomical Society of the Pacific Conference Series, p. 735.

Korista, K. T. and M. R. Goad (2004). 'What the Optical Recombination Lines Can Tell Us about the Broad-Line Regions of Active Galactic Nuclei'. In: *ApJ* 606, pp. 749–762. DOI: 10.1086/383193.

Korista, K. et al. (1997). 'An Atlas of Computed Equivalent Widths of Quasar Broad Emission Lines'. In: *ApJS* 108, p. 401. DOI: 10.1086/312966.

Kormendy, J. and L. C. Ho (2013). 'Coevolution (Or Not) of Supermassive Black Holes and Host Galaxies'. In: *ARA&A* 51, pp. 511–653. DOI: 10.1146/annurev-astro-082708-101811.

Koshida, S. et al. (2014). 'Reverberation Measurements of the Inner Radius of the Dust Torus in 17 Seyfert Galaxies'. In: *ApJ* 788.2, 159, p. 159. DOI: 10.1088/0004-637X/788/2/159.

Kovačević, J., L. Č. Popović and M. S. Dimitrijević (2010). 'Analysis of Optical Fe II Emission in a Sample of Active Galactic Nucleus Spectra'. In: *ApJS* 189, pp. 15–36. DOI: 10.1088/0067-0049/189/1/15.

Kramida, A. et al. (2018). NIST Atomic Spectra Database (ver. 5.6.1), [Online]. Available: https://physics.nist.gov/asd [2019, February 26]. National Institute of Standards and Technology, Gaithersburg, MD.

Krawczyk, C. M. et al. (2013). 'Mean Spectral Energy Distributions and Bolometric Corrections for Luminous Quasars'. In: *ApJS* 206.1, 4, p. 4. DOI: 10.1088/0067-0049/206/1/4.

Kulkarni, G., G. Worseck and J. F. Hennawi (2019). 'Evolution of the AGN UV luminosity function from redshift 7.5'. In: *MNRAS* 488.1, pp. 1035–1065. DOI: 10.1093/mnras/stz1493.

Kurk, J. D. et al. (2009). 'Near-Infrared Spectroscopy of SDSS J0303-0019: A Low-luminosity, High-Eddington-Ratio Quasar at z ~ 6'. In: *ApJ* 702.2, pp. 833–837. DOI: 10.1088/0004-637X/702/2/833.

Kurk, J. D. et al. (2007). 'Black Hole Masses and Enrichment of z ~ 6 SDSS Quasars'. In: *ApJ* 669.1, pp. 32–44. DOI: 10.1086/521596.

Laha, S. et al. (2017). 'Emission Line Ratios of Fe III as Astrophysical Plasma Diagnostics'. In: *ApJ* 841.1, 3, p. 3. DOI: 10.3847/1538-4357/aa7071.

Landt, H. et al. (2019). 'The first spectroscopic dust reverberation programme on active galactic nuclei: the torus in NGC 5548'. In: *MNRAS* 489.2, pp. 1572–1589. DOI: 10.1093/mnras/stz2212.

Lansbury, G. B. et al. (2020). 'X-ray observations of luminous dusty quasars at z > 2'. In: *MNRAS* 495.3, pp. 2652–2663. DOI: 10.1093/mnras/staa1220.

Laureijs, R. et al. (2011). 'Euclid Definition Study Report'. In: *arXiv e-prints*, arXiv:1110.3193, arXiv:1110.3193.

Lawrence, A. et al. (2007). 'The UKIRT Infrared Deep Sky Survey (UKIDSS)'. In: *MNRAS* 379.4, pp. 1599–1617. DOI: 10.1111/j.1365-2966.2007.12040.x.

Leipski, C. et al. (2014). 'Spectral Energy Distributions of QSOs at z > 5: Common Active Galactic Nucleus-heated Dust and Occasionally Strong Star-formation'. In: *ApJ* 785.2, 154, p. 154. DOI: 10.1088/0004-637X/785/2/154.

Li, J. et al. (2017). 'The Sloan Digital Sky Survey Reverberation Mapping Project: Composite Lags at $z < 1$'. In: *ApJ* 846, 79, p. 79. DOI: 10.3847/1538-4357/aa845d.

Liu, G. et al. (2013). 'Observations of feedback from radio-quiet quasars - II. Kinematics of ionized gas nebulae'. In: *MNRAS* 436, pp. 2576–2597. DOI: 10.1093/mnras/stt1755.

Lupton, R. H., J. E. Gunn and A. S. Szalay (1999). 'A Modified Magnitude System that Produces Well-Behaved Magnitudes, Colors, and Errors Even for Low Signal-to-Noise Ratio Measurements'. In: *AJ* 118.3, pp. 1406–1410. DOI: 10.1086/301004.

Lykins, M. L. et al. (2013). 'Radiative cooling in collisionally ionized and photoionized plasmas'. In: *MNRAS* 429.4, pp. 3133–3143. DOI: 10.1093/mnras/sts570.

Lynden-Bell, D. (1969). 'Galactic Nuclei as Collapsed Old Quasars'. In: *Nature* 223, pp. 690–694. DOI: 10.1038/223690a0.

Madau, P. and M. Dickinson (2014). 'Cosmic Star-Formation History'. In: *ARA&A* 52, pp. 415–486. DOI: 10.1146/annurev-astro-081811-125615.

Maddox, N. et al. (2008). 'Luminous K-band selected quasars from UKIDSS'. In: *MNRAS* 386, pp. 1605–1624. DOI: 10.1111/j.1365-2966.2008.13138.x.

Maddox, N. et al. (2017). 'Far-infrared emission in luminous quasars accompanied by nuclear outflows'. In: *MNRAS* 470, pp. 2314–2319. DOI: 10.1093/mnras/stx1416.

Maddox, N. et al. (2012). 'The large area KX quasar catalogue - I. Analysis of the photometric redshift selection and the complete quasar catalogue'. In: *MNRAS* 424.4, pp. 2876–2895. DOI: 10.1111/j.1365-2966.2012.21427.x.

Magorrian, J. et al. (1998). 'The Demography of Massive Dark Objects in Galaxy Centers'. In: *AJ* 115, pp. 2285–2305. DOI: 10.1086/300353.

Marziani, P. and J. W. Sulentic (2014). 'Highly accreting quasars: sample definition and possible cosmological implications'. In: *MNRAS* 442.2, pp. 1211–1229. DOI: 10.1093/mnras/stu951.

Marziani, P. et al. (2018). 'A main sequence for quasars'. In: *Frontiers in Astronomy and Space Sciences* 5, 6, p. 6. DOI: 10.3389/fspas.2018.00006.

McConnell, N. J. and C.-P. Ma (2013). 'Revisiting the Scaling Relations of Black Hole Masses and Host Galaxy Properties'. In: *ApJ* 764, 184, p. 184. DOI: 10.1088/0004-637X/764/2/184.

McMahon, R. G. et al. (2013). 'First Scientific Results from the VISTA Hemisphere Survey (VHS)'. In: *The Messenger* 154, pp. 35–37.

Mediavilla, E. et al. (2018). 'Systematic Redshift of the Fe III UV Lines in Quasars: Measuring Supermassive Black Hole Masses under the Gravitational Redshift Hypothesis'. In: *ApJ* 862.2, 104, p. 104. DOI: 10.3847/1538-4357/aacbd3.

Mediavilla, E. et al. (2019). 'Measuring Supermassive Black Hole Masses: Correlation between the Redshifts of the Fe III UV Lines and the Widths of Broad Emission Lines'. In: *ApJ* 880.2, 96, p. 96. DOI: 10.3847/1538-4357/ab2910.

Meisner, A. M. et al. (2019). 'unWISE Coadds: The Five-year Data Set'. In: *PASP* 131.1006, p. 124504. DOI: 10.1088/1538-3873/ab3df4.

Michell, J. (1784). 'On the Means of Discovering the Distance, Magnitude, &c. of the Fixed Stars, in Consequence of the Diminution of the Velocity of Their Light, in Case Such a Diminution Should be Found to Take Place in any of Them, and Such Other Data Should be Procured from Observations, as Would be Farther Necessary for

That Purpose. By the Rev. John Michell, B. D. F. R. S. In a Letter to Henry Cavendish, Esq. F. R. S. and A. S.' In: *Philosophical Transactions of the Royal Society* 74, pp. 35–57.

Minezaki, T. et al. (2019). 'Reverberation Measurements of the Inner Radii of the Dust Tori in Quasars'. In: *ApJ* 886.2, 150, p. 150. DOI: 10.3847/1538-4357/ab4f7b.

Miyoshi, M. et al. (1995). 'Evidence for a black hole from high rotation velocities in a sub-parsec region of NGC4258'. In: *Nature* 373.6510, pp. 127–129. DOI: 10.1038/373127a0.

Moore, C. E. (1952). *An ultraviolet multiplet table*. National Bureau of Standards.

Murray, N. et al. (1995). 'Accretion Disk Winds from Active Galactic Nuclei'. In: *ApJ* 451, p. 498. DOI: 10.1086/176238.

Myers, A. D. et al. (2015). 'The SDSS-IV Extended Baryon Oscillation Spectroscopic Survey: Quasar Target Selection'. In: *ApJS* 221.2, 27, p. 27. DOI: 10.1088/0067-0049/221/2/27.

Narayanan, D. et al. (2010). 'A physical model for z ~ 2 dust-obscured galaxies'. In: *MNRAS* 407, pp. 1701–1720. DOI: 10.1111/j.1365-2966.2010.16997.x.

Netzer, H. (2015). 'Revisiting the Unified Model of Active Galactic Nuclei'. In: *ARA&A* 53, pp. 365–408. DOI: 10.1146/annurev-astro-082214-122302.

Netzer, H. et al. (2004). 'Near-Infrared Spectroscopy of High-Redshift Active Galactic Nuclei. II. Disappearing Narrow-Line Regions and the Role of Accretion'. In: *ApJ* 614, pp. 558–567. DOI: 10.1086/423608.

Osterbrock, D. E. and G. J. Ferland (2006). *Astrophysics of gaseous nebulae and active galactic nuclei, 2nd. ed.* Sausalito, CA: University Science Books.

Padovani, P. et al. (2017). 'Active galactic nuclei: what's in a name?' In: *A&A Rev.* 25, 2, p. 2. DOI: 10.1007/s00159-017-0102-9.

Pâris, I. et al. (2017). 'The Sloan Digital Sky Survey Quasar Catalog: Twelfth data release'. In: *A&A* 597, A79, A79. DOI: 10.1051/0004-6361/201527999.

Pâris, I. et al. (2018). 'The Sloan Digital Sky Survey Quasar Catalog: Fourteenth data release'. In: *A&A* 613, A51, A51. DOI: 10.1051/0004-6361/201732445.

Peacock, J. A. (1983). 'Two-dimensional goodness-of-fit testing in astronomy'. In: *MNRAS* 202, pp. 615–627. DOI: 10.1093/mnras/202.3.615.

Perrotta, S. et al. (2019). 'ERQs are the BOSS of quasar samples: the highest velocity [O III] quasar outflows'. In: *MNRAS* 488.3, pp. 4126–4148. DOI: 10.1093/mnras/stz1993.

Peterson, B. M. (1993). 'Reverberation mapping of active galactic nuclei'. In: *PASP* 105, pp. 247–268. DOI: 10.1086/133140.

Peterson, B. M. (2006). 'The Broad-Line Region in Active Galactic Nuclei'. In: *Physics of Active Galactic Nuclei at all Scales*. Ed. by D. Alloin. Vol. 693. Lecture Notes in Physics, Berlin Springer Verlag, p. 77. DOI: 10.1007/3-540-34621-X_3.

Pogson, N. (1856). 'Magnitudes of Thirty-six of the Minor Planets for the first day of each month of the year 1857'. In: *MNRAS* 17, pp. 12–15. DOI: 10.1093/mnras/17.1.12.

Polletta, M. et al. (2007). 'Spectral Energy Distributions of Hard X-Ray Selected Active Galactic Nuclei in the XMM-Newton Medium Deep Survey'. In: *ApJ* 663.1, pp. 81–102. DOI: 10.1086/518113.

Proga, D., J. M. Stone and T. R. Kallman (2000). 'Dynamics of Line-driven Disk Winds in Active Galactic Nuclei'. In: *ApJ* 543.2, pp. 686–696. DOI: 10.1086/317154.

Rankine, A. L. et al. (2020). 'BAL and non-BAL quasars: continuum, emission, and absorption properties establish a common parent sample'. In: *MNRAS* 492.3, pp. 4553–4575. DOI: 10.1093/mnras/staa130.

Rees, M. J. et al. (1969). 'Infrared Radiation from Dust in Seyfert Galaxies'. In: *Nature* 223.5208, pp. 788–791. DOI: 10.1038/223788a0.

Richards, G. T. et al. (2002). 'Spectroscopic Target Selection in the Sloan Digital Sky Survey: The Quasar Sample'. In: *AJ* 123.6, pp. 2945–2975. DOI: 10.1086/340187.

Richards, G. T. et al. (2003). 'Red and Reddened Quasars in the Sloan Digital Sky Survey'. In: *AJ* 126.3, pp. 1131–1147. DOI: 10.1086/377014.

Richards, G. T. et al. (2006). 'Spectral Energy Distributions and Multi-wavelength Selection of Type 1 Quasars'. In: *ApJS* 166.2, pp. 470–497. DOI: 10.1086/506525.

Richards, G. T. et al. (2011). 'Unification of Luminous Type 1 Quasars through C IV Emission'. In: *AJ* 141.5, 167, p. 167. DOI: 10.1088/0004-6256/141/5/167.

Rieke, G. H. (1978). 'The infrared emission of Seyfert galaxies.' In: *ApJ* 226, pp. 550–558. DOI: 10.1086/156639.

Ross, N. P. et al. (2012). 'The SDSS-III Baryon Oscillation Spectroscopic Survey: Quasar Target Selection for Data Release Nine'. In: *ApJS* 199.1, 3, p. 3. DOI: 10.1088/0067-0049/199/1/3.

Rowan-Robinson, M. et al. (2008). 'Photometric redshifts in the SWIRE Survey'. In: *MNRAS* 386.2, pp. 697–714. DOI: 10.1111/j.1365-2966.2008.13109.x.

Salpeter, E. E. (1964). 'Accretion of Interstellar Matter by Massive Objects.' In: *ApJ* 140, pp. 796–800. DOI: 10.1086/147973.

Sandage, A. (1965). 'The Existence of a Major New Constituent of the Universe: the Quasistellar Galaxies.' In: *ApJ* 141, p. 1560. DOI: 10.1086/148245.

Sanders, D. B. et al. (1988). 'Ultraluminous infrared galaxies and the origin of quasars'. In: *ApJ* 325, pp. 74–91. DOI: 10.1086/165983.

Sarangi, A., E. Dwek and D. Kazanas (2019). 'Dust Formation in AGN Winds'. In: *ApJ* 885.2, 126, p. 126. DOI: 10.3847/1538-4357/ab46a9.

Schlafly, E. F. and D. P. Finkbeiner (2011). 'Measuring Reddening with Sloan Digital Sky Survey Stellar Spectra and Recalibrating SFD'. In: *ApJ* 737.2, 103, p. 103. DOI: 10.1088/0004-637X/737/2/103.

Schlafly, E. F., A. M. Meisner and G. M. Green (2019). 'The unWISE Catalog: Two Billion Infrared Sources from Five Years of WISE Imaging'. In: *ApJS* 240.2, 30, p. 30. DOI: 10.3847/1538-4365/aafbea.

Schlafly, E. F. et al. (2010). 'The Blue Tip of the Stellar Locus: Measuring Reddening with the Sloan Digital Sky Survey'. In: *ApJ* 725.1, pp. 1175–1191. DOI: 10.1088/0004-637X/725/1/1175.

Schmidt, M. (1963). '3C 273 : A Star-Like Object with Large Red-Shift'. In: *Nature* 197, p. 1040. DOI: 10.1038/1971040a0.

Schmidt, M. and R. F. Green (1983). 'Quasar evolution derived from the Palomar bright quasar survey and other complete quasar surveys.' In: *ApJ* 269, pp. 352–374. DOI: 10.1086/161048.

Schneider, D. P. et al. (2010). 'The Sloan Digital Sky Survey Quasar Catalog. V. Seventh Data Release'. In: *AJ* 139.6, 2360, p. 2360. DOI: 10.1088/0004-6256/139/6/2360.

Schwarz, S. (2003). 'For Good'. In: *'Wicked' (the musical)*.

Schwarzschild, K. (1916). 'Über das Gravitationsfeld eines Massenpunktes nach der Einsteinschen Theorie'. In: *Sitzungsber. Königl. Preuss. Akad. Wissenschaften*, pp. 189–196.

Seyfert, C. K. (1943). 'Nuclear Emission in Spiral Nebulae.' In: *ApJ* 97, p. 28. DOI: 10.1086/144488.

Shakura, N. I. and R. A. Sunyaev (1973). 'Black holes in binary systems. Observational appearance.' In: *A&A* 24, pp. 337–355.

Shen, Y. (2016). 'Rest-frame Optical Properties of Luminous $1.5 < z < 3.5$ Quasars: The Hβ-[O III] Region'. In: *ApJ* 817, 55, p. 55. DOI: 10.3847/0004-637X/817/1/55.

Shen, Y. et al. (2011). 'A Catalog of Quasar Properties from Sloan Digital Sky Survey Data Release 7'. In: *ApJS* 194, 45, p. 45. DOI: 10.1088/0067-0049/194/2/45.

Shen, Y. and L. C. Ho (2014). 'The diversity of quasars unified by accretion and orientation'. In: *Nature* 513.7517, pp. 210–213. DOI: 10.1038/nature13712.

Shen, Y. et al. (2015). 'The Sloan Digital Sky Survey Reverberation Mapping Project: Technical Overview'. In: *ApJS* 216.1, 4, p. 4. DOI: 10.1088/0067-0049/216/1/4.

Sijacki, D. et al. (2015). 'The Illustris simulation: the evolving population of black holes across cosmic time'. In: *MNRAS* 452, pp. 575–596. DOI: 10.1093/mnras/stv1340.

Silk, J. and M. J. Rees (1998). 'Quasars and galaxy formation'. In: *A&A* 331, pp. L1–L4.

Stevans, M. L. et al. (2014). 'HST-COS Observations of AGNs. II. Extended Survey of Ultraviolet Composite Spectra from 159 Active

Galactic Nuclei'. In: *ApJ* 794.1, 75, p. 75. DOI: 10.1088/0004-637X/794/1/75.

Storey, P. J. and C. J. Zeippen (2000). 'Theoretical values for the [OIII] 5007/4959 line-intensity ratio and homologous cases'. In: *MNRAS* 312, pp. 813–816. DOI: 10.1046/j.1365-8711.2000.03184.x.

Suganuma, M. et al. (2006). 'Reverberation Measurements of the Inner Radius of the Dust Torus in Nearby Seyfert 1 Galaxies'. In: *ApJ* 639.1, pp. 46–63. DOI: 10.1086/499326.

Sulentic, J. W., P. Marziani and D. Dultzin-Hacyan (2000). 'Phenomenology of Broad Emission Lines in Active Galactic Nuclei'. In: *ARA&A* 38, pp. 521–571. DOI: 10.1146/annurev.astro.38.1.521.

Swann, E. et al. (2019). '4MOST Consortium Survey 10: The Time-Domain Extragalactic Survey (TiDES)'. In: *The Messenger* 175, pp. 58–61. DOI: 10.18727/0722-6691/5129.

Symeonidis, M. (2017). 'What produces the far-infrared/submillimetre emission in the most luminous QSOs?' In: *MNRAS* 465, pp. 1401–1408. DOI: 10.1093/mnras/stw2784.

Tadhunter, C. et al. (2018). 'Quantifying the AGN-driven outflows in ULIRGs (QUADROS) - II. Evidence for compact outflow regions from HST [O III] imaging observations'. In: *MNRAS* 478.2, pp. 1558–1569. DOI: 10.1093/mnras/sty1064.

Takata, T. et al. (2006). 'Rest-Frame Optical Spectroscopic Classifications for Submillimeter Galaxies'. In: *ApJ* 651.2, pp. 713–727. DOI: 10.1086/507985.

Temple, M. J. et al. (2019). '[O III] Emission line properties in a new sample of heavily reddened quasars at $z > 2$'. In: *MNRAS* 487.2, pp. 2594–2613. DOI: 10.1093/mnras/stz1420.

Temple, M. J. et al. (2020). 'Fe III emission in quasars: evidence for a dense turbulent medium'. In: *MNRAS* 496.3, pp. 2565–2576. DOI: 10.1093/mnras/staa1717.

Temple, M. J. et al. (2021). 'Exploring the link between C IV outflow kinematics and sublimation-temperature dust in quasars'. In: *MNRAS* 501.2, pp. 3061–3073. DOI: 10.1093/mnras/staa3842.

Trumpler, R. J. (1930). 'Absorption of Light in the Galactic System'. In: *PASP* 42.248, p. 214. DOI: 10.1086/124039.

Urrutia, T. et al. (2012). 'Spitzer Observations of Young Red Quasars'. In: *ApJ* 757, 125, p. 125. DOI: 10.1088/0004-637X/757/2/125.

Vanden Berk, D. E. et al. (2001). 'Composite Quasar Spectra from the Sloan Digital Sky Survey'. In: *AJ* 122.2, pp. 549–564. DOI: 10.1086/321167.

Vasudevan, R. V. and A. C. Fabian (2007). 'Piecing together the X-ray background: bolometric corrections for active galactic nuclei'. In: *MNRAS* 381.3, pp. 1235–1251. DOI: 10.1111/j.1365-2966.2007.12328.x.

Vestergaard, M. and P. S. Osmer (2009). 'Mass Functions of the Active Black Holes in Distant Quasars from the Large Bright Quasar Survey,

the Bright Quasar Survey, and the Color-selected Sample of the SDSS Fall Equatorial Stripe'. In: *ApJ* 699.1, pp. 800–816. DOI: 10.1088/0004-637X/699/1/800.

Vestergaard, M. and B. J. Wilkes (2001). 'An Empirical Ultraviolet Template for Iron Emission in Quasars as Derived from I Zwicky 1'. In: *ApJS* 134, pp. 1–33. DOI: 10.1086/320357.

Vestergaard, M. and B. M. Peterson (2006). 'Determining Central Black Hole Masses in Distant Active Galaxies and Quasars. II. Improved Optical and UV Scaling Relationships'. In: *ApJ* 641.2, pp. 689–709. DOI: 10.1086/500572.

Villar Martín, M. et al. (2020). 'Peculiar emission line spectra of core extremely red BOSS quasars at z~2-3: orientation and/or evolution?' In: *A&A* 634, A116, A116. DOI: 10.1051/0004-6361/201937086.

Virtanen, P. et al. (2020). 'SciPy 1.0: fundamental algorithms for scientific computing in Python'. In: *Nature Methods* 17, pp. 261–272. DOI: 10.1038/s41592-019-0686-2.

Vogelsberger, M. et al. (2013). 'A model for cosmological simulations of galaxy formation physics'. In: *MNRAS* 436, pp. 3031–3067. DOI: 10.1093/mnras/stt1789.

Wang, H. et al. (2013). 'Outflow and Hot Dust Emission in High-redshift Quasars'. In: *ApJL* 776.1, L15, p. L15. DOI: 10.1088/2041-8205/776/1/L15.

Wethers, C. F. et al. (2018). 'UV-luminous, star-forming hosts of $z \sim 2$ reddened quasars in the Dark Energy Survey'. In: *MNRAS* 475, pp. 3682–3699. DOI: 10.1093/mnras/stx3332.

Wild, V. and P. C. Hewett (2005). 'Peering through the OH forest: a new technique to remove residual sky features from Sloan Digital Sky Survey spectra'. In: *MNRAS* 358.3, pp. 1083–1099. DOI: 10.1111/j.1365-2966.2005.08844.x.

Wild, V. and P. C. Hewett (2010). 'Peering through the OH Forest: public release of sky-residual subtracted spectra for SDSS DR7'. In: *arXiv e-prints*, arXiv:1010.2500, arXiv:1010.2500.

Wills, B. J., H. Netzer and D. Wills (1985). 'Broad emission features in QSOs and active galactic nuclei. II - New observations and theory of Fe II and H I emission'. In: *ApJ* 288, pp. 94–116. DOI: 10.1086/162767.

Wright, E. L. et al. (2010). 'The Wide-field Infrared Survey Explorer (WISE): Mission Description and Initial On-orbit Performance'. In: *AJ* 140.6, pp. 1868–1881. DOI: 10.1088/0004-6256/140/6/1868.

Wu, J. et al. (2018). 'Eddington-limited Accretion in $z \sim 2$ WISE-selected Hot, Dust-obscured Galaxies'. In: *ApJ* 852, 96, p. 96. DOI: 10.3847/1538-4357/aa9ff3.

York, D. G. et al. (2000). 'The Sloan Digital Sky Survey: Technical Summary'. In: *AJ* 120.3, pp. 1579–1587. DOI: 10.1086/301513.

Zakamska, N. L. and J. E. Greene (2014). 'Quasar feedback and the origin of radio emission in radio-quiet quasars'. In: *MNRAS* 442, pp. 784–804. DOI: 10.1093/mnras/stu842.

Zakamska, N. L. et al. (2016). 'Discovery of extreme [O III] λ5007 Å outflows in high-redshift red quasars'. In: *MNRAS* 459, pp. 3144–3160. DOI: 10.1093/mnras/stw718.

Zel'dovich, Y. B. (1964). 'The Fate of a Star and the Evolution of Gravitational Energy Upon Accretion'. In: *Soviet Physics Doklady* 9, p. 195.

Zhang, S. et al. (2014). 'Outflow and Hot Dust Emission in Broad Absorption Line Quasars'. In: *ApJ* 786.1, 42, p. 42. DOI: 10.1088/0004-637X/786/1/42.

Zhang, Z.-X. et al. (2019). 'Kinematics of the Broad-line Region of 3C 273 from a 10 yr Reverberation Mapping Campaign'. In: *ApJ* 876.1, 49, p. 49. DOI: 10.3847/1538-4357/ab1099.

Zubovas, K. and E. Nardini (2020). 'Intermittent AGN episodes drive outflows with a large spread of observable loading factors'. In: *MNRAS* 498.3, pp. 3633–3647. DOI: 10.1093/mnras/staa2652.

I've heard it said
That people come into our lives
For a reason
Bringing something we must learn
And we are led
To those who help us most to grow
If we let them...

– Schwarz (2003)

ACKNOWLEDGMENTS

Many people have helped to make my time as a Ph.D. student so enjoyable and productive. First and foremost, I am indebted to Paul and Manda for the time and interest they have invested in me. Thank you for believing in me, even when I might not have believed in myself, and for always having an open door. Thank you also to Amy, for always being happy to listen and talk about science, for allowing me to share your supervisors, and for letting me use your C IV measurements.

'This won't slow you down...'

I am grateful to everyone who has helped make the IoA such a stimulating and welcoming environment. In no particular order, specific thanks are due to Tom for helping me with Linux and making sure I went to Tea and Coffee on time; Debbie for always being so cheerful when I asked for money (or pizza); everyone in the extragalactic 'group', including Clare, Matt, Bob, Richard and James for countless useful conversations, and George for answering all my questions about X-rays; Thomas and Simon for taking me observing and introducing me to Chile; Sid, JJ, Laura and all the other students who have freely given their advice and support.

'burrito?'

The work presented in this thesis would not have been possible without the collaboration of the co-authors named in the declaration. My sincere thanks to Gary for teaching me many things about physics with such enthusiasm, and to Gordon for clear and thoughtful insights on all topics related to quasars, as well as providing a reference which helped to pave the way towards the next adventure.

My time in Cambridge has been enriched by many extraordinary people from across the University with whom I have had the privilege to interact. A special mention to Paddy, Rob, Miles, Katy and the members of CUW for inspiring me to be the best version of myself that I can be, and to the 2020 LW squad for their Mindset, Attitude and Purpose.

'P to M'

Finally, the people I have lived with over the past three years have all helped to make our house into a home. Working from home for

six months while a pandemic spread was made bearable only by those around me: thank you to Sophie for keeping me smiling with the crumbles, the bike rides, the music and the conversations; and to Anjali for sharing so much of the journey with me, from the first lecture in the Sackler, revising for Part III exams, observing 3C273 with the 16″, conversations about astronomy, academia and more. I couldn't have asked for more amazing housemates.

Matthew John Temple
Cambridge, September 2020

SCIENTIFIC ACKNOWLEDGMENTS

The work presented in this thesis has made heavy use of `NumPy` (Harris et al., 2020), `SciPy` (Virtanen et al., 2020), `AstroPy` (Astropy Collaboration et al., 2013, 2018), `Matplotlib` (Hunter, 2007) and `corner.py` (Foreman-Mackey, 2016); Python packages which have largely been developed for free by members of the community.

Grateful acknowledgement is made of the `Q3C` package (Koposov and Bartunov, 2006) and the Whole Sky Database (wsdb) created by Sergey Koposov and maintained at the Institute of Astronomy, Cambridge by Sergey Koposov, Vasily Belokurov and Wyn Evans with financial support from STFC and the European Research Council.

We thank the anonymous referees who provided feedback on Temple et al. (2019, 2020, 2021) prior to publication, and M. Vestergaard for making her Iron template available. This thesis would have been a lot harder to write without NASA's Astrophysics Data System, the arXiv, the NASA/IPAC Extragalactic Database (operated by the Jet Propulsion Laboratory, California Institute of Technology, under contract with NASA), and the SVO Filter Profile Service (which is supported by the Spanish MINECO through grant AYA2017-84089).

Chapters 2, 3 and 4 make use of data from the Sloan Digital Sky Survey. Funding for the Sloan Digital Sky Survey IV has been provided by the Alfred P. Sloan Foundation, the U.S. Department of Energy Office of Science, and the Participating Institutions. SDSS-IV acknowledges support and resources from the Center for High-Performance Computing at the University of Utah.

Chapters 3 and 4 make use of data products from the Wide-field Infrared Survey Explorer, which is a joint project of the University of California, Los Angeles, and the Jet Propulsion Laboratory/California Institute of Technology, and NEOWISE, which is a project of the Jet Propulsion Laboratory/California Institute of Technology. WISE and NEOWISE are funded by NASA.

Chapter 5 uses observations collected at the European Southern Observatory, Paranal, Chile, under ESO programmes 383.A-0573(A) and 095.A-0094(A).

MJT is grateful to the Science and Technology Facilities Council for the award of a studentship, to the UK taxpayers who paid for it, and to the Royal Astronomical Society, the Cambridge Philosophical Society and St Catharine's College for the award of travel grants.

This thesis was typeset in LaTeX using the typographical look-and-feel `classicthesis` developed by André Miede and Ivo Pletikosić.